ABSTRACT

| | |
|---|---|
| Title of Document: | REAL-TIME INVESTIGATION OF INDIVIDUAL SILICON NANOSTRUCTURED ELECTRODES FOR LITHIUM-ION BATTERIES. |
| | Khim Bahadur Karki, Doctor of Philosophy, 2013 |
| Directed By: | Professor John Cumings, Department of Materials Science and Engineering |

Silicon-based anode materials are an attractive candidate to replace today's widely-utilized graphitic electrodes for lithium-ion batteries because of their high gravimetric energy density (3572 mAh/g vs. 372 mAh/g for carbon) and relatively low working potential (~ 0.5V vs. $Li/Li^+$). However, their commercial realization is still far away because of the structural instabilities associated with huge volume changes of ~300% during charge-discharge cycles. Recently, it has been proposed that silicon nanowires and other related one-dimensional nanostructures could be used as lithium storage materials with greatly enhanced storage capacities over that for graphite in the next generation of lithium-ion batteries. However, the studies to date have shown that the nanomaterials, while better, are still not good enough to withstand a large number of lithiation cycles, and moreover, there is little fundamental insight into the science of the improvements or the steps remaining before widespread adoption. This

dissertation seeks to understand the basic structural properties and reaction kinetics of one dimensional silicon nanomaterials, including Si-C heterostructures during electrochemical lithiation/delithiation using *in-situ* transmission electron microscopy (TEM).

I present my work in three parts. In part I, I lay out the importance of lithium-ion batteries and silicon-based anodes, followed by experimental techniques using *in-situ* TEM. In part II, I present results studied on three different nanostructures: Si nanowires (SiNWs), Si-C heterostructures and Si nanotubes (SiNTs). In SiNWs, we report an unexpected two-phase transformation and anisotropic volume expansion during lithiation. We also report an electrochemically-induced weld of ~200 MPa at the Si-Si interface. Next, studies on CNT@α-Si heterostructures with uniform and beaded-string structures with chemically tailored carbon–silicon interfaces are presented. *In-situ* TEM studies reveal that beaded-string CNT@ α-Si structures can accommodate massive volume changes during lithiation and delithiation without appreciable mechanical failure. Finally, results on lithiation-induced volume clamping effect of SiNTs with and without functional Ni coatings are discussed. In Part III, a conclusion and a brief outlook of the future work are outlined. The findings presented in this dissertation can thus provide important new insights in the design of high performance Si electrodes, laying a foundation for next-generation lithium ion batteries.

# REAL-TIME INVESTIGATION OF INDIVIDUAL SILICON NANOSTRUCTURED ELECTRODES FOR LITHIUM-ION BATTERIES

By

Khim Bahadur Karki.

Dissertation submitted to the Faculty of the Graduate School of the
University of Maryland, College Park, in partial fulfillment
of the requirements for the degree of
Doctor of Philosophy
2013

Advisory Committee:
Professor John Cumings, Chair
Professor Chunsheng Wang
Professor Yu-Huang Wang
Professor Gary W. Rubloff
Professor James N. Culver

# Dedication

In memory of my father and to my mom.

# Acknowledgements

The past five years have been the “pinnacle-moment” of my life. It is thanks to my advisor Professor John Cumings, who believed and supported me in all pursued ideas (*few thoughtful, mostly crazy*) and provided guidance to make it happen. Both his intelligence and integrity as a scientist and an advisor are second to none, and there is no such thing as “undoable” in his vocabulary. I thank him for all the opportunities, guidance and support, for which I am forever indebted.

Next, I would like to thank Professor Chunsheng Wang for teaching me the fundamentals of batteries and also co-advising me in numerous projects. I am also grateful to Professor YuHuang Wang for research collaboration and insightful discussions. I am thankful to all the teachers in the department of Materials Science and Engineering as well as the Clark School’s Future Faculty Program (FFP). A special thanks is also due for Dr. Tom Picraux and his former postdoc Dr. Jeong-Hyun Cho, both from LANL, for assisting and guiding me in my experimental setup as well as supplying me with the samples, which basically paved the *track* of my dissertation. A research experiences under his group during the Summer 2011 was a rewarding experience. Furthermore, I should also acknowledge all the members of my dissertation committee, who took time and effort from their busy schedule to assist me in the smoother completion of the program.

Hadn’t it been my fellow members at the Cumings Group, things could have been quite different. To be precise: stressful and overwhelming. The moments spent with them: good humor, insightful discussions on all fronts (scientific, socio-

economic and political), and support for each other, always lifted my spirit. I will forever be grateful. A special thanks to Norvik Voskanian for helping me design my TEM electrochemical setup and also building a tomography holder pin. I would like to thank Paris Alexander for showing me to run the NanoFactory setup during the initial period of my experiments. I am grateful to Kamal Baloch (now a PhD and at BNL) for personal advices, research discussions and TEM support. I would also like to thank other fellow group members: Jeremy Ticey, Stephen Daunheimer, Kai He, Eric Epstein, Hanna Nilsson, Jasper Drisko, and John Bavier for insightful discussions and support. A special thanks is also due for postdocs at Professor YuHuang Wang Group, Dr. Hongwei Liao and Dr. ChuanFu Sun, and a graduate student at Professor Chunsheng Wang Group, Yujie Zhu ( now a PhD) for strong collaboration efforts, which resulted in three high-impact publications. My sincere thanks to NEES center, NEES staff especially Dr. Ashley Predith (now at OSTP), NISPLab staff especially Dr. Li-Chung (Larry) Lai and Dr. Pan-Ju (PJ) Shang, MSE staff especially Ms. Kay Morris. I would also like to thank all those who constantly supported me from the background: my dearest friends (especially Suman, who played an instrumental role in my decision to join Grad school), my previous advisors (Professor Vera Smolyaninova and Professor Rajeswari Kolagani), and all my relatives.

Above all, my whole-hearted gratitude goes to my loving family. A love of my life, my wife, Supriya has been a constant source of my inspiration, bestowing unconditional love and support. I promise to spend more time with you, maybe watch “never ending” soaps and help you in the kitchen. You are one good of a Personality.

And, I know you will be a terrific nurse one day. My parents, who always believed in me and supported me from a distance ("seven-seas apart" as they would like to say). My sister, Sarita who filled in my role, when I am here in the U.S., to take care of mom and late dad. My brother, Bhim, who has been very supportive during my ups-and-downs, and who is there for me at all times.

# Table of Contents

# List of Tables

# List of Figures

# List of Abbreviations

| | |
|---|---|
| AFM | Atomic Force Microscopy |
| ALD | Atomic Layer Deposition |
| CCD | Charged-Coupled Device |
| CE | Coulombic Efficiency |
| CNT | Carbon Nanotube |
| CVD | Chemical Vapor Deposition |
| DFT | Density Functional Theory |
| DMC | Dimethyl Carbonate |
| DMF | Dimethyl Formamide |
| EC | Ethylene Carbonate |
| EDP | Electron Diffraction Pattern |
| EDS | Energy Dispersive X-Ray Spectroscopy |
| EELS | Electron Energy Loss Spectroscopy |
| EFTEM | Energy-Filtered Transmission Electron Microscopy |
| EV | Electric Vehicle |
| FEA | Finite Element Analysis |
| FEG | Field Emission Gun |
| GeNW | Germanium Nanowire |
| HRTEM | High-Resolution Transmission Electron Microscopy |
| JEOL | Japanese Electron Optics, Ltd. |
| $LAB_6$ | Lanthanum HexaBorate |
| LANL | Los Alamos National Laboratory |
| LIBs | Lithium-Ion Batteries |
| LPCVD | Low-Pressure Chemical Vapor Deposition |
| LTO | Low Temperature Oxidation |
| MWCNT | Multi-walled Carbon Nanotube |
| NMR | Nuclear Magnetic Resonance |
| OCV | Open Circuit Voltage |
| PAN | Polyacrylonitrile |
| PECVD | Plasma-Enhanced Chemical Vapor Deposition |
| SEI | Solid Electrolyte Interphase |
| SEM | Scanning Electron Microscopy |
| SiNT | Silicon Nanotube |
| SiNW | Silicon Nanowire |
| SSA | Solid State Amorphization |
| STEM | Scanning Transmission Electron Microscopy |
| STM | Scanning Tunneling Microscopy |
| TE | Thermionic Emission |
| TEM | Transmission Electron Microscopy |
| UMD | University of Maryland |
| VLS | Vapor Liquid Solid |
| XRD | X-Ray Diffraction |

# List of Publications

1. X. H. Liu, H. Zheng, L. Zhong, S. Huang, **K. Karki**, L. Q. Zhang, Y. Liu, A. Kushima, W. T. Liang, J. W. Wang, J.-H. Cho, E. Epstein, S. A. Dayeh, S. T. Picraux, T. Zhu, J. Li, J. P. Sullivan, J. Cumings, C. Wang, S. X. Mao, Z. Z. Ye, S. Zhang, and J. Y. Huang, "Anisotropic Swelling and Fracture of Silicon Nanowires during Lithiation," *Nano Letters*, vol. 11, no. 8, pp. 3312–3318, Jun. 2011.

2. H. Liao, **K. Karki**, Y. Zhang, J. Cumings, and Y. Wang, "Interfacial Mechanics of Carbon Nanotube@Amorphous-Si Coaxial Nanostructures," *Advanced Materials*, vol. 23, no. 37, pp. 4318–4322, 2011.

3. D. Ruzmetov, V. P. Oleshko, P. M. Haney, H. J. Lezec, **K. Karki**, K. H. Baloch, A. K. Agrawal, A. V Davydov, S. Krylyuk, Y. Liu, J. Huang, M. Tanase, J. Cumings, and A. A. Talin, "Electrolyte Stability Determines Scaling Limits for Solid-State 3D Li Ion Batteries," *Nano Letters*, vol. 12, no. 1, pp. 505–511, Dec. 2011.

4. **K. Karki**, E. Epstein, J.-H. Cho, Z. Jia, T. Li, S. T. Picraux, C. Wang, and J. Cumings, "Lithium-Assisted Electrochemical Welding in Silicon Nanowire Battery Electrodes," *Nano Letters*, vol. 12, no. 3, pp. 1392–1397, Feb. 2012.

5. C.-F. Sun *, **K. Karki** *, Z. Jia *, H. Liao, Y. Zhang, T. Li, Y. Qi, J. Cumings, G. W. Rubloff, and Y. Wang, "A Beaded-String Silicon Anode," *ACS Nano*, vol. 7, no. 3, pp. 2717–2724, Feb. 2013.

   [* equal contribution]

6. **K. Karki**, Y. Zhu, Y. Liu, C.-F. Sun, L. Hu, Y. Wang, C. Wang, and J. Cumings, "Hoop-Strong Nanotubes for Battery Electrodes," *ACS Nano*, vol. 7, no. 9, pp. 8295–8302, Aug. 2013.

# Chapter 1: Introduction

## 1.1. Energy Storage

Energy is one of the biggest challenging topics of modern society. According to the pioneer nanotechnologist, Richard Smalley, "Energy" is projected to top the list of problems humanity will face in the next 50 years [1]. The rising demand of energy consumption with the approaching depletion of natural fuel resources is only validating the claim. Therefore, the need for alternative sources of energy has become more important than ever before. Renewable sources such as solar and wind power can be among the best options to meet the future energy demands. However, the intermittent nature of energy generated from these resources would be unable to meet the threshold of the on and off peak energy demands. So, high-performance electrical energy storage technology is desirable to enable clean, efficient and uninterruptible power supply to the consumer. Batteries, among many other storage technologies can store significantly more energy per unit mass (energy density), naturally becoming the best contender to manage renewable resources and achieve economic sustainability.

Among existing battery technologies, lithium-based batteries easily outperform other rechargeable batteries owing to their high energy density (210 Wh/kg), high discharge potential (3.7 V vs. 1.2 V for nickel cadmium/nickel metal hydride), and good shelf life (Figure 1.1) [2]. Rechargeable lithium-ion batteries have already ruled the portable electronic market, slowly replacing nickel-technology for power tool

applications and stimulating huge R&D efforts for the cheaper and safer electric vehicles (EVs).

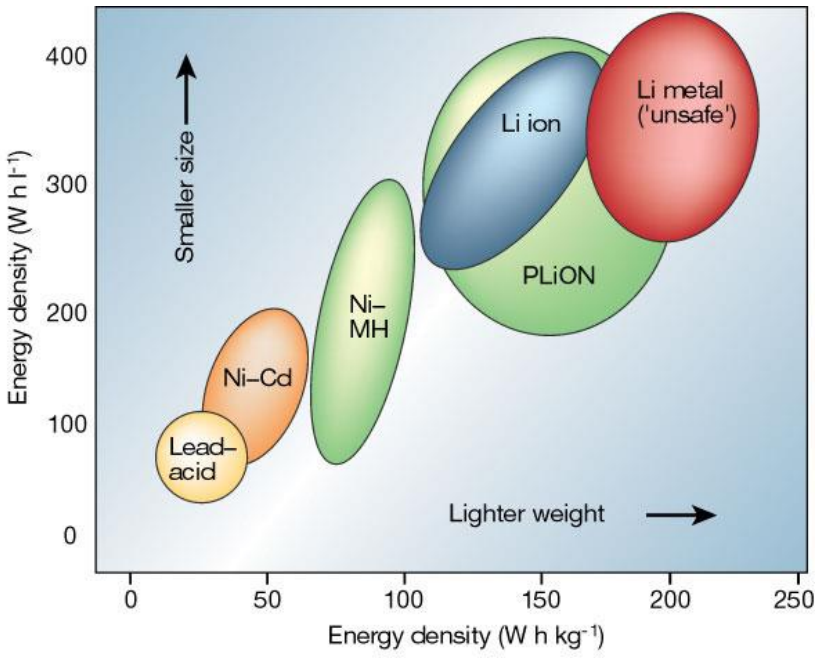


Figure 1.1: Comparison of various battery technologies in terms of volumetric and gravimetric energy density. Figure adapted from Ref. [2].

## 1.2. Lithium-ion Batteries

### 1.2.1 Fundamentals of Batteries

A battery is a device which converts chemical energy from its active materials into electrical energy by a process called electrochemical oxidation-reduction (redox) reaction [3]. A single electrochemical unit of a battery is referred to as a "cell" while the battery may constitute one or more cells connected in series, parallel, or both depending on the desired voltage and capacity. A cell comprises three major components – a) anode or negative electrode, b) electrolyte and c) cathode or positive

electrode. Basically, the anode is the reducing electrode, which loses electrons that go through the external circuit during power discharge. The cathode is the oxidizing electrode which gains electrons from the externally dissipating part of the circuit and becomes reduced during the electrochemical reaction. Both anode and cathode electrodes should ideally possess the following features: high energy density or coulombic output (Ah/g), good electronic and ionic conductivity, chemical stability, desirable working potential, abundant natural sources, and an effective supply chain. An electrolyte, on the other hand, acts as a medium to transfer ions across the negative and positive electrodes. Ideally, the electrolyte should have good ionic conductivity, and should be an electronic insulator, in order to prevent a short-circuit path between the two electrodes during operation. Additionally, an electrolyte should maintain these properties at different temperatures and should remain chemically inactive towards both electrodes. Ideally, lithium metal, which is the lightest metal and a good reducing agent, can serve as the best anode electrode, but the formation of dendrites can complicate this, as described in the following sections. For cathode materials, metallic oxides or even molecular oxygen, which provide high voltages and capacity, can be the best candidates for battery applications. The choice of electrolyte could be aqueous or non-aqueous salts with good ionic conductivity and high thermodynamic potential window, although the non-aqueous varieties are generally more effective.

### 1.2.2 Thermodynamics

The standard theoretical potential (or voltage), which is also referred to as open circuit or equilibrium or working potential of a battery cell is determined by the thermodynamics of the chemical reaction between the active materials in the electrodes, which basically drives the transport of ions through the electrolyte, and electrons through the external circuit [3], [4].

The standard potential can be empirically calculated as follows [3]:

Anode (oxidation potential) + cathode (reduction potential) = standard cell potential

It should be noted that the oxidation potential is the negative value of the reduction potential. Mathematically [3], the reaction occurring at the cathode or positive electrode (reduction reaction) of a half-cell can be expressed as:

$$\alpha A + ne \leftrightarrow \gamma C \tag{1.1}$$

Where $\alpha$ molecules of $A$ take up $n$ electrons $e$ to form $\gamma$ molecules of $C$. Similarly, reaction at the anode or negative electrode (oxidation reaction) of a half-cell follows as:

$$\beta B - ne \leftrightarrow \delta D \tag{1.2}$$

The overall reaction in the cell is given by adding the above two half-cell reactions, as follows:

$$\alpha A + \beta B \leftrightarrow \gamma C + \delta D \tag{1.3}$$

The change in the standard free energy $\Delta G^\circ$ of this reaction is given by

$$\Delta G^\circ = - nFE^\circ \tag{1.4}$$

Here, $F$ is the Faraday constant (96,487 Coulombs), and $E^\circ$ is the standard electromotive force (Volts). However, the above condition (Eq. 1.4) is true only in the

standard state. In a practical cell, the voltage $E$ is governed by Nernst equation, which is given as:

$$E = E^{\circ} - \frac{RT}{nF} ln \frac{a_C^{\gamma} a_D^{\delta}}{a_A^{\alpha} a_B^{\beta}} \quad (1.5)$$

Here, $a_i$ is the activity of species, $R$ is the gas constant, and $T$ is the absolute temperature. It is the change in the standard free energy $\Delta G^{\circ}$ which drives a chemical reaction in the cell and provides an electrical energy to the battery through the external charging part of the circuit.

### 1.2.3 Kinetics

In a practical cell, the actual operating voltage between the two electrodes is slightly lower than thermodynamically possible values [4]. The practical values largely depend on various kinetic factors involved between the electrodes. It is important to note that the electrode kinetics are somewhat different from chemical kinetics because of the following two important reasons: (1) the potential drop at the electrode/electrolyte interface affects the activated complexes and (2) the reactions at the interfaces are 2D in nature, rather than 3D [5]. These reactions often involve a series of physical, chemical, and electrochemical steps, including charge-transfer and charge transport steps. The rates of these individual reactions/ steps determine the kinetics of battery electrodes and cells. Basically, there are three different kinds of kinetic losses caused by the polarizations occurring during the electrochemical reaction [3], [5]. These are as follows: (1) activation polarization, (2) ohmic polarization and (3) concentration polarization. The typical discharge curve of a battery showing the different types of polarization is shown in Figure 1.2 [5].

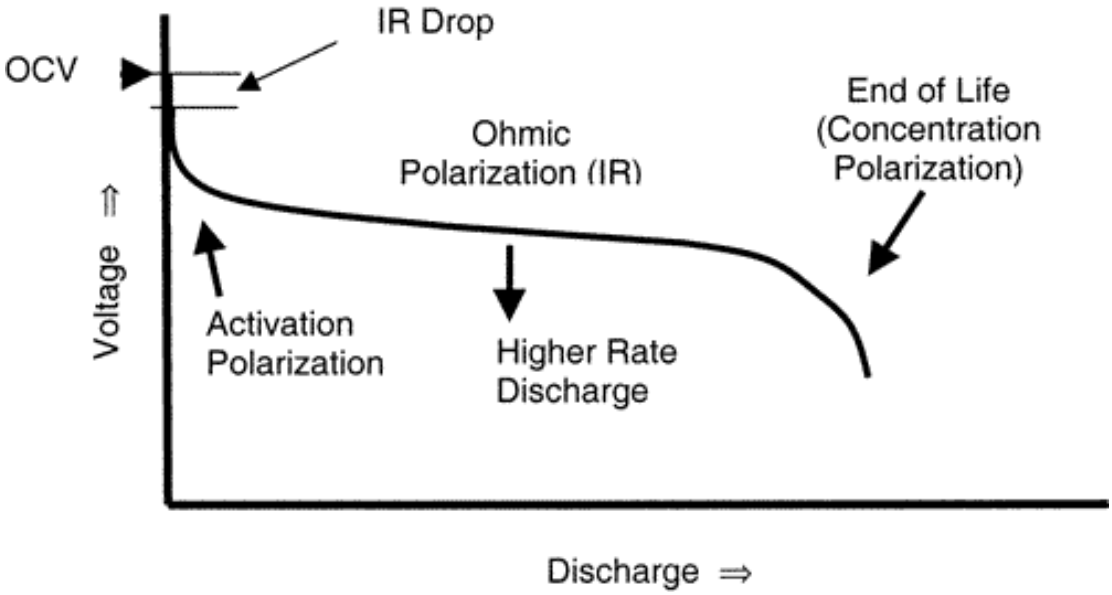


Figure 1.2: Typical discharge curve of a battery showing different types of polarization. Figure Adapted from Ref. [5].

Activation polarization occurs at the electrode/electrolyte interface which is due to the hindrance of the charge-transfer reaction during the electrochemical reaction. Ohmic polarization is due to the internal impedance or IR drop of a cell and corresponds proportionally with the current drawn from the system. Both ionic resistance of the electrolyte and electronic resistance of the electrodes and electronic components which are ohmic in nature can directly contribute to the overall impedance. Concentration polarization occurs due to the limitation of mass-transfer caused by the concentration difference between the reactants and products at the electrode surface. Therefore, the total voltage (E) delivered by the cell when it connected to the external load is given by Eq. 1.6:

$$E = E^{\circ} - [\eta_a + \eta_o + \eta_c] \qquad (1.6)$$

Here, $E^{\circ}$ is the open circuit voltage of a cell, while $\eta_a$, $\eta_o$, and $\eta_c$, are activation, ohmic and concentrations polarizations, respectively.

In order to minimize the loss of energy due to polarization, the following consideration in the battery materials are necessary [3]:

1) Both the anode and cathode electrodes should be sufficiently conducting, ionically and electronically, thereby reducing the ohmic polarization. Additionally, an electrode with high surface area and high rate of electrochemical reaction can help significantly reduce both the activation and concentration polarization.
2) Electrolyte should be ionically conducting, which can reduce ohmic polarization and can remain chemically stable against both the electrodes.

### 1.2.4. Operations and General Terms of Lithium-Ion Chemistry

Like any other battery chemistry, lithium-ion batteries (LIBs) requires three major components: anode (negative electrode), electrolyte and cathode (positive electrode). The operating potential of the anode is typically lower than 3 V *vs.* $Li/Li^+$, while it is higher than 2 V *vs.* $Li/Li^+$ for the cathode. There is generally also a porous polymeric separator between the anode and cathode which prevents the two electrodes from short-circuiting but readily allows the passage of lithium ions ($Li^+$) through the electrolyte. The most commonly used anode, cathode and electrolyte in today's LIBs are graphite, lithium cobalt oxide ($LiCoO_2$), and an organic mixture of ethylene carbonate (EC)/dimethyl carbonate (DMC), respectively. The choice of electrolyte avoids the problem of hydrolysis of an aqueous solvent into $H_2$ and $O_2$ gas, which can occur for potentials outside the "water window" of 2.9 V. The schematic showing the

working principle of lithium-ion battery is given in Figure 1.3. During charge, reduction takes place at cathode, and the free $Li^+$ ions migrate through the ionically conducting electrolyte and intercalate within the anode. The $Li^+$ ions travelling through the electrolyte are also compensated by electron flowing through the external part of the circuit. During discharge, the reverse process occurs, wherein the anode is oxidized to liberate $Li^+$ ions, which intercalate back to the cathode host. This shuttling of lithium ions between anode and cathode induced by redox reaction gives the energy output of the battery.

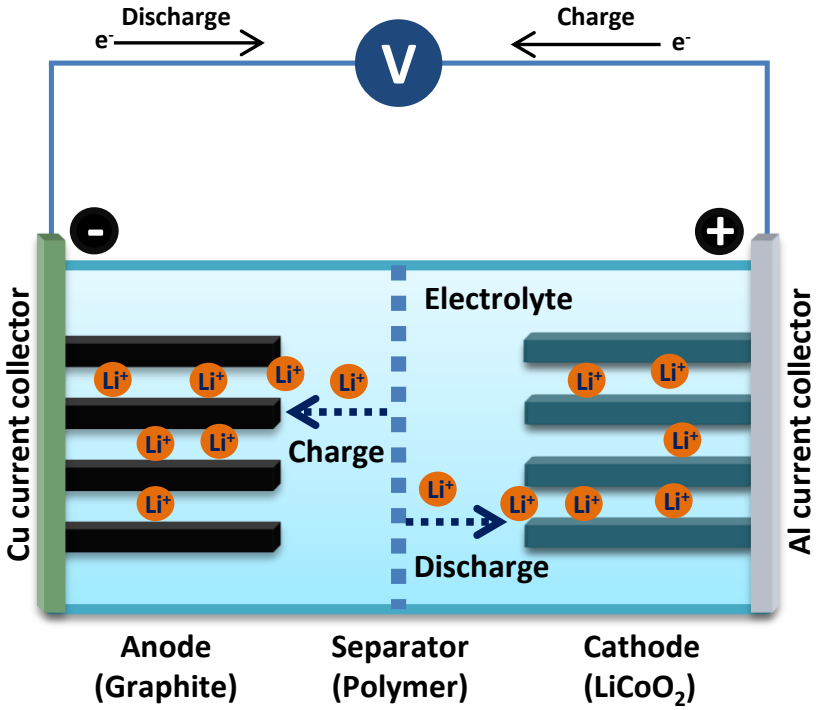


Figure 1.3: Operation of lithium-ion batteries (LIBs). During charge, the cathode is electrochemically reduced and $Li^+$ ions travel through the electrolyte and intercalate at the anode. The electrons are simultaneously released to compensate the loss of charges. The reverse process occurs during the discharge.

The energy output (also referred to as energy density) of a battery depends on the operating voltage between two electrodes (determined by redox reactions) and the specific charge capacities of the electrode materials [6].

The specific charge capacity of the electrode, $C_{electrode}$ can be calculated using the following eq. 1.7 [7].

$$C_{electrode}\left(\frac{\text{mAh}}{\text{g}}\right) = \frac{z \times x\,(mol) \times F\left(\frac{C}{mol}\right)}{3.6\left(\frac{C}{\text{mAh}}\right) \times M_{electrode}\left(\frac{g}{mol}\right) \times 1\,mol} \qquad (1.7)$$

Where $z$ is the charge of lithium ion, $x$ is moles of extracted/inserted lithium ions, $M_{electrode}$ is the molecular weight of an electrode, and $F$ is the Faradaic constant. The *electrode* can be either anode or cathode in a cell. The operating (or working) potential and theoretical specific capacities of most commonly studied anode and cathode materials are provided in Table 1.1

| Electrode | Open circuit potential (OCV) (Working potential vs. $Li/Li^+$) (V) | Theoretical specific capacity (mAh/g) |
|---|---|---|
| <u>Anode</u> | | |
| Lithium metal (Li) | 0 | 3861 |
| Graphite (C), $LiC_6$ | 0.2 | 372 |
| Silicon (Si), $Li_{4.4}$ Si | 0.4 - 0.5 | 4200 |
| Lithium Titanate ($Li_4Ti_5O_{12}$) | 1.5 | 175 |

| Cathode | | |
|---|---|---|
| Lithium Cobalt Oxide ($LiCoO_2$) | 4.1 | 137 |
| Lithium Manganese Oxide ($LiMn_2O_4$) | 4.2 | 148 |
| Lithium Iron Phosphate ($LiFePO_4$) | 3.6 | 170 |
| Vanadium Oxide ($V_2O_5$), 2Li | 3.4 | 294 |

Table 1.1: Working potentials (also OCV), and theoretical specific capacities of most commonly studied anode and cathode materials. Adapted from Refs. [8], [9].

The energy density of each electrode is the product of specific capacity and open circuit voltage (OCV), which is expressed as in Eq. 1.8.

$$Energy\ density\ \left(\frac{\mathrm{Wh}}{\mathrm{kg}}\right) = C_{electrode}\ \left(\frac{\mathrm{mAh}}{\mathrm{g}}\right) \times OCV \qquad (1.8)$$

The OCV also depends of the rate at which the battery is charged and discharged [6]. If a battery is discharged quickly for high power applications, an overpotential is needed to drive the electrode reactions at fast rates. This drive can significantly reduce the OCV and the energy output of a cell. The energy density of a battery can be lowered by any kind of polarization, as mentioned above.

The energy density of the battery refers to the total amount of stored energy delivered per unit mass, expressed in the units of Wh/kg. The rate at which a battery is charged and discharged is given by the term C-Rate. The charge/discharge rate is expressed as C/n, where n is the numbers of hours required to completely charge/discharge the nominal capacity C. For instance, if a rate of C/2 is applied to fully discharge a cell with a nominal capacity of 4 Ah, it would take a total time of 2 hours and discharge

current would be 2 A. In simple terms, a rate of 1C represents charging or discharging a battery in 1 hour.

The total capacity of a lithium-ion cell is calculated by the given Eq. 1.9 [10].

$$C_{cell}\left(\frac{\text{mAh}}{\text{g}}\right) = \frac{1}{\frac{1}{C_a}+\frac{1}{C_c}+\frac{1}{Q_m}} \tag{1.9}$$

Where $C_a$ and $C_c$ are the theoretical specific capacities of anode and cathode, respectively, in units of mAh/g, and $1/Q_m$ is the specific mass of other cell components (electrolyte, separator, current collectors, case, etc.), in units of g mA/h. Coulombic efficiency (CE) of a battery is the ratio of total input charge capacity $(C_{input})$ during charge and output capacity $(C_{output})$ during discharge, as given in Eq. 1.10.

$$Coulombic\ \text{efficiency (CE)} = \frac{C_{output}}{C_{input}} \times 100\% \tag{1.10}$$

### 1.2.5 Current LIBs: Improvements and Challenges

Sony introduced the first commercial LIBs in 1990 using graphite as the negative electrode and lithium cobalt oxide ($LiCoO_2$) as the positive electrode [6]. After two decades, consumers still rely on nearly the same battery chemistries and materials to power their electronic, with the energy density of LIBs having been improved only slightly in the past decade. The surge in the portable electronics and other technological ambitions such as EVs is only adding need for improved battery technology. While the processing power in computing power seems to rise with the pattern of so-called “Moore’s Law,” famously predicted by Intel co-founder Gordon Moore, no such parallel advancement exists for batteries or other energy storage devices [2], [11]. A battery is driven by ions, and compared to electrons, they are

larger in size and needs space to accommodate within the structure. So, the right selection of materials and appropriate design of electrodes can only enable the development of better batteries with high-energy and high-power densities needed to power advanced applications.

My thesis work is based on the study of anode materials, exclusively focused on understanding the fundamentals and scope of alloy-based silicon for use in LIBs. Below, I will discuss some of the positive and negative electrode materials, which are currently been used and studied for future LIBs applications.

1.2.5.1 Anode or Negative Electrode Materials

Early on, lithium (Li) metal attracted considerable interests for use as an anode material for LIBs [10]. Lithium, being the lightest metal in the periodic table and with large reduction potential (-3.04 V *vs.* standard hydrogen potential), can generate high output voltage and thus deliver higher specific energy density of 3860 mAh/g (Table 1.1). The use of Li-metal based battery was first demonstrated in 1970s in the form of primary cell (non-rechargeable) [2]. The working concept of a rechargeable battery was only introduced in 1972 by Exxon [12]. They used $TiS_2$ as the positive electrode, Li metal as the negative electrode and lithium percholate in dioxolane as the electrolyte. However, Li metal posed serious safety issues due with lithium dendrite formation at the anode surface and led to the potential problem of short circuiting the electrodes. So, lithium metal batteries were never really commercialized and are still an active area of research.

In 1990, Sony introduced the first successful LIBs with a carbonaceous anodes, replacing lithium metal, and lithium cobalt oxide ($LiCoO_2$) as a cathode [13]. Because

Li was used in the ionic form rather than metallic state, the problem associated with dendrite formation was relatively solved. The standard carbonaceous graphite anode can intercalate one Li atom per six carbon atoms –$LiC_6$ during charging- with the possibility of delivering 372 mAh/g specific capacity in single cells. It is relatively safe, cheaper and has long cycle life compared to $TiS_2$. However, the lower energy density of carbonaceous anode cannot satisfy needs for high power and capacities for applications such as power tools and EVs. Also, the sluggish nature of lithium ion diffusion in the graphitic layers inhibits faster charge/discharge rate and limits its use in the power tool industry. Most important of all, the lower operating potential of graphite (Table 1.1) can cause the electrolyte to decompose at the graphite surface leading to the formation of passivating layer called solid electrolyte interphase (SEI) [9]. The SEI layer is usually composed of $Li_2CO_3$, various lithium salts, LiF, $Li_2O$ and nonconductive polymer, which could vary depending on the type of organic electrolyte used (see Figure 1.4). Typically, the decomposition of the electrolyte into a variety of SEI layers is reported to occur below the operating potential of 1.5 V and 4 V at the anode and cathode interfaces, respectively [14]. These SEI components can be insulators to both $Li^+$ ions and electrons, and thus SEI layers can seriously impede the diffusion of lithium ions in the subsequent cycles, increasing the risk of lithium plating during charge and discharge. The issue of lithium plating may not be evident in portable devices, but when used in large-scale applications like EVs, safety during high charge/discharge rates becomes a huge challenge.

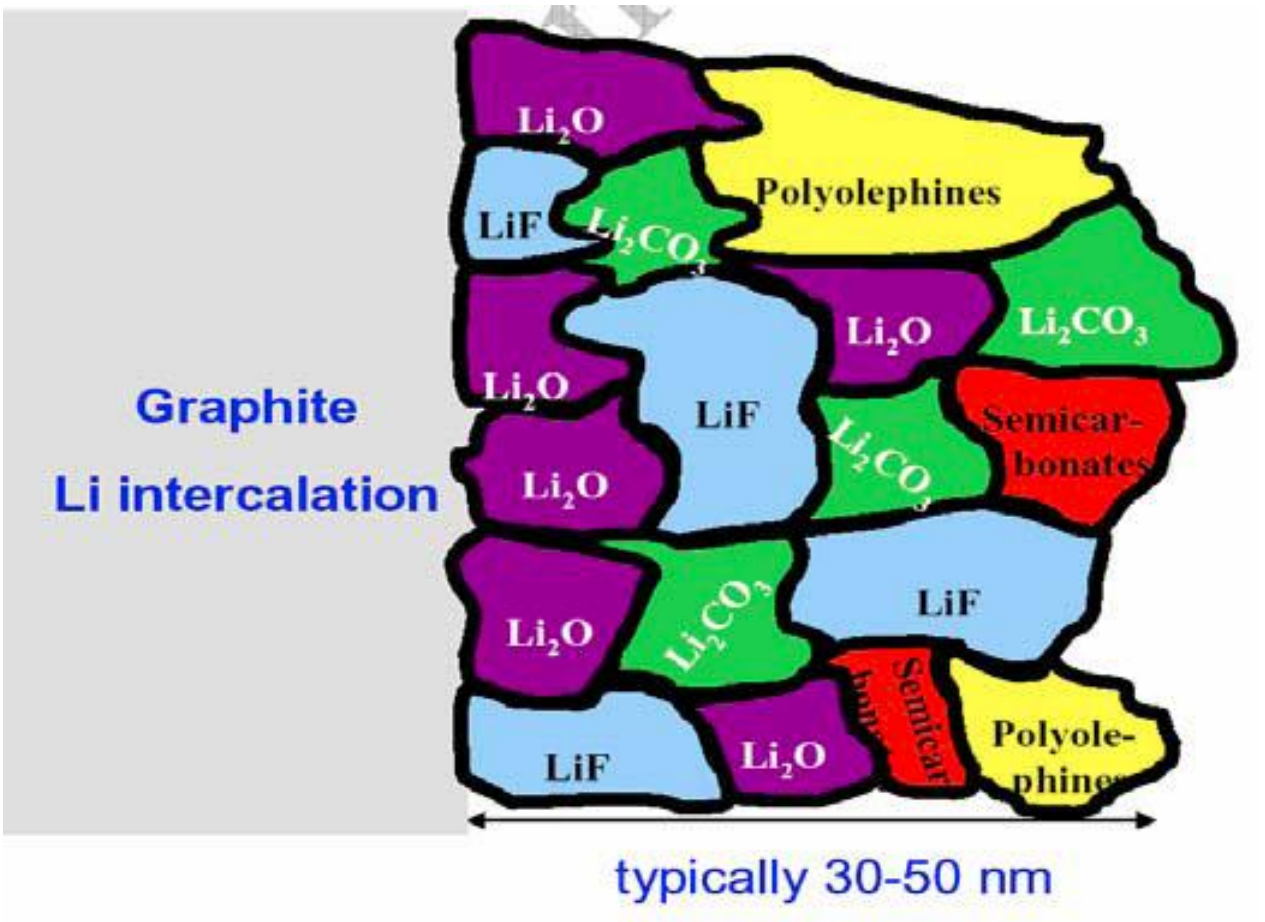


Figure 1.4: A schematic showing different components of the SEI layer. Figure adapted from DOE's Reports of the Basic Energy Sciences Workshops on electrical Energy Storage, 2007 [15].

Another insertion-based anode, $Li_4Ti_5O_{12}$ (LTO) with a defected spinel structure garnered tremendous interests due to its chemical stability and low cost. Compared to graphite, it intercalates $Li^+$ ions at a higher operating potential of 1.5 V, which is within the thermodynamic limits of most standard aqueous electrolyte solutions [14]. Thus, no SEI is formed, and the possibility of Li plating is avoided. Additionally, it undergoes less structural changes during electrochemical lithiation and delithiation.

However, its limited capacity (~160 mAh/g) and high operating potential (1.5 V) significantly reduce the cell voltage and energy density [14]. For these reasons, LTO is practically unfeasible for use in mobile electronics and EVs, although it could be good choice for grid applications.

Conversion-based anode materials have also received considerable interests because of their high stability and longer cycle life [14]. In the conversion systems, oxides are converted to a metallic state and a $Li_2O$ matrix during lithiation and the reaction can be reversed back to some extent during delithiation. As $Li^+$ ions do not require a host-site during the process, structural changes are limited, and the materials can be electrochemically reversed for hundreds of cycles. However, these anodes suffer from high polarization and poor kinetics, requiring significant energy to break M-O bonds during the conversion process. Sometimes, Li plating might occur if the influx of $Li^+$ ions is faster than the host can incorporate, thus compromising battery stability.

Recently, alloy based anodes such as Si, Sn, Al, Pb etc. have attracted much attention due to their higher theoretical energy densities, low cost, environmental safety, and low operating potentials [9], [10], [16]. Ever since Dey et al. first reported the possibility of lithium electrochemically alloying with intermetallic metals, massive research efforts have been invested to exploit their properties for commercialization [10]. However, the electrode instability and rapid capacity fade (due to irreversible loss of capacity) caused by massive volume changes (~300-400 %) during alloying (charging) and dealloying (discharging) remains a grave challenge for alloy based anodes. A review of the silicon-based anode, highlighting the advantages and challenges, is discussed below in Section 1.3.

The reaction mechanisms of the most commonly studied forms of anode materials are summarized as follows:

a) Insertion-based (commonly graphite)

$$Li^+ + e^- + C_6 \leftrightarrow LiC_6 \quad (1.11)$$

b) Insertion-based spinel structure (commonly $Li_4Ti_5O_{12}$)

$$Li_4Ti_5O_{12} + xLi^+ + xe^- \leftrightarrow Li_4 + xTi_5O_{12}, [x = 2 \text{ to } 3] \quad (1.12)$$

c) Conversion-based (commonly transition metal oxides such as CuO, $Co_3O_4$)

$$MO + 2Li^+ + 2e^- \leftrightarrow M + Li_2O, [M= Fe, Co, Ni, Cr, Mn, Cu] \quad (1.13)$$

d) Alloy-based (commonly Si, Sn)

$$Si\ (Sn) + xLi^+ + xe^- \leftrightarrow Li_xSi\ (Sn), [x = 4.4 \text{ (maximum)}, 3.75 \text{ (room-temperature)}] \quad (1.14)$$

1.2.5.2 Cathode or Positive Electrode Materials

The cathode serves as a $Li^+$ ion reservoir in a battery during the discharge state. Typically, cathodes are made of metal oxides and phosphates [2]. Lithium cobalt oxide ($LiCoO_2$) is the current state-of-the-art cathode. But, the high cost and scarcity of cobalt cannot meet the rising demands, especially when there is high prospect for its use in EVs and other hybrid vehicles. Lithium transition-metal oxide spinels such as $LiM_2O_4$ (M = Mn, Ni) and lithium transition-metal phosphates such as $LiMPO_4$ (M = Fe, Ni, Mn) have been proposed as an alternatives [2]. The electrochemical performance of these oxides and phosphates are practically comparable to $LiCoO_2$ and yet are less expensive.

Another big concern for the cathode materials is the possibility of "thermal runaway," which is triggered by increased oxygen generation during the lithium deintercalation reaction. Some of the cathode materials have been shown to generate three-to-four

times more heat than the graphite anodes at the fully lithiated state at above 200˚C [17], [18]. This grave problem associated with the thermal runaway should be addressed in order to ensure the safety of a battery. Of the various cathodes studied, $LiMn_2O_4$ and $LiFeO_4$ have shown to generate only a modest concentration of oxygen at the fully charged states. As a result, these cathodes have been considered as the main contenders for use in future EVs [18]. The most recent exhaustive reviews highlighting the development of cathode electrode materials are given in references [19] and [20].

In Li-metal batteries, the Li anode provides a high-capacity source of $Li^+$ ions. Thus, there is no need for the cathode to have any additional $Li^+$ ions, and the starting materials can be devoid of $Li^+$ ions. However, in LIBs, the graphite anode is generally lithium-deficient, and thus such batteries depend solely on the cathode for $Li^+$ ions. Therefore, the major practical requirement of cathode materials is to provide air-stable Li-based intercalation compounds for manufacturing [2]. A second major challenge with the conventional inorganic cathode materials is that they are limited by the quantity of $Li^+$ ions that can be extracted without collapse of the structure. For instance, extracting beyond 0.5 Li in $LiCoO_2$ during lithiation of anode could bring its lattice structure near to collapse and could lead to failure of the electrode [2], [6]. In practical LIBs, a certain charge cut-off voltage is set to ensure the structural stability of the electrode, thereby preventing safety concerns. In doing so, only about half of the $Li^+$ ions are ever deintercalated from the cathode. The available energy charge capacities of cathode materials are thus limited only to the range of 120-160 mAh/g [2], [6].

Anode materials, on the other hand, such as graphite, have higher charge storage capacities of 372 mAh/g or more. To compensate for the lower charge capacities available in cathodes, they are usually made thicker compared to the anodes. However, as the thickness of the cathode increases, other challenges associated with various polarization factors can seriously impede $Li^+$ ion mobility and thus the power density of a battery.

Therefore, the smart-engineering of both anode and cathode materials seems to be the only viable option to improve the charge capacity and power of a battery.

In the next section, I will provide a brief literature review of challenges and opportunities for using silicon-based anodes.

## 1.3. Silicon-Based Negative Electrodes

Among the alloy-based anodes, silicon has major advantages over current graphitic technology because its specific energy density (thermodynamically limit $Li_{4.4}Si$; 4200 mAh/g) is nearly 10 times that of carbon (see Table 1.2), and is still earth abundant.

| Anode material (lithiated state) | C ($LiC_6$) | Bi ($Li_3B$) | Al (LiAl) | Sn ($Li_{4.4}Sn$) | Ge ($Li_{4.4}Ge$) | Si ($Li_{4.4}Si$) |
|---|---|---|---|---|---|---|
| Gravimetric energy density (mAh/g) | 372 | 385 | 993 | 994 | 1384 | 4200 |
| Volumetric energy density ($mAh/cm^3$) | 855 | 3765 | 2681 | 7246 | 7366 | 8334 |
| Volumetric change (%) | 10 | 215 | 94 | 260 | 250 | 400 |

Table 1.2: Gravimetric and volumetric energy densities of the most commonly studied alloy-based anodes. The volumetric expansion (%) during charge is also given. The values of carbon are given as a reference. Adapted from Ref. [9].

However, as mentioned earlier, the practicality of a silicon anode-based battery can only be realized when the following two of its biggest problems are solved: charge irreversibility (capacity retention) and material instability (cycle life) [10], [16]. During the initial first cycle, silicon suffers from a huge irreversible capacity loss which amounts to roughly 25% of the coulombic efficiency. The immense loss of capacity during the first few cycles is partly because of the huge volume change (~300-400%) during the lithium alloying and dealloying process (Table 1.2) which causes stress-related cracking and disconnection of active materials from the current collector. In the meantime, a passivating SEI layer is also formed at the silicon-electrolyte interface during cycling. While the inevitability of SEI layer formation remains a challenge for all low potential materials such as silicon and carbon, repeated deposition of additional layers can be especially detrimental. When silicon

undergoes huge deformation, it simultaneously breaks away the SEI layer re-exposing a fresh silicon surface to the electrolyte. As the thickness of the SEI layers add up during each charge/discharge cycle and reaches to certain limit, $Li^+$ ions can no longer shuttle back and forth between the electrodes. This permanent trapping of lithium ions in disconnected materials along with the huge deposition of SEI layer leads to irreversible capacity loss and poor cycle life.

Various strategies have been proposed and tested to overcome the issue of structural instability and rapid capacity fade associated with silicon electrodes. One approach is to incorporate active and inactive matrix composites to silicon electrode materials [10], [16]. The addition of inactive matrix such as Fe, Cu, TiN, TiB etc., have been shown to buffer silicon particles and to help mitigate the rapid volume changes. Similarly, the addition of an active matrix such as carbon enhances the interparticle electronic contact to improve charge/discharge rate, provides mechanical rigidity to suppress volume changes, and also hosts lithium ions to increase the capacity. In addition, carbon can stabilize the SEI layer and participate in the electrochemical cycling as well. However, the lower silicon-to-matrix ratio and issues with particle agglomeration during the cycling have slowed down considerable interests in the approach. Another approach that is currently gaining momentum is the use of nanostructured silicon materials [21], [22]. When the material is scaled down to "nano" level, there are a myriad of advantages that can be exploited. First of all, the lithium storage kinetics can be greatly enhanced by decreasing the size of the electrodes as the distance over which $Li^+$ has to travel is minimized as according to Fick's Law, which is given as follows:

$$\tau = \frac{L^2}{2D} \tag{1.15}$$

Here, $\tau$, $L$ and $D$ represent mean diffusion time, diffusion length, and diffusion coefficient, respectively. The faster rate of lithium diffusion across the short length scale of electrode materials can be beneficial for the high charge/discharge rates necessary for high power applications. Secondly, the high surface-to-volume of the nanostructured material ensures high contact area between the electrode and electrolyte. Typically, bulk silicon electrodes lack large surface sites for higher electrochemical activity and take longer times to fully lithiate and delithiate. In addition, the large number of defect sites present in the bulk has the greater tendency to trap lithium ions, contributing in the huge irreversible capacity of the cell. Thirdly, the proper engineering of nanomaterials can better accommodate the volume expansion and eliminate the need for extra binders and additives, which can add significant mass in the battery.

Unfortunately, the nanostructuring of silicon creates additional challenges due to the large surface-to-volume ratio, which leads to a large surface area that can cause unwanted side-reactions with the liquid electrolyte. For example, the reduction of organic electrolytes during the charge transfer process can lead to the formation of a solid electrolyte interphase (SEI) layer that reduces lithium diffusivity and causes irreversible capacity loss. On the contrary, a thin SEI layer that only grows during the initial few cycles can instead form a permanent protective layer preventing further growth, while allowing $Li^+$ ions to diffuse readily between the electrode and electrolyte. This variety of SEI is regarded as an ideal compromise for battery applications [23], [24]. However, the notorious volume changes experienced by

silicon during electrochemical cycling can simultaneously weaken and tear the SEI layer causing the silicon to be directly re-exposed to the electrolyte with each cycle, thus re-forming a new SEI film. This repeated reduction and consumption of electrolyte during cycling can quickly thicken the SEI layer, consuming lithium from cathodes and impeding the further transfer of $Li^+$ ions across the interface. This instability in SEI formation can eventually lead to overall capacity loss and failure of the battery. Therefore, a better engineering of Si nanostructures, such as coating with inactive functional layers to prevent uncontrolled SEI formation could be an ideal strategy for the long-term stability of the electrode.

### 1.4. Nanostructured Silicon Electrodes

With discouraging performance from the bulk silicon anodes, the majority of recent studies have been focused on synthesizing and designing electrodes with nanostructured form. Ohara *et al.* tested the 50 nm thin film anodes deposited on Ni foil, and showed a stable reversible capacity of 3600 mAh/g for 200 cycles [25], [26]. They also found a strong correlation between the thickness of the silicon film and capacity loss per cycle [27]. However, the thin film technology utilizes less active material which means less amount of charge stored. Later, Kumta *et al*. demonstrated that the weak silicon-substrate interface bonding causes these films to delaminate after many cycles making it unsuitable for viable battery applications [28]. The use of silicon nanoparticles down to the size of 10 nm have shown to improve performance as the reduction in the size decreases the lithium diffusion path and lowers the internal stress associated with volume expansion [29]. However, the pressure induced by the volume expansion during the lithiation leads to agglomeration of the

nanoparticles [9]. As a result, the agglomeration of the particles increases the diffusion length, traps the SEI layers and causes huge irreversible capacity loss. Followed by numerous unsuccessful attempts of using nanoparticles and thin film materials, Chan *et al.* in 2008 reported pioneering work in which they used one dimensional silicon nanowire anodes directly grown on the current collector [30]. They reported a near theoretical capacity of 4200 mAh/g. The superior performance of silicon nanowire anodes was attributed to the large surface-to-volume ratio of the 1D nanostructure with no binders and additives. The spaces between the nanowire arrays provided adequate space for accommodating the large volume strain during cycling. Furthermore, the nanowire architecture of growing directly on the current collector provided a robust electrical contact for faster lithium ion transport. Despite all these advantages, the capacity still dropped to 3000 mAh/g immediately after the first cycle and lasted for only few cycles even at the low rate of C/20.

To circumvent this issue, several researchers have undertaken the approach of mere tweaking and redesigning of the nanostructured architecture. Nanotubes [31], [32], nanopores [33], core-shell [34], templates [35], and nanocables [36] are some of the few techniques being pursued in order to improve the performance of silicon based anodes. An overview of various one-dimensional silicon nanostructures studied have been thoroughly documented in the following recent review articles: [13], [24], [37].

## 1.5. Goal of the Dissertation

It is clear from the majority of studies conducted on silicon nanostructures that battery performance has not been able to reach the mark above a few tens of cycles. While much of the research effort has been focused on materials selection, cell design and evaluation of cell performance, relatively few studies have been dedicated to understanding the fundamental aspects of materials behavior and kinetics during the battery operation. The systematic understanding of the structural changes and reaction mechanism is critical for determining the necessary steps that can be implemented to design the best electrode materials for battery application.

For this dissertation work, I present a real-time studies of individual silicon nanostructures achieved by developing a prototype nanoscale electrochemical cell platform inside the transmission electron microscope (TEM). This technique provides fundamental insights into the mechanics and kinetics of individual silicon electrode during electrochemical charge/discharge. The data and results obtained from this work can be valuable for the battery community to incorporate specific material choices and architectures into the design of future viable battery electrodes.

Various *in situ* techniques such as scanning electron microscopy (SEM) [38], X-ray diffraction (XRD) [39], Raman spectroscopy [40], and nuclear magnetic resonance (NMR) [41] are pursued to investigate materials' properties and reaction mechanisms used in batteries. However, most of them have some serious limitations. *In situ* TEM, is possibly the best technique for conducting real-time investigations of battery materials because it has the ability to capture images at the atomic-scale while during

the operation and testing. Additionally, it has the simultaneous ability to provide chemical and structural information of the material studied.

## 1.6. Organization of Dissertation

The organization of the thesis is as follows. In Chapter 2, I will discuss the experimental techniques where the basics of TEM and details on *in-situ* techniques are provided. Additionally, the synthesis process of silicon nanowires (SiNWs) using chemical vapor deposition (CVD) is presented. Chapter 3 provides various fundamental investigations conducted on silicon nanowire-based electrodes during lithiation and delithiation, as performed *in-situ* in TEM. Chapter 4 covers the study of heterogeneous structures featuring carbon nanotube (CNT) and amorphous Si ($\alpha$-Si). The mechanical reliability at the interface of CNT@ $\alpha$-Si is studied with *in-situ* TEM bending tests followed by detailed lithiation and delithiation experiments and results. Chapter 5 focuses on hollow silicon nanostructures, which provide insights on the engineering strategies to alleviate problems associated with volume changes during lithiation/delithiation and simultaneously controlling the formation of excessive SEI layers. Finally, in Chapter 6, the scope of the work is summarized and future direction for the research are outlined.

# Chapter 2: Experimental Techniques

## 2.1. Transmission Electron Microscopy (TEM)

### 2.1.1. Background

Transmission electron microscopy (TEM) is a powerful tool which manipulates electrons to extract information such as topography, morphology, structure, and chemical composition from the selected region of the sample. It was first introduced in 1931 by Max Knoll and Ernst Ruska, and later commercialized in 1939 [42]. Before going through the details about the operation of TEM, it is important that we understand the following two terms:

a) Magnification: It is the ratio between the size of the image formed and actual size of the object.

b) Resolution: It is the smallest possible detail that can be resolved in an image. It is usually measured in the units of distance, $d$ (Å). The smaller the distance measured, higher is the resolution. The ultimate resolution is determined by the wavelength $\lambda$ of the source, and is defined by Rayleigh criterion:

$$d = 0.6 \times \lambda \qquad (2.1)$$

The smaller the wavelength of the source, the higher is the resolving power. The $\lambda$ in the visible region of the spectrum falls within 400-700 nm. So, the resolution limit of the light microscope is around 200 nm and the magnification greater than 1000X cannot be resolved by human eye.

In 1924, Louis de Broglie hypothesized that electrons can behave like waves, and that the wavelength of the electron beam can be significantly reduced by increasing the accelerating voltage. The hypothesis was later verified experimentally by two independent groups from U.S. (Davisson and Germer) and U.K. (Thomson and Reid). This discovery led to idea that electron beam could be potentially used as a source in the microscope. In 1927, after Busch showed that it is possible to focus electrons using electrostatic fields, it basically stimulated the field of electron optics, which continues to this day.

The modern TEMs are typically operated at acceleration voltages *V* ranging from 60-300 kV. The wavelength $\lambda$ of the electron can be determined using the following non-relativistic relation:

$$\lambda = \frac{h}{\sqrt{2meV}} = \frac{12.26}{\sqrt{V}}\text{Å} \qquad (2.2)$$

Where *m, e* and *v* are mass, charge and velocity of electron, respectively. For 200 and 300 kV electron microscope, the electron wavelengths are therefore 0.02508 and 0.01969 Å, respectively. These electron wavelengths are about 100 times smaller than typical distances of atoms in solid. The resolution of a modern TEM is limited by lens aberrations around 1- 2 Å., which is basically 1,000 times greater than the light microscope and about 500,000 times greater than that of a human eye.

### 2.1.2 Basic Parts and Operation of TEM

TEM basically consists of five parts: electron gun, condenser-lens system, specimen stage, objective-lens system and imaging system (see Figure 2.1).

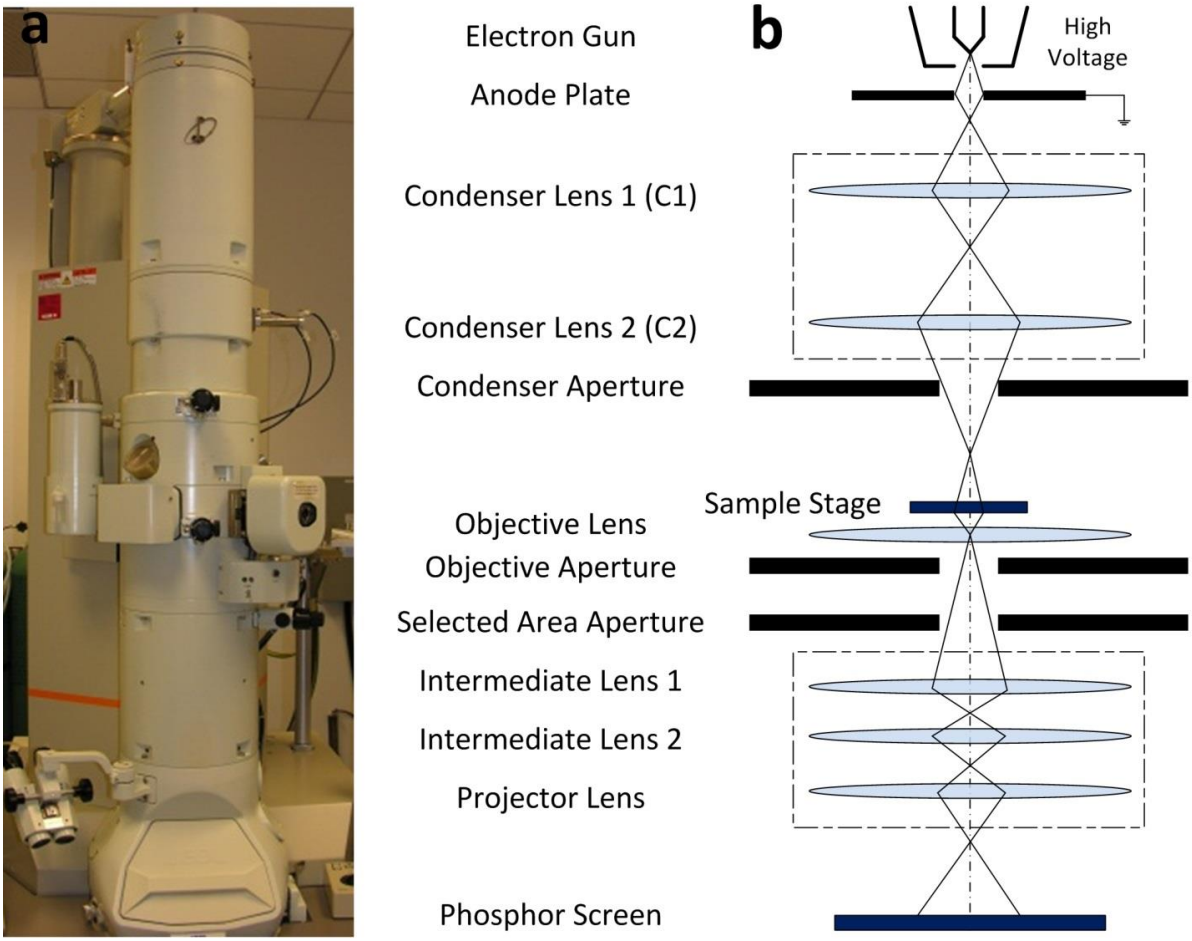


Figure 2.1: (a) A JEOL $LaB_6$ TEM. (b) A schematic representation of electron optics in TEM. Figure (b) adapted from Ref. [42].

i) Electron Source

The electron source (or gun) produces a beam of electrons with high kinetic energies, which allows them to pass through the transparent region (typically < 0.5 μm) of the sample. The gun assembly consists of a cathode and an anode (Figure 2.2).

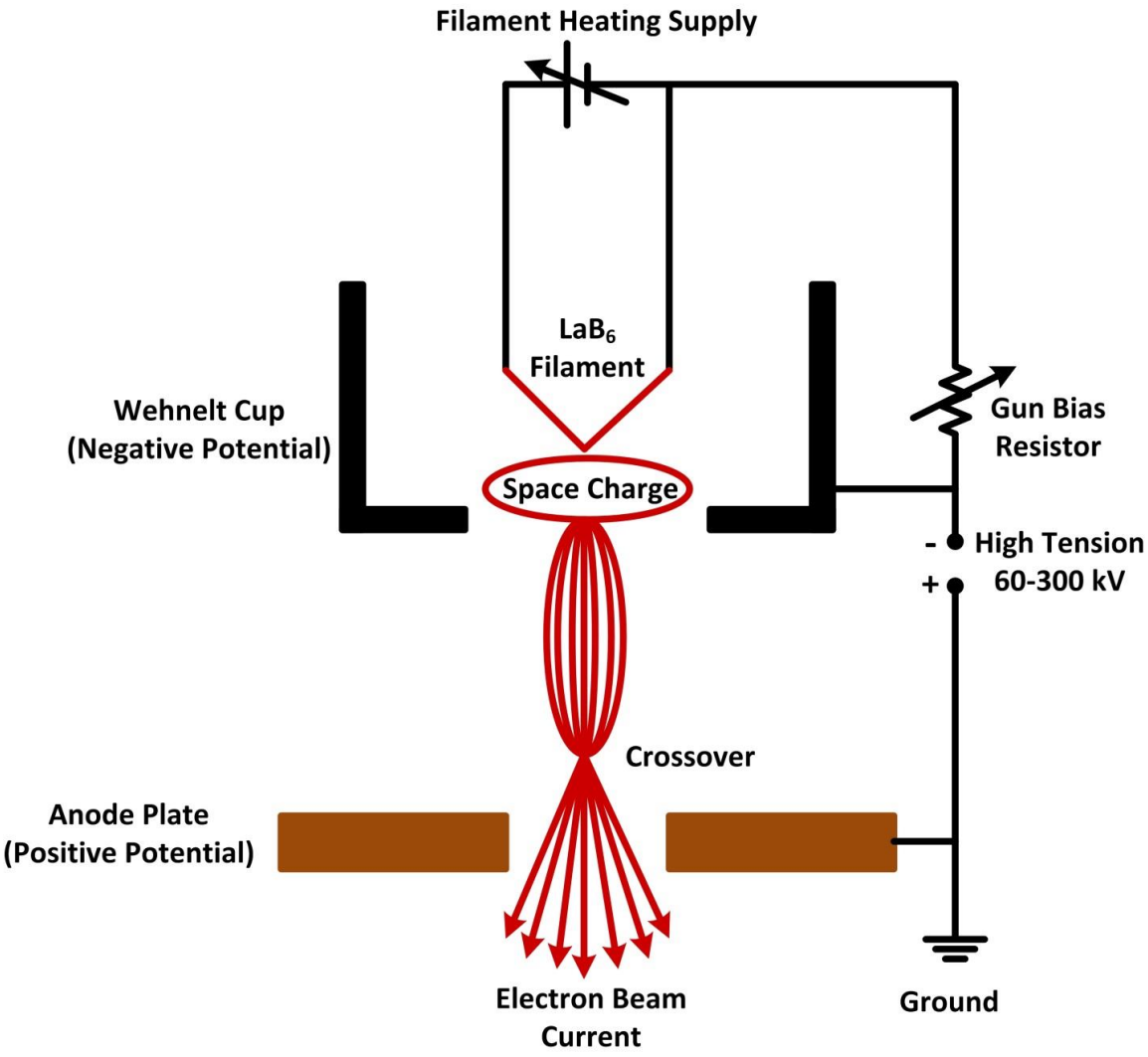


Figure 2.2: A schematic diagram of thermionic electron gun source ($LaB_6$) generating beam current. Figure adapted from Ref. [42].

A cathode source is either tungsten filament or Lanthanum Borate ($LaB_6$), which produces electrons through thermionic emission (TE). There is also another source with a very fine tungsten tip (radius r < 100 nm) called field emission (FE) [42]. The FE allows for the electrons to tunnel through the tip with high probability and thus increases the current density and brightness of the beam probe. FEGs are suitable for high-resolution imaging. The electrons produced by the cathode are then concentrated

around the region of a negatively charged Wehnelt Cup called space charge. The positively charged anode plate underneath the cup attracts the electrons. The electrons exit though the central hole of the cup (typically ~ 1% of total electrons in TE) [43] and accelerate down to the column. The TEM column is maintained under high vacuum pressure using oil diffusion pumps and rotary pumps. A high vacuum is necessary so that the accelerated electrons are not scattered by the remnant gas and water molecules inside the TEM.

ii) Condenser-lens system

Typically, an electron lens is made of hollow (bore) soft-iron magnet (polepiece) with copper wire coils around it (Figure 2.3). The current passing through the coil creates a magnetic field in the bore and the resulting Lorentz force deflects the electrons in the spiral trajectory. The magnetic field works like the convex lens in the optical lens system, where the off-axis electrons are brought to the focus. However, the image formed by the magnetic lens is inverted and rotated. The degree of rotation of the image depends on the strength of the lens. Thus, the magnification or the focal length of the electron lenses can be changed by varying the current passing through it.

The purpose of the condenser-lens system is to focus the electrons beam into the specimen. For TEM, the beam can be spread; but for scanning TEM (STEM), the beam is focused.

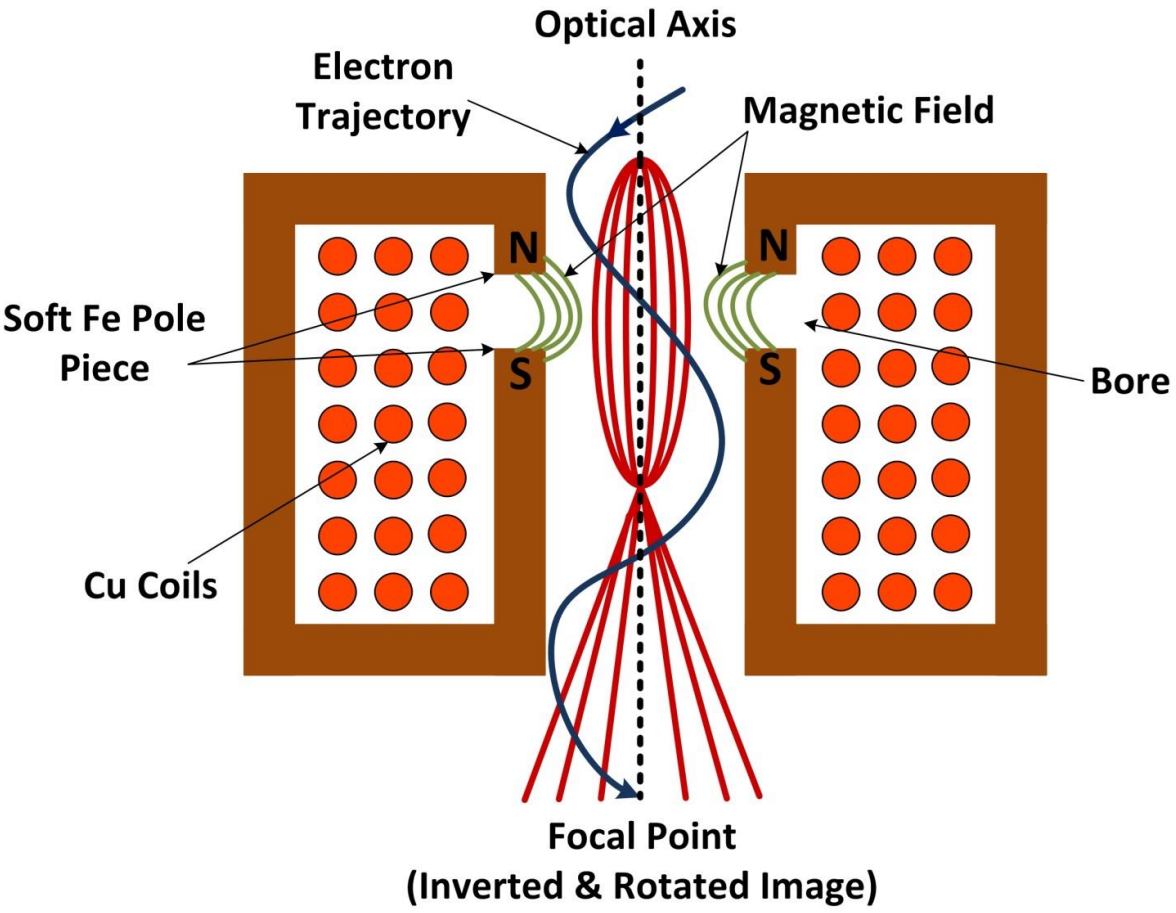


Figure 2.3: Schematic showing electron trajectory in the electromagnetic lenses. Figure adapted from Ref. [42].

The condenser-lens system consists of at least two electron lenses. The first condenser (C1) lens is a strong magnetic lens with a lower focal length *f* (< 2 mm) and concentrates and demagnifies the electrons coming from the gun. Often, lens aberration such as a spherical aberration (scattering at different angles) and a chromatic aberration (scattering at different wavelengths) can cause incoherency in the beam. These aberrations should be corrected or else can compromise the final resolution of the image. The second condenser (C2) lens is a weak magnetic lens (higher *f*) and converges the beam that passes through the aperture without affecting

the magnification. The focus condition of the image can be changed by changing the current in the C2 lens. If the current is increased, overfocused imaged is formed; while the decrease in the current can lead to underfocused image. During both conditions, the condenser aperture should be correctly aligned to the optic axis to compensate for the changes.

iii) Specimen stage

The specimen stage consists of a holder designed to be free from any mechanical vibration or drift and should be airlocked during the TEM operation. The sample is positioned on the top-end of the holder, and is directly in the electron beam path. When the electron beam interacts with the specimen and transmits through it, three following conditions may typically occur:

a) The electrons are transmitted without scattering, called zero-loss.
b) The electrons are elastically scattered (no loss of energy), called diffracted beam.
c) The electrons are inelastically scattered (a loss of energy).

The transmission of electrons depends on the thickness of the specimen. The thicker part will cause more electrons to scatter and image appear to be darker and *vice-versa*. Any electron scattered or deflected by an angle $\theta$ can satisfy Bragg's Law and give structural information such as orientation, atomic arrangements and phases present in the selected area of the specimen. These scattered electrons appear in the form of spots, called diffraction spots, and each spot corresponds to a specific atomic spacing or a plane.

The electrons that are inelastically scattered loose energies during the interaction with the atoms of the specimen. These energies can be detected and analyzed by the spectrometer attached to TEM to extract chemical information such as elemental composition and distribution. This method is referred to as electron energy loss spectroscopy (EELS).

iv) Imaging system

The imaging system comprises of three lens systems: objective, intermediate and projector. The purpose of the imaging system is to magnify the image or the electron diffraction produced after the beam interacts with the specimen.

The objective lens is located immediately below the specimen stage (Figure 2.4). The lens has small *f* and focuses the parallel beam of electrons emerging from the specimen in the back focal plane (bfp). An electron diffraction pattern (EDP) is formed at the bfp. Two different apertures, objective and selected area, can be inserted to select the mode of imaging, diffraction pattern or image, as shown in Figure 2.4. The objective aperture also improves the image contrast by blocking the inelastically scattered electrons from the specimen.

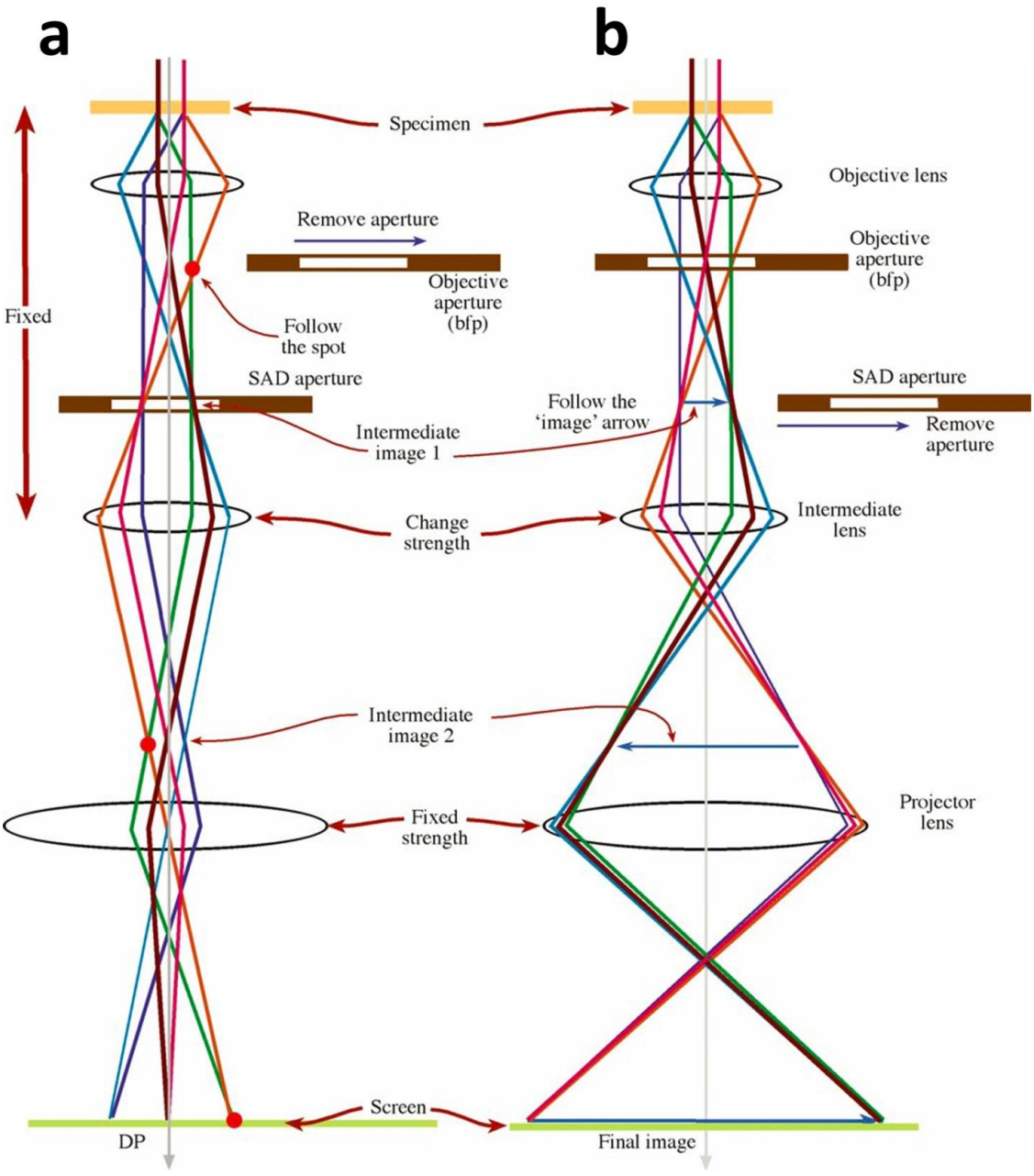


Figure 2.4: Two modes of imaging in TEM. (a) Diffraction pattern (DP) mode, and (b) Imaging mode. Adapted from Figure 9.12 of Ref. [42].

The intermediate lens magnifies the image by changing the *f* in small steps. By doing this, the magnification of the TEM images can be varied over a large range, from $10^3$ to $10^6$ [43].

Finally, the projector lens produces an image or a diffraction pattern over the entire TEM screen with diameters as large as several centimeters. The image produced can also be viewed in computer screen or captured using CCD camera.

### 2.1.3. *In-Situ* TEM

*In-situ* TEM is a powerful technique which allows to observe and to record the dynamic processes occurring in the specimen under various stimuli in real-time. The significant improvements achieved in both the spatial and temporal resolution of TEM have made *in-situ* technique an inevitable tool to study the fundamental properties of materials. However, the technique has several challenges. One of them is the limited space available for manipulating the sample in the TEM. Typically, the gap between the two pole pieces of the objective lens in the specimen region is 2 mm. The gap between the polepieces cannot be widened as it compromises TEM resolution and is also economically unfeasible. Additionally, the depth of focus in TEM is so small, moving the sample around can be a huge challenge. Furthermore, the conventional TEM holders are built solely for TEM/STEM imaging of the sample. No external conditions or stimuli can be applied using these holders. The external stimuli may include electrical, mechanical, thermal, electrochemical, liquid, gases, etc. A typical in-situ TEM holder should overcome all of the above challenges. The specialized TEM holder built by NanoFactory Instruments™ has the capability of imaging while manipulation (Figure 2.5). It has a compact piezoactuated STM probe

built within the holder and is capable of precise manipulation within a small gap between the objective pole pieces in TEM. The probe can be used to study both the electrical and mechanical properties of sample, thereby allowing the observation of structural, morphological and chemical changes, simultaneously.

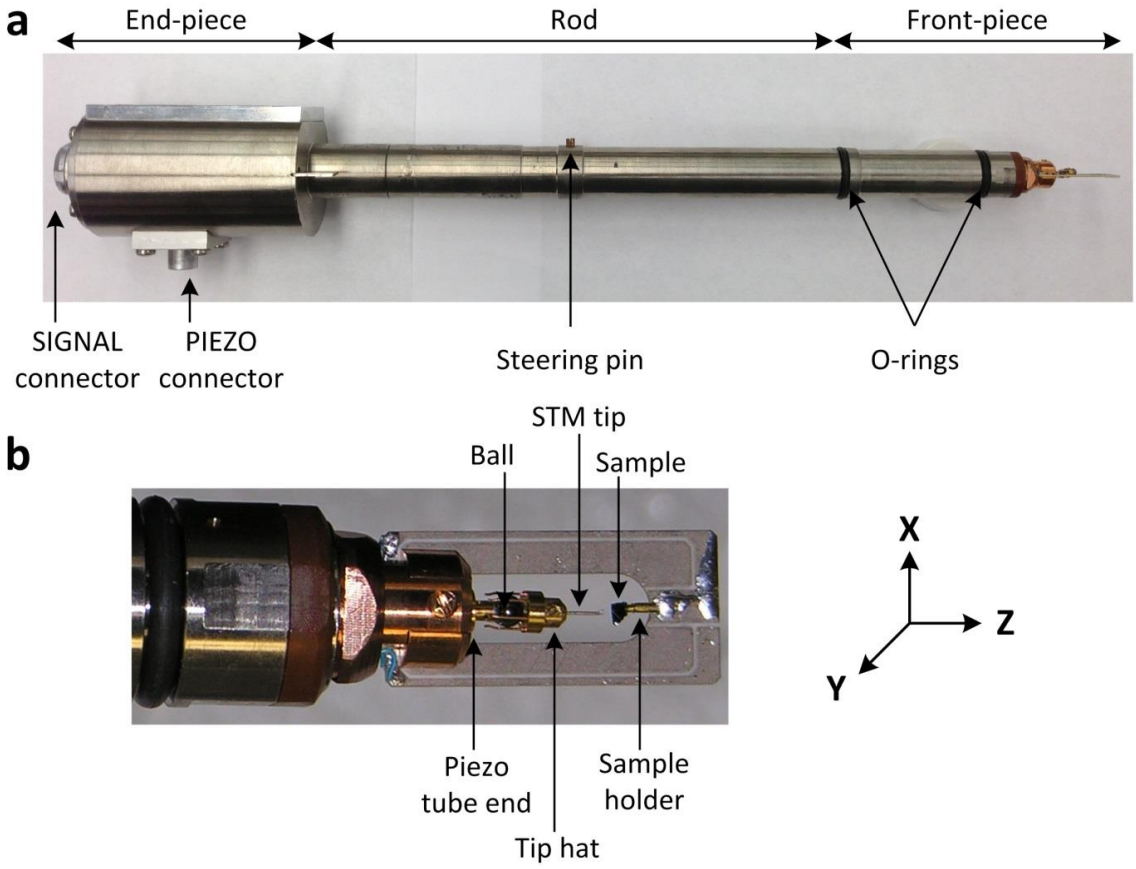


Figure 2.5: (a) NanoFactory™ STM-TEM manipulation holder for JEOL TEM. (b) Front-piece with tip hat and sample

Figure 2.5 a shows the STM-TEM holder designed to fit in both JEOL $LaB_6$ and JEOL FEG TEM goniometer. The holder consists of three main parts, the end piece (with the connectors), the rod and the front-piece. The SIGNAL connector provides

signals for excitation and measurements. The PIEZO connector controls signals in the piezoelectric tube. The front-piece contains the three-dimensional positioner system (Figure 2.5 b) fitted with the piezoelectric tube. The end of the piezoelectric tube has a sapphire ball with conductive coatings. A six-legged tip holder called "tip hat" is placed directly on top of the ball. A STM wire ($Pt_{0.8}Ir_{0.2}$, 0.25 mm diameter, Agilent Technologies) is attached to the tip hat and it acts as a manipulation probe. On the other side of the ceramic front-piece, is a sample holder and is fixed. During the manipulation, the STM tip probe can move in all three dimensions (X &Y: 3 mm X 3 mm, Z: 1.5-2 mm) using the inertial slider mechanism [44]. The movement both in lateral (X) and forward/backward (Z) directions are easy to control and are visible in TEM. Since the Y-positioning is along the direction of the electron beam, positioning the STM tip to the eucentric height is difficult. The best approach is to align the height of the sample to the eccentric point first, and then the STM tip, using both coarse and fine motion of the positioner as necessary.

## 2.2. Nano-Electrochemical (Nano-Battery) Assembly

For the prototype nanobattery assembly, individual silicon nanostructures either directly grown or cantilevered on the TEM grid substrate are attached (or glued) to the fixed sample holder (Figure 2.6). The protruding nanowires or nanotubes from the substrate should be placed in such way that they are directly in the path of electron beam illumination. The piezoactuated STM manipulation tip carries a piece of lithium metal, which acts simultaneously as a Li source, a reference electrode, and a counter electrode. A thin layer of native $Li_2O$ that forms due to the residual vacuum of the microscope serves as a solid electrolyte, allowing the diffusion of $Li^+$ between the

electrodes under potential bias [45]. Typically, lithiation and delithiation are performed by applying biases of -2 V and +2 V (*vs.* Li metal) to the nanostructured sample, respectively.

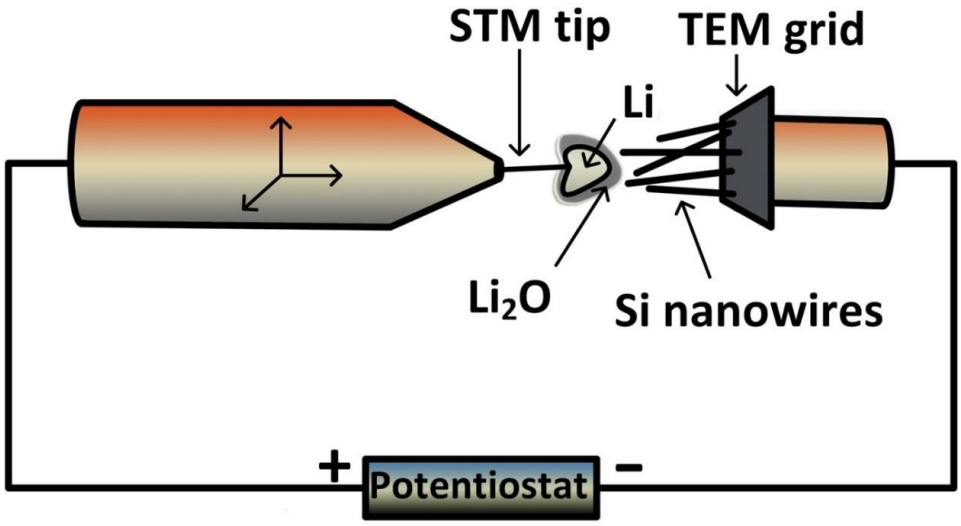


Figure 2.6: A schematic representation of the electrochemical setup inside TEM. Adapted from Figure 1 of Ref.[45].

## 2.3. Synthesis and Characterization of Silicon Nanowires (SiNWs)

### 2.3.1. Chemical Vapor Deposition (CVD)

The SiNWs used in this study [45] are grown from the (111) Si surface at the edge of a window in a silicon nitride ($Si_3N_4$) TEM membrane (SPI supplies) using the bottom-up vapor-liquid-solid (VLS) technique (Figure 2.7) [46].

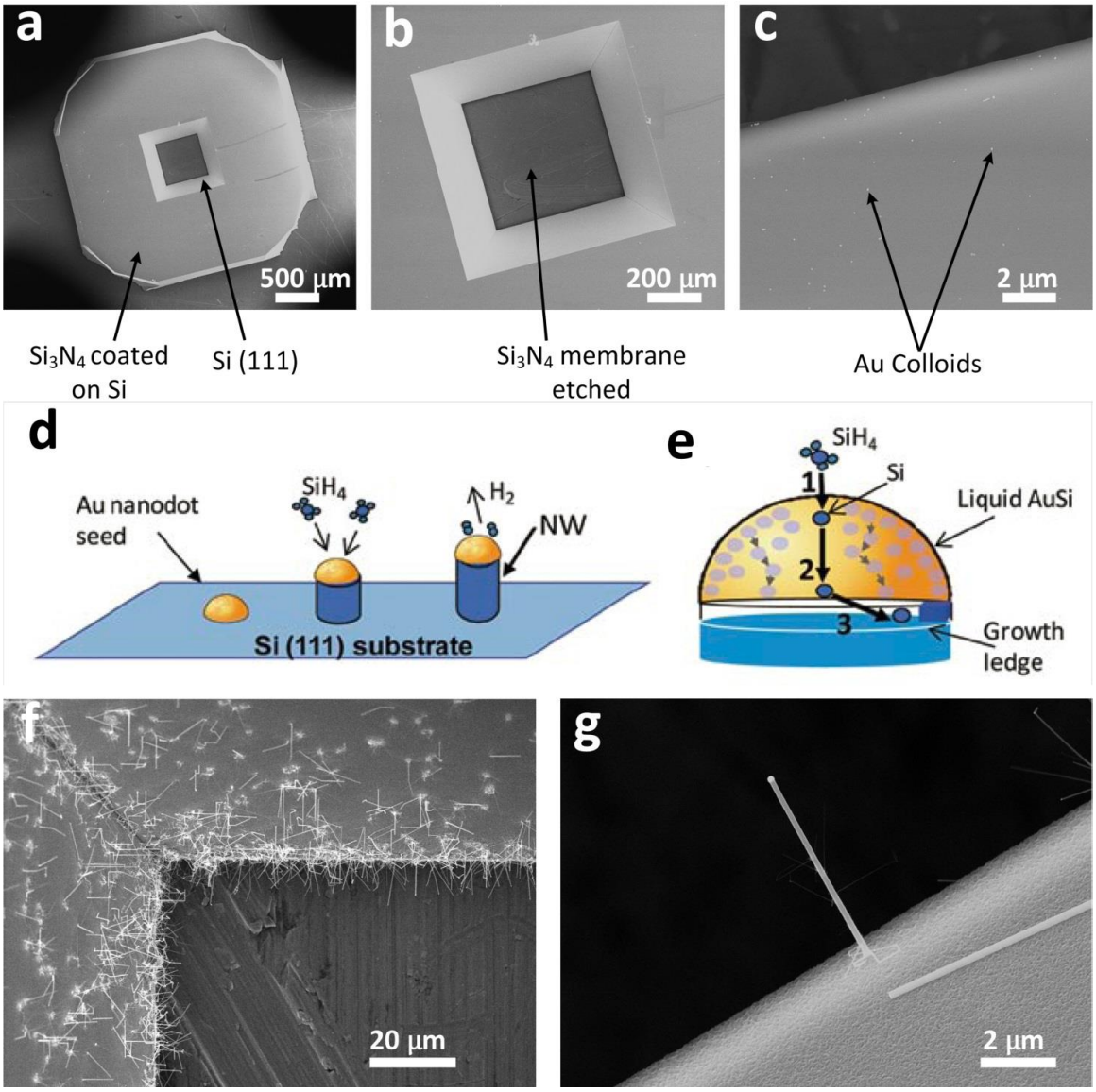


Figure 2.7: Vapor-liquid-solid (VLS) growth mechanism for SiNW on TEM grid window. (a) SEM image of TEM grid having dimensions of 200 µm x 200 µm. (b) The inner and outside square dimensions of the central window region of TEM grid in (a) are 0.5 and 0.75 mm, respectively. (c) Au-colloid seeds dispersed on the window edge as shown in (b). (d) A schematic of VLS SiNW growth from a liquid Au catalyst seed which floats on top of NW as it grows and defines the growth diameter. (e) A schematic showing the enlarged view of the liquid Au and solid NW interface

and three kinetic steps for NW growth: (1) $SiH_4$ decomposition at the vapor-liquid interface, (2) Si atom diffusion through the AuSi liquid, and (3) NW crystallization. (f) Low magnification SEM image of SiNWs grown on the TEM grid window. (g) High magnification SEM image individual SiNW with Au on the top. Figures (d & e) adapted from Ref.[46] and Figures (f & g) from Ref. [45].

The dimensions of the TEM-grid window are 200 μm x 200 μm with a 100 nm thick silicon nitride membrane (Figure 2.7a, b). In order to break the membrane, the TEM grid is sonicated for 5 s. Gold colloids (100 nm diameter) are then dispersed around the edge of the TEM window (Figure 2.7c). The samples are loaded in a CVD (Atomate Corp.) reactor, and the temperature is set to 490˚C in order for the gold colloids to form a eutectic mixture with Si (Figure 2.7d, e). Silane (50 % $SiH_4$ in $H_2$) and phosphine (100 ppm $PH_3$ in $H_2$) are introduced into the chamber simultaneously with the flow rate of 250 sccm and 100 sccm respectively with a chamber pressure of 3 Torr. The growth time is about 10 minutes with the resulting nanowires ~10 μm in length and 100-150 nm in diameter (Figure 3.8f, g).

### 2.3.2. Growth Orientation of SiNWs

The growth orientation of the SiNWs can be determined by a two-tilt diffraction technique in TEM [47], as schematically shown in Figure 2.8a.

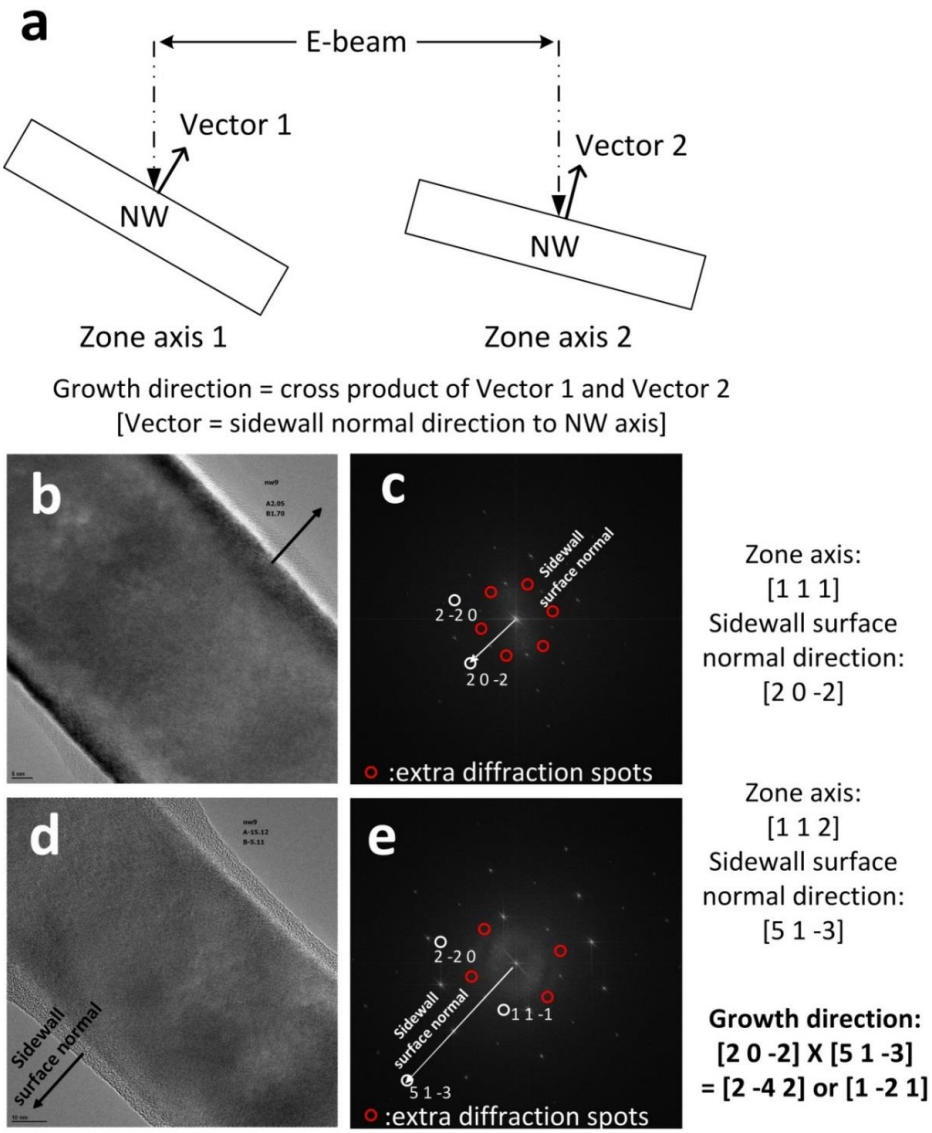


Figure 2.8: A two-tilt diffraction technique to determine the growth orientation of NW. (a) A schematic showing NWs in two different zone axes. (b) TEM image of NW as observed in a zone axis of [1 1 1] with (c) electron diffraction spots. (d) TEM image of NW as observed in a zone axis of [1 1 2] with (e) electron diffraction spots. A cross-product of sidewall surface normal directions from (c) [2 0 -2] and (d) [5 1 -3] to NW axes gives a growth direction of [1 -2 1]. Figures (b-e) courtesy of Tom Picraux, LANL.

The technique assumes that two different planes parallel to a cylinder should intersect along a line parallel to the cylinder axis. A plane parallel to the nanowire axis is identified and indexed using electron diffraction (ED) spots. These ED spots are perpendicular to the NW axis (Figure 2.8b-e). The NW is then tilted to different zone axis and the process is repeated. The crystallographic growth orientation is then calculated from the cross product of the Miller indices of these two planes.

# Chapter 3: Silicon Nanowires

## 3.1. A Real-Time Lithiation Study

### 3.1.1. Introduction

LIBs have become the dominant power sources for portable electronics and EVs. The current graphitic-based anodes suffer from limited energy density of 372 mAh/g. There is an ongoing and relentless search for the materials with high-energy and high-power densities. Recently, silicon has attracted significant interest owing to its highest theoretical capacity of 4200 mAh/g. However, bulk silicon used as an anode electrode has numerous reported failures due to stress induced cracking associated with a huge volume expansion of 300-400%, consequently leading to irreversible capacity fade [2], [10], [13]. To circumvent this issue, Chan *et al.* [30] used silicon nanowires, reporting charge capacity close to the theoretical value. However, even with the 1D nanowire geometry capable of efficient electron transport and facile strain relaxation, total charge capacity retention faded after a few cycles.

It is evident from this result that nanostructures of silicon anodes have advantages over the bulk for use in LIBs. However, the result is still far from what is needed to benefit battery production and use. The real challenge is to understand its fundamental aspect, as to how such nanostructures can maintain structural integrity and chemical function under certain phase changes, and yet fail after a few cycles. Various studies have been focused on addressing this issue by tweaking fabrication techniques and cell designs on the silicon nanowire material in the form such as

crystalline- amorphous core-shell [48], [49], and carbon-silicon heterostructures [31], [32], [50]–[52], etc. Despite these efforts, the success in improving the overall capacity for long cycle remains a key challenge. Therefore, it becomes important that we fundamentally understand the complex phenomena that occur in various components of battery during the charge and discharge cycles.

### 3.1.2. *In-Situ* Lithiation of Silicon Nanowires

The first test of the nano-battery is performed with individual silicon nanowires (SiNWs) as working electrode (Figure 3.1). The SiNWs are prepared from CVD technique using VLS method discussed in Chapter 2 (Section 2.3.1). The diameters of the nanowires range from 100 to 160 nm, while the length vary a few microns. Typically, the NWs have the growth direction of [112] as discussed in Section 2.3.2 of Chapter 2.

The schematic of the nano-battery setup is shown in Figure 3.1 a. Initially, the pristine SiNW is brought in contact with the lithium metal probe having little or no $Li_2O$ layer (Figure 3.1b). The SiNW is then mechanically forced to break the $Li_2O$ layer and short-circuited with lithium (equivalent charge rates would be ~100C-1000C). Within few seconds, lithium propagates from the tip of the NW progressing towards the substrate (Figure 3.1 c). Upon complete lithiation, silicon undergoes huge volume change and forms a crack along the NW axis (Figure 3.1 c, d). The crack is seen as a light contrast along the axis of the NW.

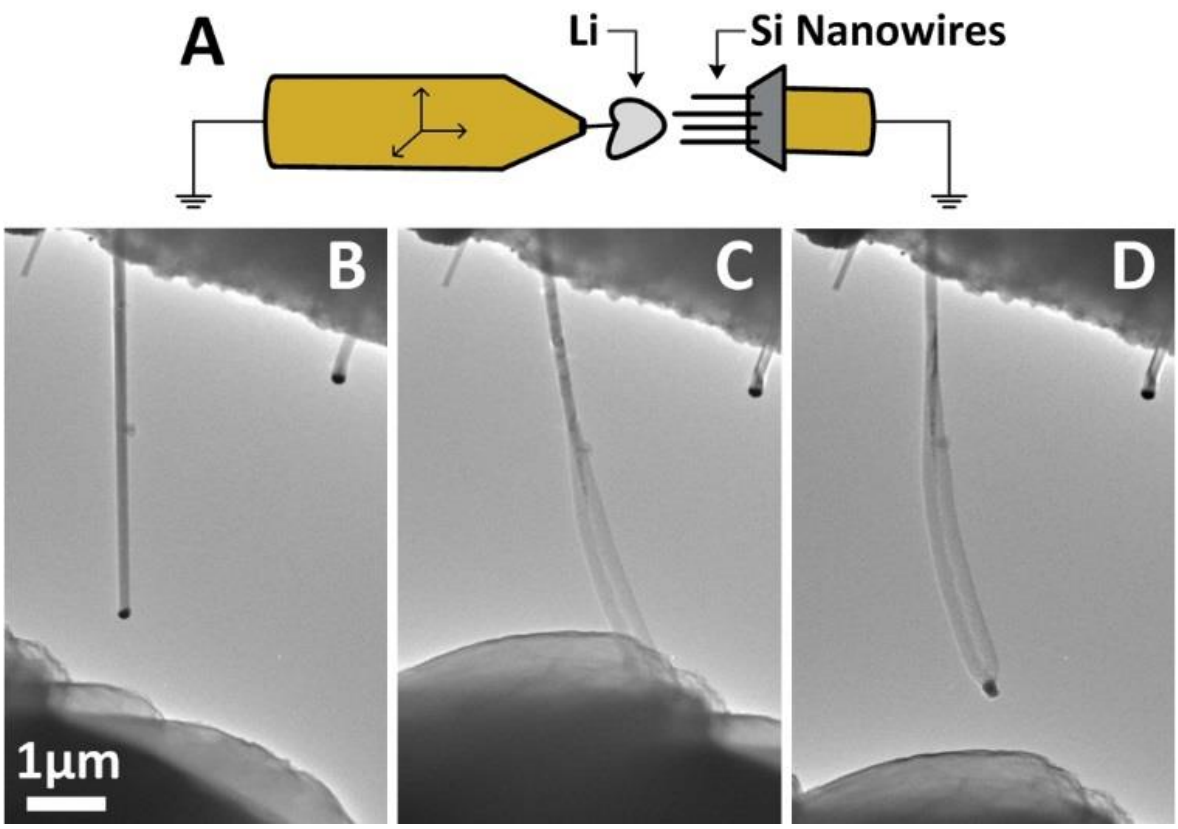


Figure 3.1. Real-time lithiation of pristine silicon nanowire in the TEM. (a) A schematic showing the setup of a lithiation process. A lithium metal source is brought into contact with a crystalline SiNW (*c*-SiNW) using a piezo-actuated STM tip with three degrees of freedom. (b) A mobile lithium source probe approaching a fixed *c*-SiNW just before lithiation. (c) Li alloying with Si, inducing axial crack propagation and volume change. (d) A lithiated NW after removing Li source.

### 3.1.3. Anisotropic Lithium Diffusion and Volume Expansion

*Adapted from Ref.* [53]

Interestingly, the nature of volume expansion during lithiation in Si is anisotropic and it forms cross-sectional dumb-bell shape upon deformation (Figures 3.1 and 3.2). Our collaborative effort with Sandia National Lab concluded that there is a strong orientation dependence diffusion of lithium in the crystalline Si [53], which is comparable to anisotropic Si etching in the semi-conductor industry [54], [55].

In this case, a naturally grown $Li_2O$ layer (~700 nm) formed during the brief exposure of lithium metal in air, served as a solid electrolyte. As $Li_2O$ is insulating in nature and forms a significant barrier for $Li^+$ ions transport, a potential of -2 V is applied to the SiNW *vs.* the Li counter electrode to the initiate the lithiation process (Figure 3.2) [53]. The SiNWs in both cases (Figure 3.1 and 3.2) have the growth orientation along the [112] direction, usually with a 180˚ twin boundary parallel to the (111) plane (Figure 3.2, a-c). As viewed from the [110] direction, the expansion of a NW during lithiation is only 17 %, from the original 155 to 188 nm (Figure 3.2, d-g). However, tilting of the NW in the viewing direction [111] shows a much larger expansion from 155 to 485 nm (Figure 3.2, d & h). The expansion of the NW is found to be more favorable along the [110] direction (~170%) and less towards the [111] direction (~20%). It should be noted that fast diffusion along a common planar defect, a twin boundary parallel to the $(11\bar{1})$ plane, has no role in the anisotropic deformation because the twin boundary is parallel to the long axis of the dumbbell rather than the short axis. In fact, a single twin ($T_1$ or $T_2$) itself also undergoes anisotropic swelling upon lithiation. Similar results are reported on silicon pillars and microslabs by other

*ex-situ* experiments [56], [57]. For instance, Lee *et al.* [57] fabricated silicon nanopillars with different orientation as [100], [110], and [111] and reported that the nanopillars expanded significantly along the [110] direction. In contrast to the [110] direction, the nanopillars showed little expansion along the [100] and [111] directions. Therefore, anisotropic swelling in Si is intrinsic characteristics of Li-Si alloying regardless of any experimental conditions and cell geometries.

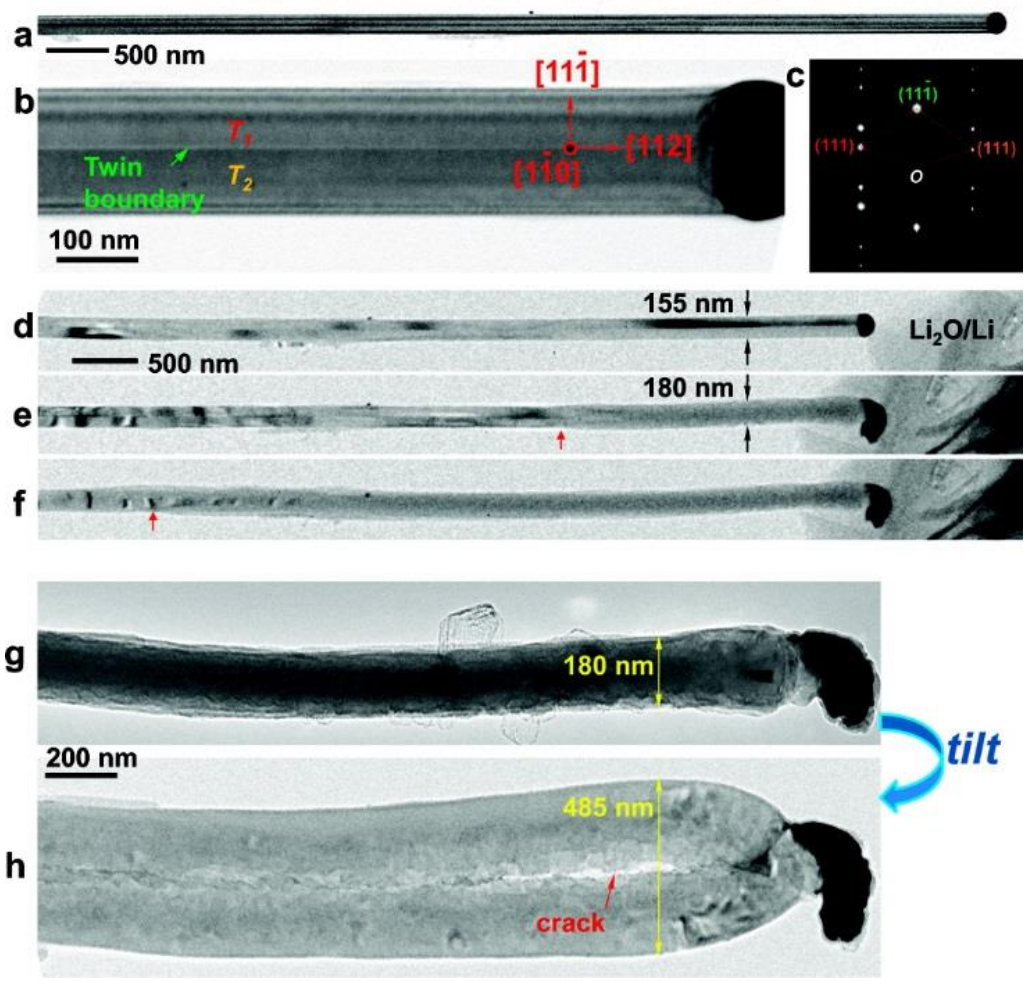


Figure 3.2. Anisotropic swelling and crack formation of Si nanowire during lithiation. (a) Low magnification image of pristine SiNW. (b) High magnification image of the pristine Si nanowire showing a twin boundary in the center. (c) Electron diffraction

pattern (EDP) of SiNW along the [110] zone axis. The axis of the nanowire was along [112], and the twin boundary was parallel to $(11\bar{1})$. (d–f) Lithiation of the Si nanowire with lithium propagation front (shown in red arrows). The visible diameter expansion was only 17% and no elongation was observed. (g, h) Lithiated nanowire in (f) viewed along $[110]_{Si}$ (g) and close to $[111]_{Si}$ (h) directions, respectively, showing the anisotropic volumetric expansion. Adapted from Figure 3 of Ref [53].

### 3.1.4. Thermodynamics and Phase Transformation

Another important phenomenon observed during the lithiation of SiNW is a two-step phase transformation during the alloying process. In theory, the equilibrium Li-Si binary phase diagram includes the formation of other possible intermetallic compound such as $Li_{12}Si_7$, $Li_7Si_3$, $Li_{13}Si_4$, and $Li_{22}Si_5$, of which $Li_{22}Si_5$ is the fully lithiated phase (Figure 3.3) [58]. However, with the *in-situ* TEM lithiation of NW, *c*-Si is initially transformed into amorphous $Li_xSi$ phase by a process referred to as solid state amorphization (SSA) [59]. The amorphous $Li_xSi$ phase is immediately followed by a fully lithiated polycrystalline $Li_{15}Si_4$ (*c*-$Li_{15}Si_4$) phase. This three-step process is confirmed by electron diffraction patterns (EDPs) of the pristine, lithiated and fully lithiated NW as shown in Figure 3.4.

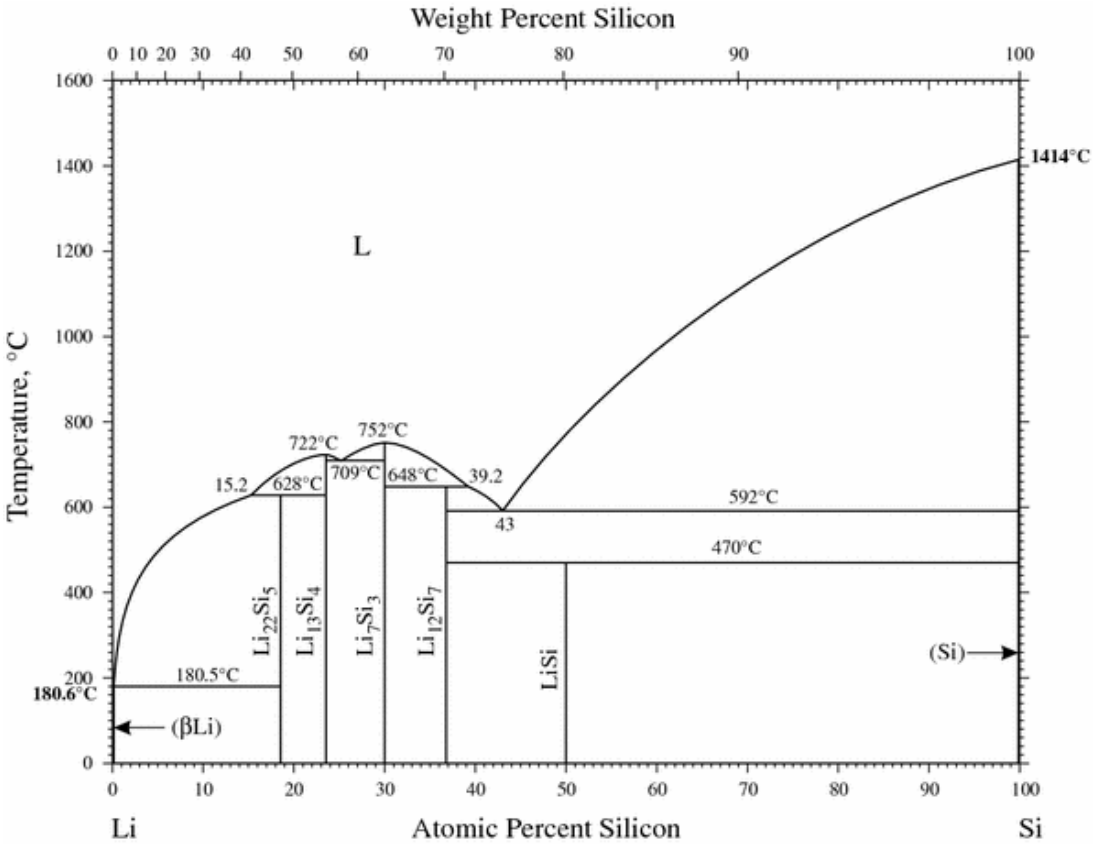


Figure 3.3: Lithium-silicon phase diagram assessed thermodynamically. Adapted from Fig.1 of Ref. [58].

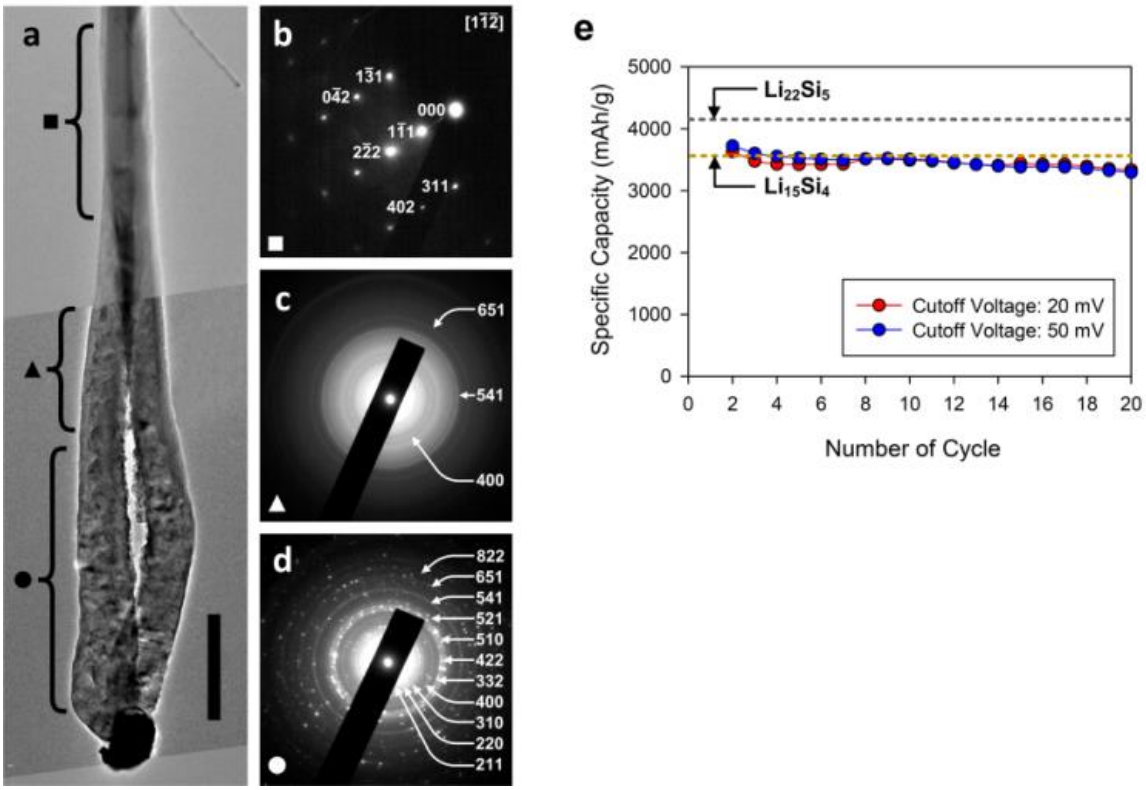


Figure 3.4: Evolution of the $Li_xSi$ structure during alloying. a) TEM image of a lithiated Si NW. This particular NW demonstrates a clear progression from unlithiated pristine Si, to mixed amorphous $Li_xSi$ to crystalline $Li_{15}Si_4$. The scale bar is 500 nm. b-d) SAED images of the regions indicated by symbols (■, ▲, and ●). b) Single crystalline Si, corresponding to the unlithiated NW region. c) Amorphous $Li_xSi$ region of NW with three sharp rings. d) Fully lithiated segment of Si NW, comprised primarily of $Li_{15}Si_4$ polycrystals. e) Cyclic specific capacity profile of Si NW anodes tested at room temperature and at a charging rate of 0.5 C. We observed maximum capacities of 3629 mAh/g and 3722 mAh/g at 20 mV and 50 mV cutoff voltages, respectively. Our results confirm that at room temperature, $Li_{15}Si_4$, rather than $Li_{22}Si_5$, is the fully lithiated phase.

Our results indicate that the fully lithiated phase of silicon at room temperature is *c*-$Li_{15}Si_4$ rather than the canonical $Li_{22}Si_5$. Identification of *c*-$Li_{15}Si_4$ as fully lithiated phase is made by matching the experimental *d*-spacings through EDP and the diffraction intensities with the simulated values for all known crystalline $Li_xSi$ phases. Figures 3.4a, b, and c show the electron diffraction patterns (EDPs) from pristine *c*-Si, *a*-$Li_xSi$ (x= 3.75) and *c*-$Li_{15}Si_4$ phases respectively, and are obtained during *in-situ* lithiation of SiNWs. This argument is also supported by our *ex-situ* electrochemical cycling result which shows that the highest capacity obtained with the silicon is close to the theoretical specific capacity of $Li_{15}Si_4$ (3579 mAh/g) at 20mV cutoff voltage and a charging rate of 0.5C (Figure 3.4e). There are a few other studies conducted by *in-situ* XRD studies which confirm the existence of similar $Li_{15}Si_4$ phase [60]–[62].

### 3.1.5. Summary

We performed real-time investigations on the lithiation and delithiation behavior of individual SiNWs, which allowed us to understand some of the fundamental processes associated with Si electrode materials. We observed that *c*-Si with [112] growth direction undergoes antistrophic volume expansion preferentially expanding more towards [110] direction compared to [111]. During lithiation of *c*-SiNWs, we also find that Si converts to $Li_{15}Si_4$ as a fully lithiated phase. These results could be beneficial towards the design consideration of *c*-Si based electrode for LIBs.

## 3.2. Formation of Nano-Voids during Delithiation

Another interesting phenomenon of nano-void formation is observed in SiNW during the electrochemical lithiation and delithiation (Figure 3.5). When the fully lithiated SiNWs are discharged at higher rate, we see nucleation of voids over time (Figure 3.5c). As the NWs are lithiated back, voids are refilled (Figure 3.5d). Upon subsequent lithiation and delithiation (Figure 3.5 e-g), we see a reversible formation of nanovoids similar to the previous study on Germanium nanowires (GeNWs) [63]. However, prior work clearly indicated the process may be isolated in the case of Ge because of its high intrinsic electrical conductivity. However, we believe that void formation could be the case in any alloy-based anodes. More investigations should follow to determine the fundamental understanding of the process.

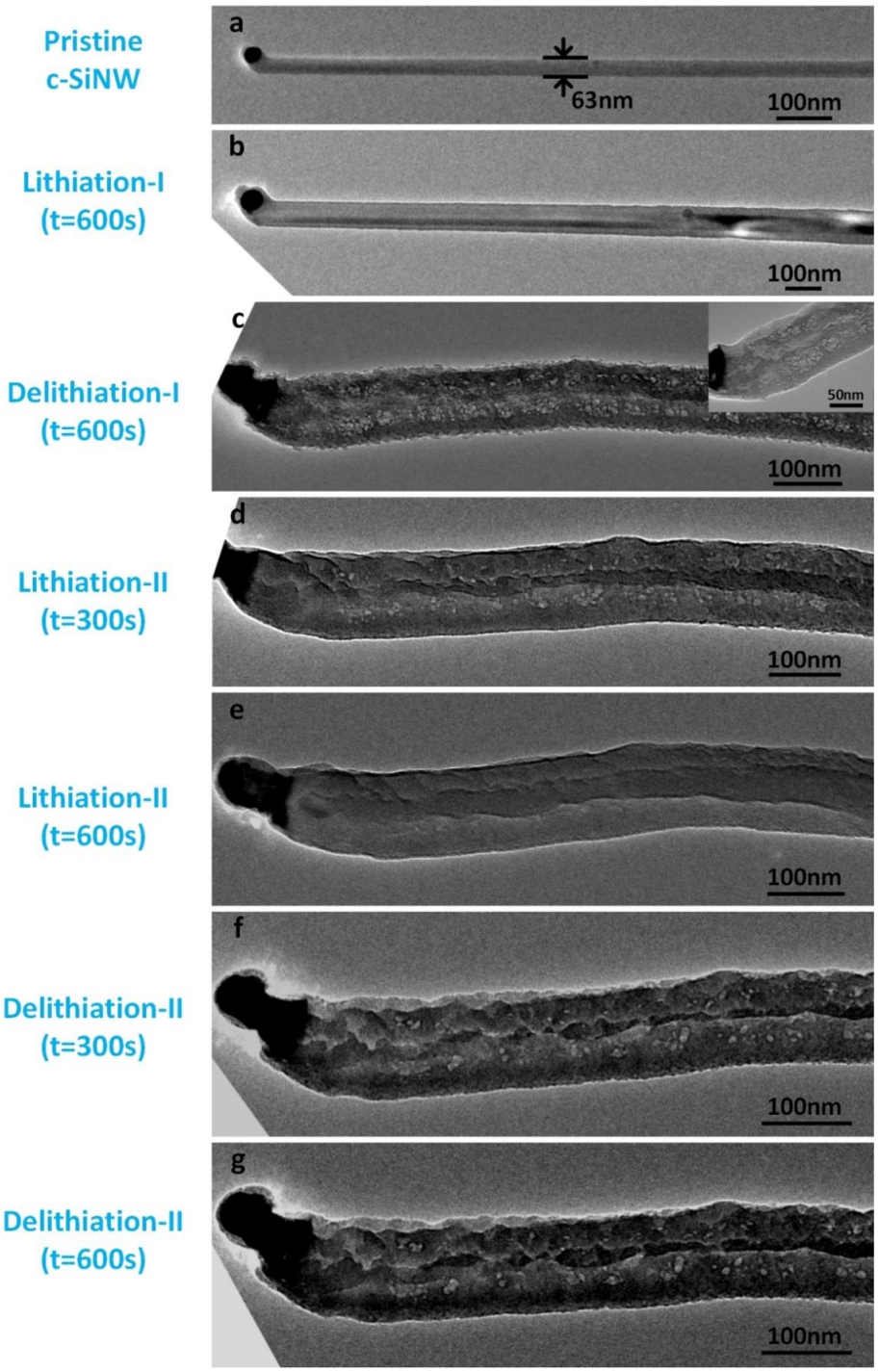


Figure 3.5: Cycling of *c*-SiNWs. (a) Pristine SiNWs with diameter of 63 nm. (b) Lithiation of SiNWs after a bias of -4 V with respect to Li metal is applied. (c) Delithiation of SiNWs when a bias of +4 V is applied.

## 3.3. Lithium-Assisted Electrochemical Welding at Si-Si Interface

*Adapted from Ref.* [45]

### 3.3.1. Introduction

Cracking and pulverization are known to be mitigated in part by nanostructured forms of silicon, but several recent studies, including ours [53], indicate that cracking can still occur in nanostructures subject to a variety of conditions [53], [56], [64], [65]. In contrast to this detrimental effect, we report an opposite effect, which may enable self-healing nanostructured Si-electrodes. While performing *in situ* TEM, we observe that contacted surfaces of otherwise physically distinct silicon nanowires are fused together after lithiation and delithiation. To date, there have only been a few post-mortem studies suggesting the occurrence of bonding and coalescence of nanomaterials in lithium battery electrodes [66]–[70]. For example, Li *et al.* [66] report the coalescence of Si nanoparticles from transmission electron microscopy (TEM) images of cycled and dismantled composite electrodes. However, direct evidence and a detailed understanding of the process are both still lacking. We here report *in-situ* TEM observations of the welding of physically-contacted silicon nanowires (SiNWs) during electrochemical lithiation and delithiation. Our data indicates that this welding phenomenon is predominantly an electrochemically-induced process, occurring at room temperature. Moreover, we demonstrate that the weld formed between SiNW surfaces is mechanically robust and exhibits evidence of facile transport of lithium ions, which are both desirable properties for enhanced battery performance.

3.3.2. Lithium Transport across Crossed-Contacted Silicon Nanowires

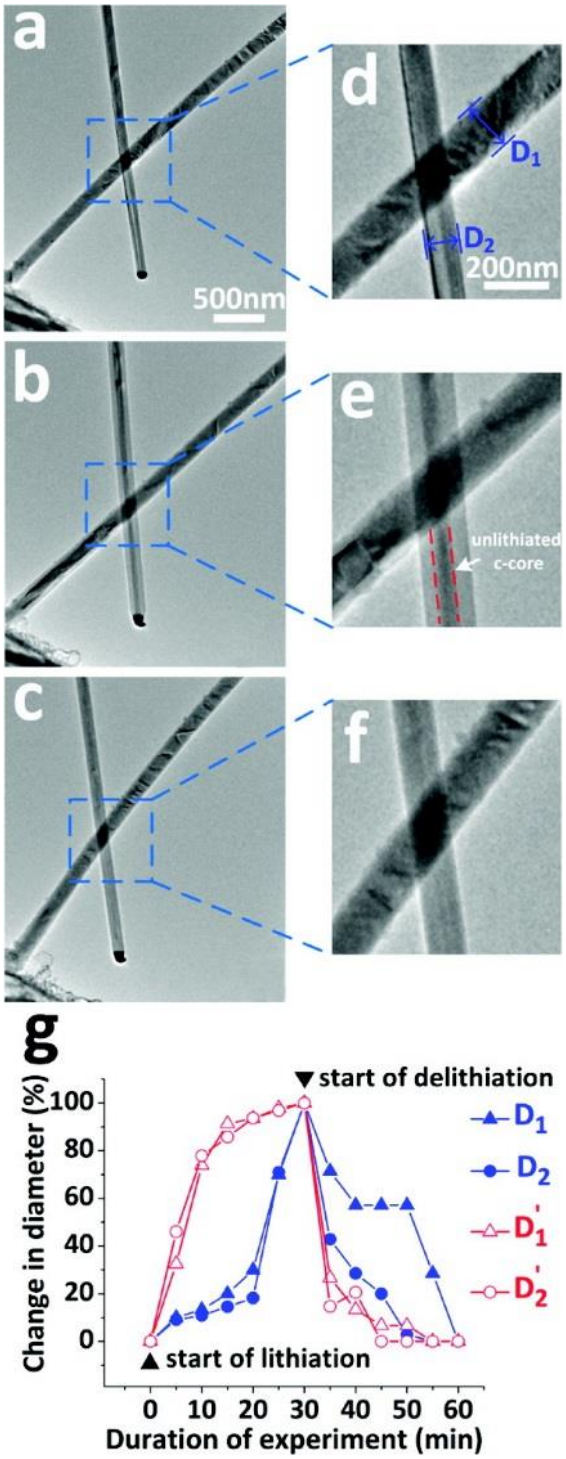


Figure 3.6. Lithiation and delithiation observed in crossed silicon nanowires. (a) Pristine nanowires. (b) Swelling of both nanowires after lithiation. (c) With

delithiation, both nanowires contract, however, and fail to reach the original volume. (d–f) Blown up images focusing on crossed part of nanowire representing panels a–c, respectively. The measured $D_1$ and $D_2$ diameters for d–f are (143, 98) nm, (167,148) nm, and (161,125) nm respectively. (g) Changes in diameter in the $D_1$ and $D_2$ section of the crossed SiNWs (Figure 3.6 d) plotted with respect to duration of experiment.

To investigate Li transport across contacted SiNWs, two separate nanowires are brought into contact with each other by bending one of them with the manipulator probe at 0V bias, as shown in Figure 3.6.

One nanowire with a diameter of 143 nm is contacted by the lithium source while the other with diameter of 98 nm remains isolated (Figure 3.6 a & d), contacted only indirectly, via the larger nanowire. Both nanowires are connected at the base to the silicon growth substrate. When a potential of -3 V with respect to lithium metal is applied to the silicon substrate, lithiation proceeds in the nanowire directly contacting the $Li_2O$, propagating in both the radial and axial directions (Figure 3.6 b & e). At the same time, we also observe lithiation advancing in the crossed nanowire, which is not itself contacting the lithium source. To test Li transport across the resulting interface of the two SiNWs, the diameter changes were subsequently monitored during delithiation by supplying the Si substrate with a bias of +3 V *vs*. the lithium metal source (Figure 3.6 c & f). As delithiation progresses, both nanowires are observed to decrease in diameter. We controlled the lithiation and delithiation times to make sure that the reaction front in the primary SiNW proceeded past the contact point of the two nanowires but did not reach to the Si substrate. Adjacent nanowires

that are not in contact with the lithiated nanowires show no lithiation behavior, also confirming that the lithium transport is indeed through the SiNW-SiNW contact and not, e.g. mediated *via* the Si substrate.

To test for any possible delay due to diffusion across the welded interface, we quantify the relative diameter changes of directly-contacted and indirectly-contacted nanowires during lithiation and delithiation, as shown in Figure 3.6 g. These experiments were conducted by applying the bias voltages and observing the nanowire evolution at video rates for approximately 15 seconds, periodically every five minutes during lithiation. At times between observations, the illuminating electron beam is blanked in order to avoid possible beam effects on the sample. We define the variable diameters of the directly-contacted and indirectly-contacted nanowires in the vicinity of the junction as $D_1$ and $D_2$, respectively, as shown in Figure 3.6 d. We also define a corresponding pair of diameters, $D_1'$ and $D_2'$, for another set of independent nanowires. Table 1 shows the diameters $D_1$, $D_2$, $D_1'$, and $D_2'$ of each respective SiNW in their pristine, lithiated and delithiated states. We calculate fractional diameter changes during the lithiation phase according to the ratio , and during the delithiation phase according to , where in both expressions, $D_P$, $D_L$ and $D_D$ correspond to the diameter of each SiNW in its pristine, lithiated and delithiated state, respectively, and $D$ represents the measured diameter as it varies with time. Using these expressions, we report the relative change in diameter of contacted nanowires as a function of time during lithiation and delithiation in Figure 3.6 g. These measurements were obtained from experiments, during which we lithiated each crossed-SiNW system for 30 min, and subsequently delithiated for 30

min. Using the incremental diameter changes of each nanowire, we qualitatively compare the lithium propagation rates among SiNWs. With the exception of a delayed contraction briefly exhibited by $D_2$ upon delithiation, we observe that the rates of Li propagation in the indirectly-contacted SiNWs are identical to those in the directly-contacted SiNWs. Here, we note that SiNW system $D_1'$-$D_2'$ lithiates faster and with less time-delay than SiNW system $D_1$ $D_2$. This difference in electrochemical behavior may be attributed to variable response of the $Li_2O$ electrolyte to the applied potential between separate experiments [71], [72]. We may also attribute the delayed contraction of $D_2$ to variant behavior of $Li_2O$, or alternatively, to different mechanical behavior of the larger nanowire ($D_1$, e.g. increased stress and cracking) as compared to the smaller nanowire ($D_2$). Despite these experimental variations, the curves of Figure 3.6 g provide evidence for identical rates of Li propagation in indirectly-contacted SiNWs to those in SiNWs directly contacting the Li source. Therefore, we conclude that there is no additional barrier to Li diffusion between physically-contacted SiNW surfaces at the charging rates used for these studies (approximately 2C).

### 3.3.3. Mechanical Strength of Weld at Silicon Nanowires Junction

We investigate the strength of the weld formed between two SiNWs using an experimental procedure shown in Figure 3.7.

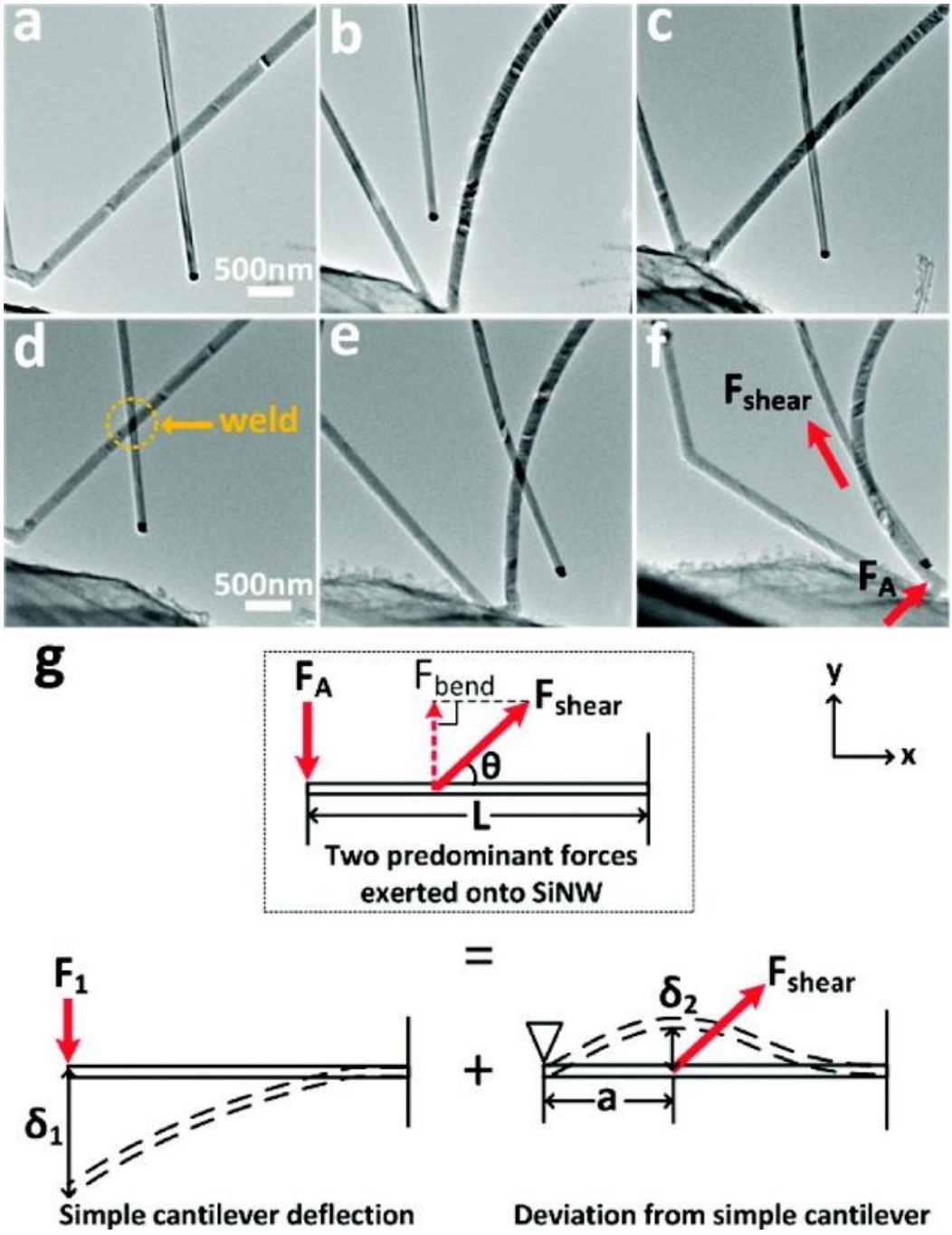


Figure 3.7. Determination of welding strength at the interface of crossed SiNWs after lithiation/delithiation. (a) As seen crossed nanowires. Same scale bar of 500 nm from (a–c). (b) Nanowires that are pulled apart to demonstrate they are grown independently. (c) Bend contours seen in both nanowires suggest they are in contact with each other. (d) Crossed nanowires after lithiation and delithiation. Same scale

bar of 500 nm from (d–f). (e,f) Stress applied on nanowires in order to separate them. (g) The free-body-diagram (top), which depicts the total deflection of the SiNW in (f), illustrates the two predominant forces that generate the total deflection of the nanowire; $F_A$ is the transverse force applied by nanomanipulator, and $F_{shear}$ is the shear force exerted by the weld. The total deflection is a linear superposition of two distinct deflections: $\delta_1$, generated by $F_1$ (a component of the unknown, total applied force $F_A$) and $\delta_2$, generated by $F_{shear}$. To calculate $F_1$, we model the system as a simple cantilever. To calculate $F_{shear}$, we model the system as a beam fixed at one end and pinned at the tip. $F_{bend}$ is the transverse component of $F_{shear}$, $a$ is the distance from the free end of the NW to $F_{shear}$, and $L$ is the total length of the NW.

Figure 3.7a shows two pristine crystalline SiNWs, which appear to cross each other as viewed through the TEM. We note that the nanowire closest to the lithium source exhibits kinking, which is believed to be due to twinning along the growth direction. This is commonly observed among bottom-up grown SiNWs (approximately 40% of the total SiNWs) [73], [74], but has no contribution or observed effect on the lithiation processes in this study. In order to confirm that the crossed nanowires are not the branches of the same parent nanowire, but instead, physically distinct nanostructures, we separated one of the nanowires from the other using the nanomanipulator (Figure 3.7b). Because they are easily separated from one another, both nanowires are observed to be separate entities rather than a single, branched or defective nanostructure. Next, the nanowires are brought back into physical contact with each other using the piezo-controlled STM probe. Single-crystal nanowires that

are bent exhibit a strong diffraction contrast in the form of Bragg-condition bend contours. These bend contours appear to move along the length of the nanowire as it is being strained [42]. The observed motion of the bend contours in both SiNWs unambiguously confirms that they contact one another (Figure 3.7c). Next, the SiNWs are lithiated and delithiated (Figure 3.7d) using similar parameters to those used for the experiment shown in Figure 3.6.

We perform two tests to determine if strong bonds are formed between two SiNWs after a single lithiation/delithiation cycle. First, we attempt to bring two SiNWs into and out of contact by applying positive and negative forces, normal to the plane of the SiNW junction. Prior to lithiation, the negative normal force overcomes any Van der Waals bonding that occurs when the two nanowires touch. After lithiation and delithiation, application of a negative normal force no longer separates the nanowires, suggesting the presence of a strong bond. Our second test, as demonstrated in Figure 3.7 d-f and described in detail as follows, allows us to assign a value to the mechanical strength of the weld. Although the strength of the weld cannot be precisely determined using our experimental data, we can estimate a lower limit to its mechanical strength by the observation that it was able to withstand the loading depicted in Figure 3.7f, just prior to failure of the weld. To estimate this lower bound, we modeled the primary SiNW as a suspended cantilever, as shown in the free-body diagram of Figure 3.7g. This SiNW is fixed at one end, at the silicon growth substrate, and is fully suspended in vacuum at all other points along its axis. The deformed shape of this SiNW, as shown in Figure 3.7f, results from two concentrated forces, a transverse force at its free end exerted by the moving Li source

($F_A$ in Figure 3.7f), and a shear force from the weld with the secondary SiNW ($F_{shear}$ in Figure 3.7f). The combined effect of these two forces on the deformation of the suspended SiNW is equivalent to the superposition of two decoupled configurations as illustrated in Figure 3.7g. In one configuration, the suspended SiNW is subject to a transverse force (labeled as $F_1$) at its free end. In another configuration, the displacement of the free end of the SiNW is fixed by a pin and the SiNW is subject to the concentrated force $F_{shear}$. The resulting deflection of the SiNW in these two configurations can be solved analytically, from which $F_{shear}$ and the shear strength can be estimated (see Appendix A). From this analysis, we estimate the shear strength to be at least 200 MPa. Thus, our analytical model suggests that the strength of the fused Si region is comparable to that of stainless steel (205 MPa) [75] and ceramic silicon carbide (~200 MPa) [76], thus demonstrating that a strong bond has been formed by the electrochemical cycling. To further verify the calculated strength, we also perform three-dimensional nonlinear finite-element analysis (FEA), as described in Appendix B. This analysis addresses any nonlinear effects arising from large deformations as depicted in Figure 3.7 e & f, and it leads to an estimated shear stress at the welded region of about 308 MPa, confirming the robust strength of the weld. Similar mechanical studies were carried out on a total of five separate nanowire junctions with qualitatively similar results, confirming that the strong bonding is a reproducible feature.

The observation of strong bonding in the welded region and facile lithium transport through the SiNW interface during lithiation and delithiation can be explained as follows. Generally, as Li intercalates into the SiNW, the energy barrier for breaking

the strongly covalent Si-Si bonds is significantly reduced. Initially, the Si-Si bonding energy is very high (2.72 eV), but according to a model put forth by Zhao *et al*. [77], when a single Si-Si bond is surrounded by four Li atoms, the energy barrier for breaking the bond is reduced to a mere 0.08 eV. Consequently, Si-Si bonds readily break—as they also tend to stretch—during Li intercalation. As Si-Si bonds are broken, the dangling bonds are saturated by neighboring Li atoms in order to lower the system's free energy. This model may be extended to our specific study of Li-assisted welding at the interface of two SiNWs. We observe that Li-Si bond formation occurs first at the high-energy nanowire surface before the lithiation reaction propagates inward toward the nanowire core. When the surfaces of two nanowires are directly in contact, Li atoms can bond simultaneously with the surface atoms on both the primary and secondary nanowires. Our results indicate that there is no additional energy barrier to diffusing to the surface of the second nanowire along this interfacial contact and reacting with this secondary surface as well. As a result, during intercalation, the surface energy of the crossed-SiNW system is reduced by forming metastable Li-Si bonds, which bridge the two nanowires at the interface. However, during Li extraction this Si-Li-Si bridge is broken and there is a kinetic driving force for neighboring Si atoms at the interface to bond to one another. Thus, the decrease of surface energy is the kinetic driving force for welding SiNWs. Moreover, the reconstructing of surface Si-Si bonds by Li transport across connected SiNWs makes the welding phenomenon possible at room temperature. Finally, we note that the SiNWs used in our experiments were all encompassed by a ~2nm layer of native $SiO_x$, but, this $SiO_x$ layer apparently does not complicate the Si-Si bonding

process. One possible explanation for this is that the $SiO_x$ may be reduced into Si, $Li_2O$ and Li-containing silicates upon $Li^+$ insertion, of which the latter two may also be serving to enhance the strength of the welded junction [78]–[80]. A second possibility is that the volume expansion of the SiNW during lithium insertion may also break the $SiO_x$ layer, thereby enabling direct contact between the interfacial host atoms [66], [67], [81]. This explains the Li-Si bonding and corresponding phase changes at the interface of the crossed SiNW system.

### 3.3.4. Summary

To summarize, we have directly observed electrochemical welding of cross-contacted SiNWs at ambient temperatures during lithiation and delithiation by *in situ* TEM studies. By comparing the incremental expansion and contraction of the SiNWs that are in direct contact with the Li source to those that are not, we have demonstrated that there is facile Li transport between two SiNW interfaces. We also estimate the minimum mechanical shear strength of the interfacial weld between two SiNWs to be ~200 MPa, indicating that this welding process generates strong interfacial bonds. The inherently high capacity of silicon, combined with facile Li diffusion between surface-contacted Si nanostructures, may enable the self-assembly of an interconnected network for Si nanowires in anodes, leading to high energy density lithium ion batteries with improved cycling stability. We suggest that this welding phenomenon may also serve as a self-healing mechanism in Li-ion battery electrodes. It is well-known that during cycling SiNWs may lose electrical contact with the electrode support, but our experimental results indicate that such detached nanowires may still actively participate in Li storage if they remain part of a robust contacted

network, formed during the first lithiation cycle [82]. Furthermore, the welding and self-healing processes that we have observed in SiNWs may equally apply to other alloy-based anode materials, such as germanium and tin.

3.4. Acknowledgement

Designed and conceived by me, Xiao Hua Liao, Jian Yu Huang and Prof. John Cumings All *in-situ* TEM cycling of SiNWs were performed by me. Some data on anisotropic expansion behavior of SiNWs were taken by Sandia group (Xiao Hua Liu, Yang Liu, John P. Sullivan and Jian Yu Huang) and analyzed by UoP (He Zhong, Li Qiang Zhang, Jiang Wei Wang, and Scott X. Mao), GIT (Shan Huang, and Ting Zhu), and UPenn (Akihiro Kushima, and Ju Li). Sample prepared by LANL group (Jeong-Hyun Cho, S. Tom Picraux, and Shadi A. Dayeh). Welding strength analysis done in help from Eric Epstein. Teng Li and Zheng Jia performed Finite Element Analysis (FEA). John Cumings and Chunsheng Wang co-advised the project.

# Chapter 4: Silicon @ Carbon Nanotube Heterostructures

## 4.1. Interface Mechanics of Carbon Nanotube@ Amorphous Si (CNT@ α-Si) Co-Axial Nanostructures

*Adapted from Ref.* [83]

### 4.1.1. Introduction

Silicon offers the highest theoretical capacity for lithium storage. However, it suffers from massive pulverization and cracks when subjected to electrochemical lithiation and delithiation. Additionally, the low electrical conductivity of silicon due to its semiconductor nature reduces lithium diffusivity and charge/discharge rate during electrochemical cycling. CNTs, because of their outstanding electrical properties apart from their high chemical stability, high aspect ratio, strong mechanical strength, electrical conductivity, and high activated surface area, are attractive electrode materials in energy storage devices, such as electrochemical capacitors, fuel cells, and lithium batteries [84]–[86]. Heterogeneous structures of amorphous silicon coated CNTs (CNT@ $\alpha$ -Si) separate lithium ion storage and electron transport pathways. The $\alpha$-Si layer acts as the lithium-ion storage medium, while the CNT core provides a mechanical support for $\alpha$-Si and a continuous electron transport pathway. Thus, this core/shell structure may combine advantages of both CNTs and nanostructured $\alpha$-silicon, while eliminating the weakness for each other. Experiments using silicon-coated carbon fibers have shown early promise of this strategy for improving the performance of lithium ion batteries [48].

The mechanical reliability at the interface of a heterogeneous structure is critical to the use of this type of materials in applications such as composites and energy storages. Atomic force microscopy (AFM) is often used to characterize the mechanical properties of nanostructures. When a CNT is deflected using the tip of an AFM, its displacement is directly related to the force acting on the tip, thereby giving a measurement of the Young's modulus [87]. Based on electric-field-induced resonant excitation, an alternative technique has been developed for measuring the mechanical properties of individual nanowire-like structures by *in-situ* transmission electron microscopy (TEM) [88], [89]. Here we report a synthetic approach for fabricating individual, cantilevered CNT@ $\alpha$-Si coaxial nanostructures and investigate their mechanical properties by combining a static bending test and *in-situ* TEM imaging. The interfacial mechanical properties were correlated with the heterogeneous structures simultaneously resolved through electron imaging.

### 4.1.2. Synthesis

Well-crystallized arc-discharge multiwall carbon nanotubes (MWCNTs), with few surface defects and a diameter range of 2-50 nm, are covalently functionalized with $-(CH_2)_5COOH$ groups using a modified Billups-Birch reaction [90]. The functionalized CNTs are drop-casted onto a clean Si (100) thin-wafer substrate (250 μm). The Si substrate is cleaved, leaving a controllable number of cantilevered f-CNTs protruding over the edge of the cleaved Si substrate. Similarly, MWCNTs without functionalization are chosen as control samples. Amorphous Si is deposited onto f-CNTs and CNTs at 460 ˚C using a low pressure chemical vapor deposition (LPCVD) method with 2 Torr of silane as the silicon source and 1 Torr of argon as

the protective gas. The thickness of amorphous Si shell is controlled by deposition time.

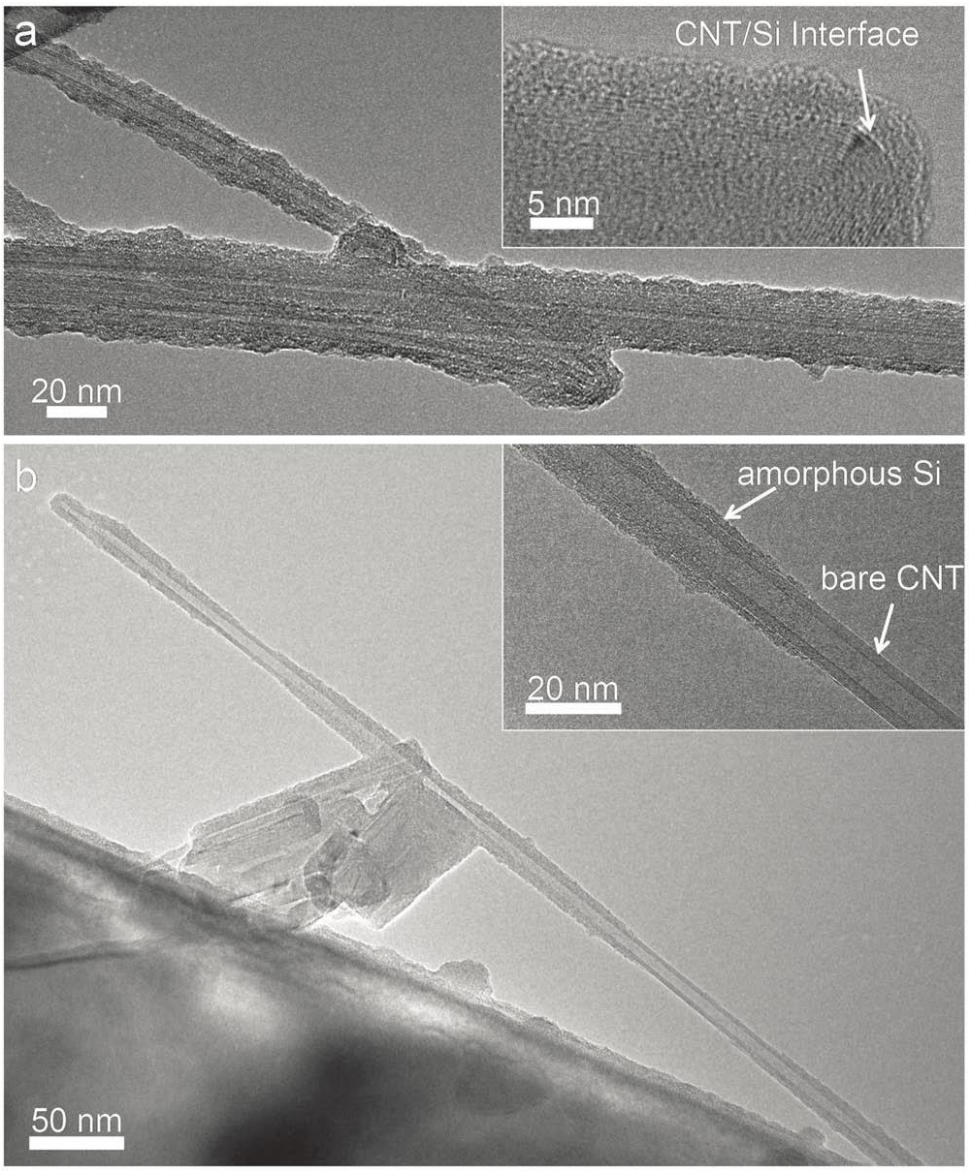


Figure 4.1. TEM images of thin $\alpha$-Si coated CNTs showing a strong dependence on surface functionalization. The CNTs were a) functionalized with alkylcarboxylic groups and b) further annealed at 600 °C in $Ar/H_2$ for 1 h to remove the functional groups. Insets show the high-resolution TEM images.

4.1.3. TEM Bending Test

The foremost objective is to understand the mechanical reliability at the interface of a heterogeneous structure. The intactness at the interface is a critical factor for its long term stability and better cycle performances as a battery electrode. So, a bending test is performed to test the mechanical toughness of the CNT@ $\alpha$-Si structure as shown in Figure 4.2.

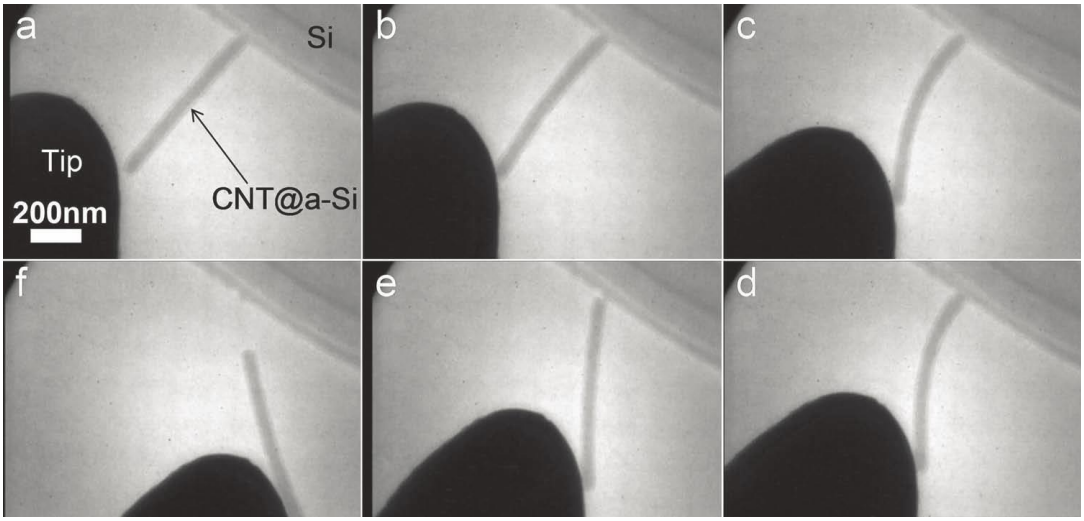


Figure 4.2: Snapshots of a bending test on a coaxial nanostructure with a 12 nm CNT core and a 24 nm amorphous Si shell: a) before the test, b,c) a lateral force is applied, d) immediately before the shell breaks, e) after the Si shell is broken, and f) when the shell is partially pulled out.

After CNTs are coated with amorphous Si, the sample is mounted onto a Nanofactory manipulation holder and loaded into the TEM chamber. A Pt/Ir tip approaches the CNT@$\alpha$-Si core/shell structure applying a lateral force to the free end of the coaxial structure, and the process is captured with digital video. Figure 4.2 shows snapshot images extracted from a movie. Figure 4.2a shows a nanostructure with diameter 60

nm (CNT diameter 12 nm and $\alpha$-Si thickness 24 nm), prior to making contact with the Pt/Ir tip. From Figure 4.2b–d, the applied force increases, and the coaxial structure bends with increasing curvature. Figure 4.2d is the snapshot just prior to the failure of the $\alpha$-Si layer, where the heterogeneous structure exhibits elastic deformation. With increasing force, the amorphous Si shell breaks at the root while the CNT core survives intact. The core/shell structures routinely fail via sudden brittle fracture of the shell at the vicinity point where the nanostructures are anchored to the silicon substrate. During the bending process, no plastic deformation is observed. Previous results on single-crystal GaN nanowires showed dislocation nucleation and propagation before fracture [91]. However, with the CNT@$\alpha$-Si coaxial nanostructures, no such preliminary processes are observed, indicating that the CNTs are mechanically stronger than $\alpha$-Si. The Young's modulus of amorphous Si (bulk) is approximately 80 ± 20 GPa [92], while those of MWNT outer layers range from ≈270 to ≈950 GPa [93], which is about 10 times stiffer than amorphous Si. Furthermore, the bending stress is a maximum at the outer edges of a beam section and it is zero at the neutral axis. Thus, the amorphous Si shell carries more stress than the CNT core. For a cantilever beam with a concentrated force applied at the free end of the beam, the anchor point suffers the maximum bending moment. This explains why the coaxial nanostructures break at the anchor point.

Interestingly, at excessive force, the broken $\alpha$-Si shell is released from the coaxial structure. Using the Pt/Ir tip, the Si shell can be slowly pulled out like pulling the sheath from a sword and leaving the CNT core (Figure 4.2f). The broken $\alpha$-Si shell can be partially or completely pulled out.

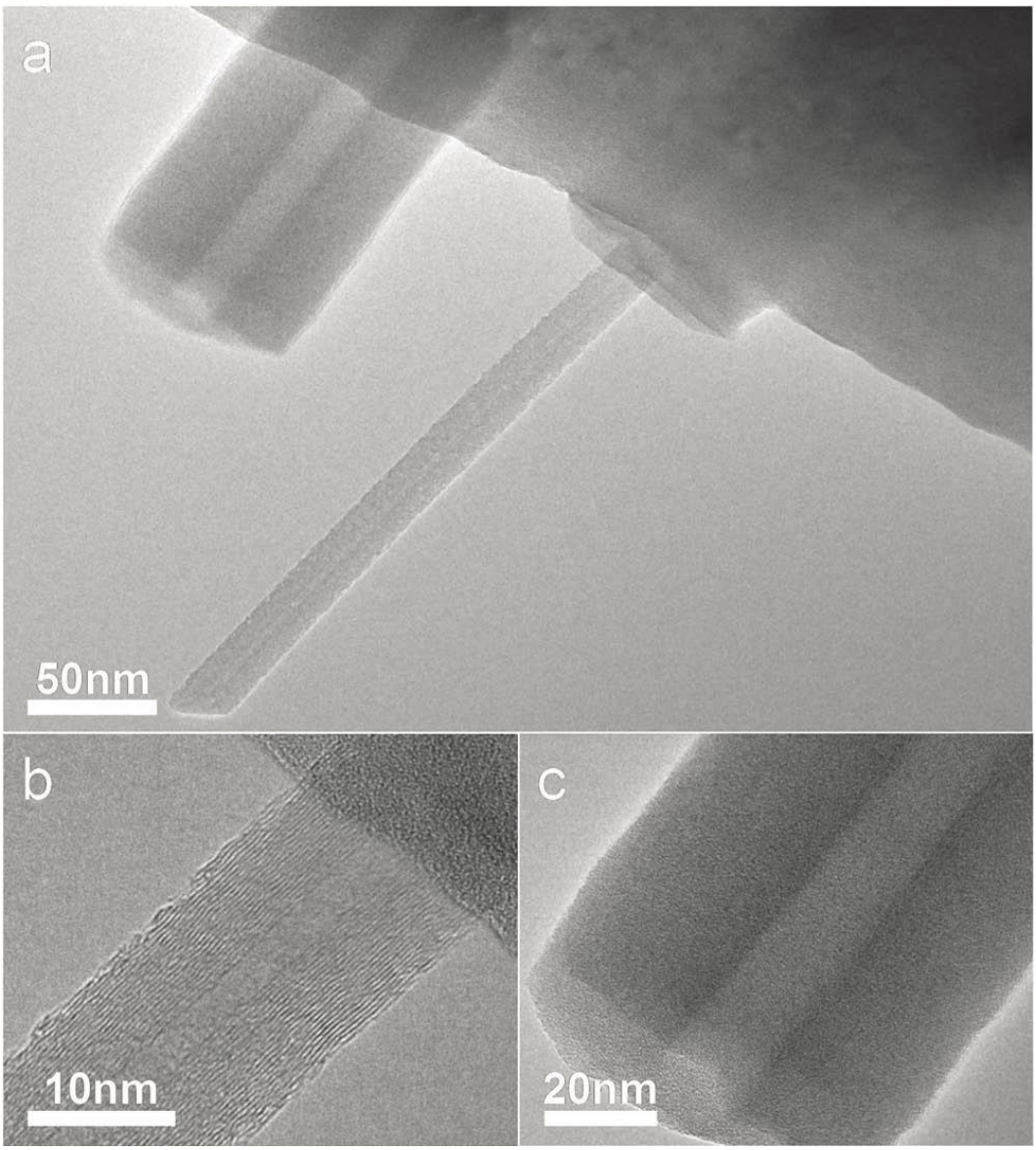


Figure 4.3: TEM images of a) a broken CNT@$\alpha$-Si structure with the Si shell placed side-by-side to the CNT core and high-magnification images showing b) the CNT and c) $\alpha$-Si at the broken interface.

After a crack initiates in the $\alpha$-Si shell, stress concentration at the crack tip creates an excessive shear force between the shell and the CNT core due to the differential mechanical stiffness. Clearly, this stress concentration is strong enough to overcome

the interactions between the $\alpha$-Si shell and the CNT core such that the broken $\alpha$-shell can be readily pulled out by the Pt/Ir tip, which presumably interacts with the amorphous Si shell by van der Waals interactions. The shell remains intact after removing from the tube and it does not break into pieces. Figure 4.3a shows a TEM image of an $\alpha$-Si shell completely pulled out and subsequently placed on the edge of the Si substrate side by side with the corresponding CNT core. High-resolution TEM images (Figure 4.3 b,c) clearly show that the $\alpha$-Si shell does not contain any graphite layers from the CNT and no $\alpha$-Si is left on the CNT. We note a modest roughening of the carbon nanotube surface (Figure 4.3b). Two possible sources can cause such roughness, and the first is chemical functionalization. Although our chemical functionalization does not remove carbon atoms from the nanotube surface, it introduces alkylcarboxylic groups that are covalently attached to the nanotube sidewall. Since the carboxylic groups can form strong Si–O bonds, partial fracture of the outermost layers of the nanotube might have occurred during the process of breaking or pulling out the $\alpha$-Si. The second possible source of CNT roughening is plasma etching during the Si deposition process. The plasma during PECVD process is energetic enough to knock out some carbon atoms from the outer layer of a CNT. In a control experiment, we intentionally damaged the outer layers of a MWNT by plasma treatment prior to PECVD. We observed that the damaged graphitic layers were pulled out along with the $\alpha$-Si shell. This indicates that the interaction between the $\alpha$-Si shell and the damaged graphitic layers of a MWNT can be stronger than the van der Waals interactions between two pristine graphitic layers in a MWNT and the interfacial mechanics can be tuned by the surface chemistry.

### 4.1.4. Summary

In conclusion, we report a synthetic approach for fabricating cantilevered CNT@ $\alpha$-Si coaxial nanostructures and in situ TEM bending studies of their mechanical properties. Both the growth of the conformal Si coating and the mechanical properties of these heterogeneous nanostructures show a strong dependence on the CNT surface chemistry. The $\alpha$-Si shell breaks at the anchoring point to the Si substrate under an increasingly applied force on the free end of the cantilever-like structure. The broken $\alpha$-Si shell can be removed like pulling the sheath from a sword while the CNT core survives intact, illustrating a striking difference in mechanical properties between $\alpha$-Si and CNTs and the relatively weak interfacial bonding between the two materials. The interfacial bonding is improved by surface functionalization of the CNTs.

## 4.2. Lithiation/Delithiation Studies on Uniform-and Bead-Silicon on CNT

*Adapted from Ref.* [94]

### 4.2.1. Introduction

Silicon  nanomaterials have been intensively studied as a potential anode material for high capacity lithium ion batteries [30], [61], [95]–[100] . Nanostructured materials shorten electronic and ionic transport paths and enable strain relaxation to prevent Si fracture-induced capability loss. In a one-dimensional silicon nanowire, the mechanical stress that arises during lithiation/delithiation cycles can be effectively relaxed along the radial directions. This reduced-dimension benefit could potentially be maximized in quasi zero-dimensional nanoparticles, where stress relaxation can occur in all three dimensions. *In-situ* TEM studies of the detailed lithiation processes of single Si particles provide direct evidence that silicon nanoparticles below a critical size are indeed immune from cracking [101].

However, retaining electrical connectivity for silicon nanoparticles in an electrochemically demanding environment remains an even greater challenge to electrode design. Even if nanoparticles do not crack, they easily detach from the current collector or other conducting phases, resulting in undesirable capacity loss [53], [102]. To maintain electrical connectivity in Si electrodes, there is substantial interest in incorporating low dimensional carbon nanomaterials such as CNTs and graphene in the design and synthesis of heterostructured Si anodes [83], [103], [104] because such nanostructures provide complementary properties including excellent

electrical conductivity and mechanical durability. However, the native adhesion between Si and $sp^2$ carbon layers has proven to be inherently weak [104], [105], and interfacial delamination remains as a significant challenge in these nanocomposite materials. With the potential to alleviate this problem, it has already been shown that binders containing carboxyl groups can enhance stability, thus reducing irreversible capacity losses [106]–[109]. The improved stability has been attributed to strong interactions between a hydroxylated Si surface and the carboxyl groups of the binder [110].

Here, we demonstrate the synthesis of electrically connected silicon beads on covalently functionalized CNT (*f*-CNT) strings. Carboxylic functional groups are covalently attached to the $sp^2$ carbon lattice in a unique "banding" fashion, allowing growth of discrete amorphous silicon beads symmetrically threaded along the CNT at regular intervals and with strong interfacial bonding. This beaded-string structure affords advantageous features unattainable in a conventional continuous coaxial morphology, where Si is uniformly coated on CNTs over the entire surface. Both theoretical modeling and comparative *in-situ* TEM studies reveal remarkably improved structural durability of this novel beaded-string structure during lithiation and delithiation.

### 4.2.2. Synthesis

Arc-discharge multiwall carbon nanotubes are chosen for this study because their high crystallinity and low defect-density are ideal for synthesis of well-defined model heterostructures. Functional bands of $–(CH_2)_5COOH$ groups are covalently attached to the outermost walls through C-C bonds using a propagation chemistry developed

previously by some of us [90]. Unlike oxidative chemistries, this propagation chemistry does not remove carbon atoms from the $sp^2$ lattice of a CNT. Each functional group is instead amplified into a band consisting of hundreds of $–(CH_2)_5COOH$ groups. Amorphous Si ($\alpha$-Si) is grown on both the *f*-CNTs and on pristine CNTs at 460 $^oC$ by low pressure chemical vapor deposition (LPCVD) using silane as the silicon source.

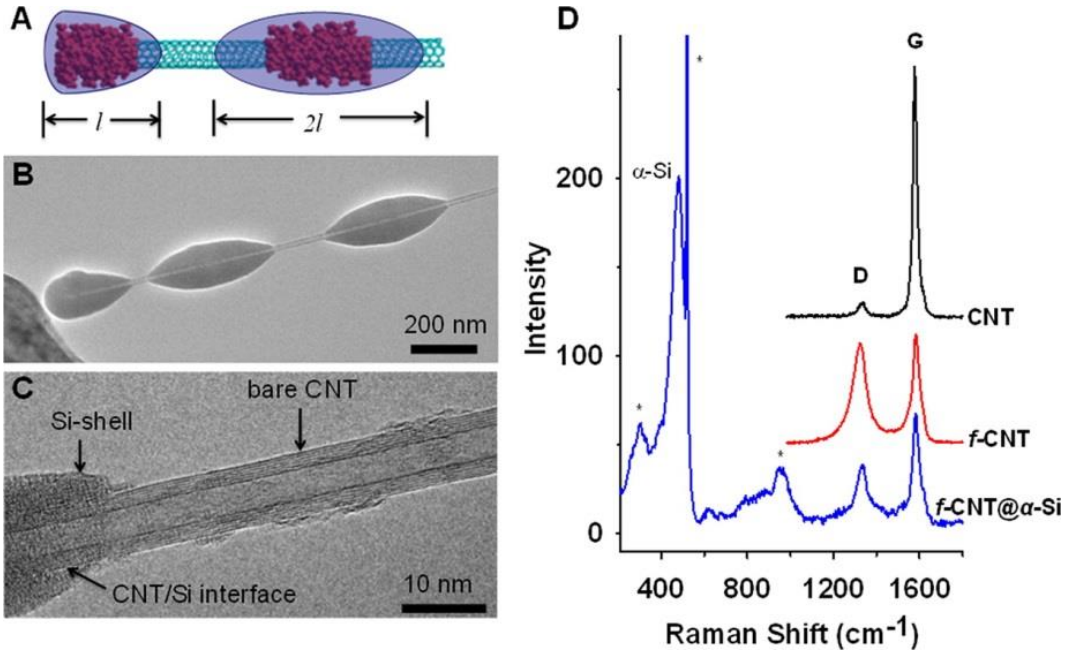


Figure 4.4: Functional bands control α-Si nucleation on f-CNTs. (A) Schematic and (B) TEM images showing symmetrical relation of $\alpha$-Si beads on the end and sidewall of a *f*-CNT. (C) HRTEM images show the bare CNT between two Si beads and the interface of CNT-core/$\alpha$-Si-shell. (D) Raman spectra of *f*-CNT@ $\alpha$-Si beaded-string structures in comparison with the pristine CNTs and alkylcarboxylated CNTs. The peaks marked by "*" arise from the crystalline silicon substrate. The excitation line was 632.8 nm.

We found that the surface chemistry of CNTs plays a vital role in controlling the growth of $\alpha$-Si on the CNTs. For *f*-CNTs, the functional bands serve as nucleation centers, from which the growth of $\alpha$-Si starts and extends axially away in both directions, leading to a beaded-string structure with discrete ellipsoidal $\alpha$-Si beads threaded on the nanotube (Figure 4.4).

The lengths of the beads follow a distribution similar to functional bands previously observed with single-walled CNTs [90], suggesting $-(CH_2)_5COOH$ or defect-dictated silicon nucleation. All $\alpha$-Si beads have similar axial length, except those at the end of CNTs, which typically exhibit half of the length of other beads (Figure 4.4 A & B). This difference can be explained by assuming that Si can grow in only one direction at the end of a CNT but in both directions from functional bands on the CNT sidewall. As growth proceeds, the adjacent ends of the Si ellipsoids may overlap and ultimately form a continuous core-shell structure, depending on the growth time. All the Si beads in an *f*-CNT@$\alpha$-Si structure have a similar shape and diameter. High resolution transmission electron microscopy (HRTEM) images (Figure 4.4 C) clearly show that the *f*-CNT string and Si beads meet at a well-defined *f*-CNT/Si interface, with the segment between two adjacent Si beads being a bare CNT with little Si coating. SEM and TEM images collected at different rotation angles confirm that Si grows with nearly perfect rotational symmetry along the nanotube, demonstrated the controlled morphology of the synthesis. Raman spectra of the *f*-CNT@$\alpha$-Si beaded-string structures confirm the characteristic G and G′ peaks of CNT at 1580 $cm^{-1}$ and 2660 $cm^{-1}$, respectively, as well as the peak of amorphous Si around 480 $cm^{-1}$ (Figure 4.4 D). The peaks around 300, 520 and 940 $cm^{-1}$ are assigned to crystalline silicon

within the supporting substrate. Covalent attachment of alkylcarboxylic functional groups to the nanotube sidewall introduces $sp^3$ defect centers, which activate the disorder mode around 1325 $cm^{-1}$. This disorder peak persists in the *f*-CNT@*α*-Si structures, suggesting a CNT surface chemistry-dictated CNT/Si interface. In contrast, for pristine, unfunctionalized CNTs, a uniform, continuous *α*-Si coating is typically formed (Figure 4.5, A & B). This is attributed to uniform nucleation on the nearly defect-free and atomically smooth surface of a pristine CNT.

### 4.2.3. Kinetics and Microstructural Evolution

To follow the structural evolution of these heterostructured electrodes, a prototype nanoscale electrochemical cell is built inside the TEM using lithium metal as a counterelectrode and its native surface $Li_2O$ layer as an electrolyte. As the $Li_2O$ electrolyte is brought into contact with the *f*-CNT@*α*-Si heterostructure using an *in-situ* nanomanipulator, a constant bias with respect to Li metal is applied to the nanowire. Unless otherwise specified, the bias used in these studies is -2 V, which is sufficient to reproducibly induce super-ionic transport within the $Li_2O$ layer , providing a pathway for $Li^+$ to diffuse into the contacted *f*-CNT@ *α*-Si structure. Upon application of the electrochemical bias, lithium rapidly propagates axially towards the opposite end of the structure.

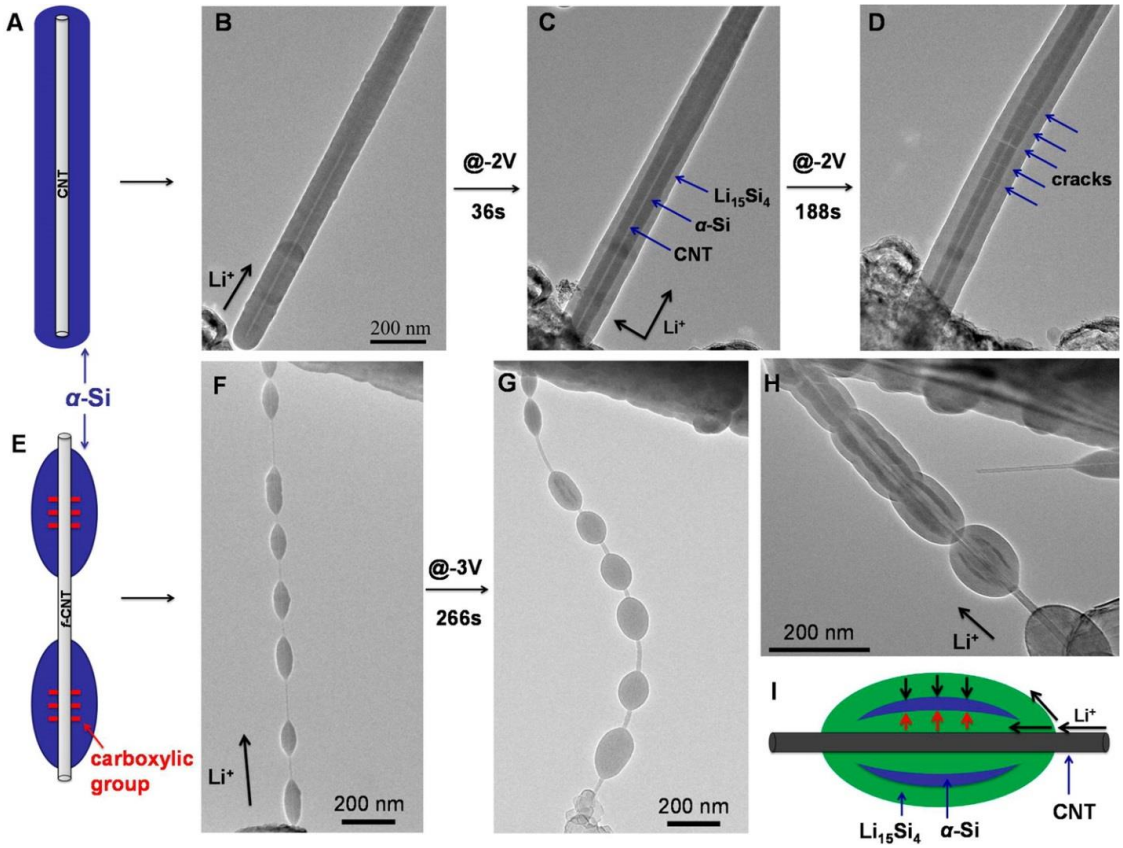


Figure 4.5: Microstructural evolution of beaded-string heterostructures upon lithiation propagation. (A, E) Schematic drawings show two different nucleation models with the free sliding and fixed interfaces. (B-D) Microstructural evolution of CNT@*α*-Si core-shell structure upon lithiation. (F,G) Microstructural evolution of *f*-CNT@ *α*-Si beaded-string structure upon lithiation. (H) Microstructural evolution of *f*-CNT@ *α*-Si upon lithiation (0V, t = 15s) shows that $Li^+$ propagated in two pathways: along both the *α*-Si surface and CNT/Si interface in the radial direction. (I) Schematic drawing indicates two reaction fronts for the formation of $Li_{15}Si_4$ in *f*-CNT@ *α*-Si beaded-string structure.

Figure 4.5 compares the morphology evolution of the beaded-string structure with that of the continuous core-shell structure. As is also clearly visible in Figure 4.5 A-D, lithium quickly diffuses along the surface of the *α*-Si in the axial direction,

followed by a lithiation reaction front propagating from the outer surface of $\alpha$-Si radially inward toward the CNT at the center. As a result, a tapered lithiation front is formed in the $\alpha$-Si during the lithiation process. By tracking the position of the lithiated/unlithiated Si interface, we estimate the interface propagation rate from *in-situ* TEM videography. The microstructural evolution of CNT@$\alpha$-Si continuous core-shell structures upon lithiation shows that $Li^+$ propagates along the axial direction at a high rate of 140±10 nm/s, in agreement with previous literature [104]. The reaction front propagating along the radial direction is much slower than the lithium diffusion rate along the axial direction. For the continuous core-shell structures, two stages of $Li^+$ propagation along the radial direction were observed: in one case, an average rate of 0.9 nm/s is exhibited in the first 36 seconds but drops to merely 0.24 nm/s after 188 s. In contrast, the beaded-string structure has a markedly different morphology change upon lithiation. Figure 4.5 F shows a series of beads along a *f*-CNT. From top to bottom, one can find non-lithiated (the first two beads), partially lithiated (3rd bead), and fully lithiated beads (the 4th and below) in Figure 4.5 G. Notably, the beaded-string exhibits remarkable flexibility in accommodating the volume expansion during lithiation. Besides the surface reaction, radially inward from the outer surface of each bead, there is also a second lithiation front propagating outwards from the CNT/Si interface toward the outer surface (Figure 4.5 H & I). This new reaction pathway is not observed with the core-shell structures grown on relatively defect-free CNTs. The two radial reaction front propagating rates, inwards and outwards, are ~1.7 nm/s and ~1 nm/s, respectively. Both propagation rates are faster than the radial propagation rates in the core-shell structure. This fast, interfacial propagation

pathway can be attributed to the finite length of the beads and the fast diffusion of $Li^+$ on both Si and CNT surfaces. This results in the beaded-string structure reaching full lithiation faster than the core-shell structure, leading to improved rate capability.

The different two-front lithiation morphology described above leads to distinct deformation and failure behaviors of the Si phase in these two nanostructured electrodes. As evident in Figure 4.5 D, upon further lithiation of the continuous core-shell heterostructure, the unlithiated portion of the $\alpha$-Si shell tends to crack across axial direction. Even by slow and gentle lithiation of comparable structures at a minimum bias (0 V) with respect to lithium metal, the $\alpha$-Si shell failed to avert the formation of these cracks. Such fragmentation of the unlithiated Si shell can severely degrade the cycle stability of CNT@$\alpha$-Si electrodes. By contrast, all *f*-CNT@$\alpha$-Si beaded-string electrodes tested in our *in-situ* experiments sustained significant lithiation-induced deformation without appreciable fracture, suggesting a highly robust non-cracking nanostructure design of anodes for lithium ion batteries.

### 4.2.4. Stability and Radial Breathing Mode of Beaded-Silicon

To further evaluate the stability of beaded-string structures, we follow the lithiation and delithiation of these structures for many cycles with *in-situ* TEM (Figure 4.6). Constant biases of -0.1 V and +3 V with respect to lithium metal are applied to the beaded-string structures during lithiation and delithiation, respectively. The complete state of lithiation and delithiation is assessed by the observable morphological changes in the structures, which stabilize toward the lithiated and delithiated states. The numbered upper and lower labels, except 0 (pristine) in Figure 4.6a depict the number of lithiated and delithiated cycles respectively. The cross-sectional area of

individual beads is calculated by estimating the maximum transverse radial change during lithiation and delithiation.

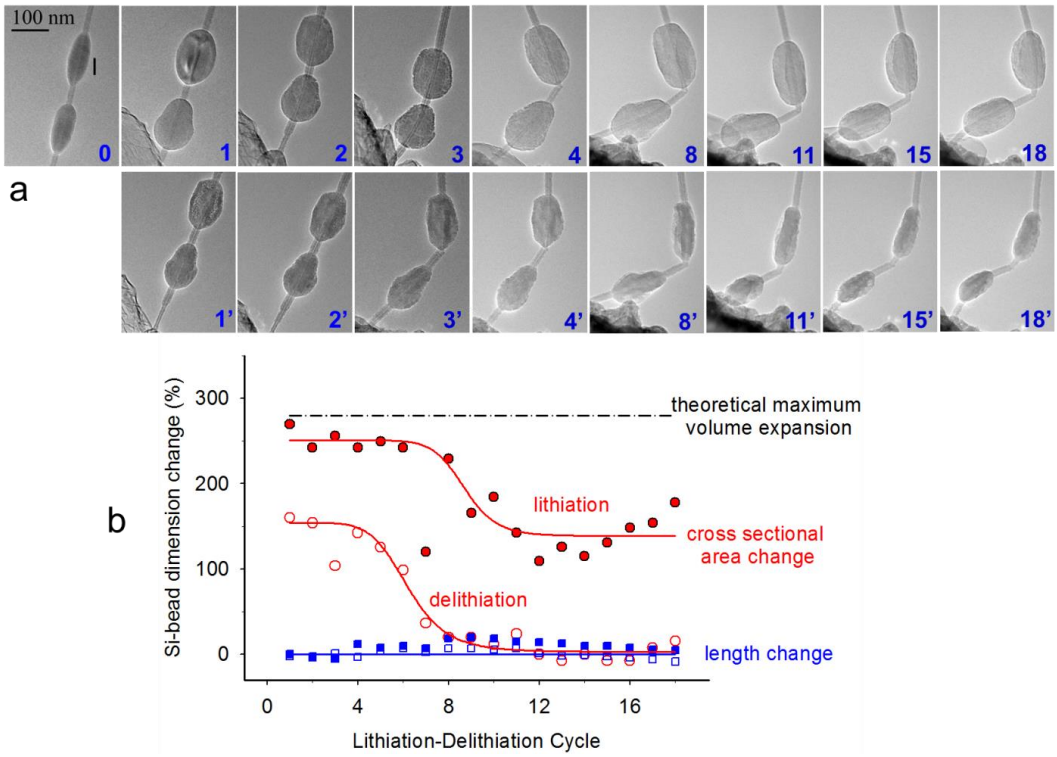


Figure 4.6: Radial breathing mode of Si beads during lithiation and deliathiation cycles. (a) Microstructural evolution of *f*-CNT@*α*-Si during 18 cycles of lithiation (at -0.1 V) and delithiation (at +3 V) (n-lithiation cycle, n'-delithiation cycle) (all the images have the same scale bar). (b) Plot of Si-bead dimensions, which change as a function of cycle, showing a "radial breathing mode" of Si beads during lithiation and delithiation cycles.

During the initial 8 cycles, the volume expansion of the lithiated beads nearly reached the theoretical limit. We note that the delithiated silicon did not recover its original size, probably due to the incomplete removal of Li during delithiation or the generation of pores and/or voids, as previously observed in Ge nanowires [63]. For cycles after the 8$^{th}$, the delithiated Si beads recover their original sizes, but the

lithiated state does not reach its theoretical capacity, probably due to internal resistance increase or Si structural change. However, analysis of the changes in diameter and length of Si beads over 18 cycles reveals a consistent and reliable "radial breathing mode" of expansion and contraction as $Li^+$ inserts and extracts from the silicon beads. The axial length of the beads barely changes over all cycles, while the main volume expansion is reflected only in the changing radius of the beads. This radial breathing mode further suggests highly reversible mechanical durability of the beaded-string structures.

One major concern with nanoparticle-based electrode materials is their low volumetric storage capacity due to the large inaccessible inter-particle space. We found that with beaded-string structures, the silicon beads can be grown during synthesis to the point where adjacent beads just begin to touch and even merge slightly. Since the Si beads do not elongate axially upon lithiation, the spacing between beads can be designed to be very small. An example is shown in Figure 4.7 where Si beads with diameters approaching 200 nm were grown on a CNT of merely ~20 nm in diameter.

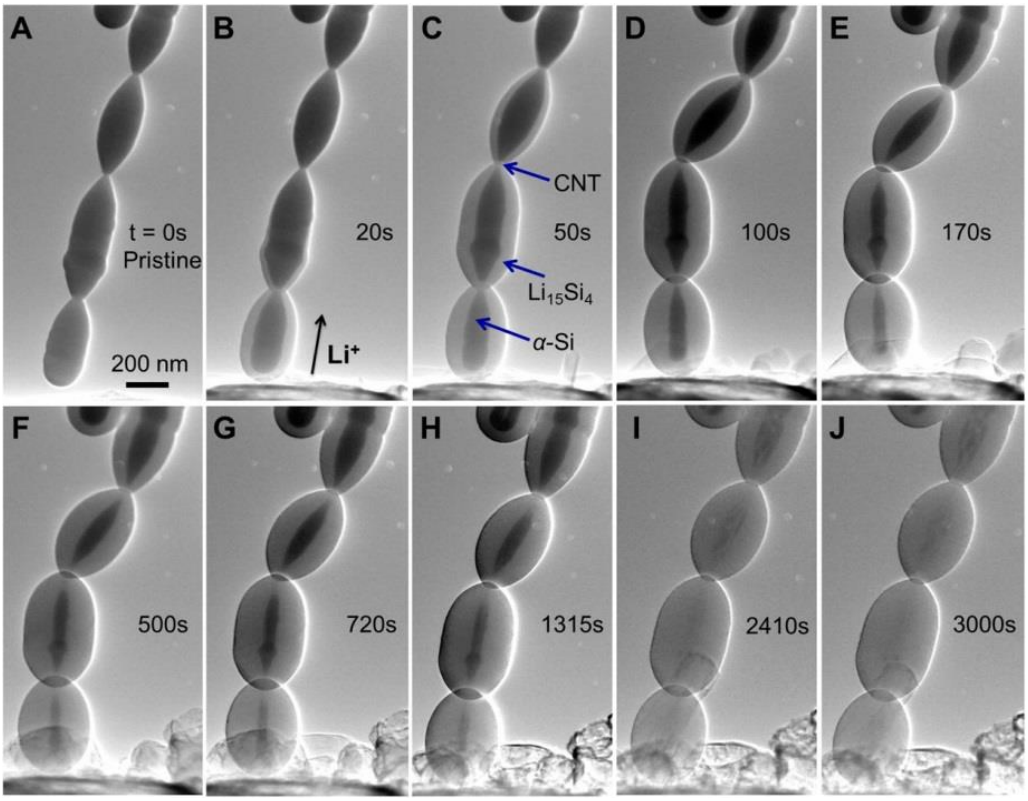


Figure 4.7: Microstructural evolution of *f*-CNT@*α*-Si beaded-string upon lithiation at -2V. The diameter of pristine bead is 198 nm. The diameter of bead in (J) is 352 nm. Note the purely radial expansion, which prevents the beads from coalescing, even though they are nearly touching at the beginning.

*In-situ* TEM studies confirm non-cracking behaviors in all such beaded-string structures investigated. Therefore, these beaded-strings can have a volumetric capacity comparable to that of silicon nanowires, but with better cycle life due to their enhanced mechanical durability. We note that in these larger beads, the second interfacial lithiation pathway is lost, probably because all the CNT surfaces are covered by silicon making it behave virtually like a core-shell structure with respect to lithium diffusion. However, the non-cracking behavior is again clearly evident.

### 4.2.5. Summary

In summary, *f*-CNT@ $\alpha$-Si beaded-string heterostructures with chemically tailored carbon-silicon interfaces were designed and synthesized based on a fundamental understanding of carbon surface chemistry and Si nucleation on covalently modified CNT surfaces. *In-situ* TEM studies of lithiation propagation reveal that these novel heterostructures can accommodate huge volume changes during lithiation and delithiation without appreciable mechanical failure. By contrast, CNT@$\alpha$-Si continuous core-shell nanostructures fracture upon lithiation. DFT and continuum FEM studies consistently suggest that the strong Si-C interface made possible by the carboxylic functional bands on CNTs plays key roles in enabling non-cracking *f*-CNT@$\alpha$-Si beaded-string heterostructures. These findings thus provide important new insights in the synthesis of high performance Si electrodes, laying a foundation for next-generation lithium ion batteries.

## 4.3. Acknowledgements

This work is performed in collaboration with Prof. YuHuang Wang group. The controlled synthesis of CNT@ $\alpha$-Si sample is performed by Prof. YuHuang Wang group (Hongwei Liao, ChuanFu Sun, and Yin Zhang), and we conduct *in-situ* TEM lithiation/delithiation experiments. Modeling and simulations done by Prof. Teng Li, Zheng Jia, and Yue Qi (GM). Prof. Gary Rubloff provided valuable insights in overall discussions.

# Chapter 5: Silicon Nanotubes

*Adapted from Ref.* [111]

## 5.1. Introduction

Advanced lithium-ion battery technology has permeated the portable electronics industry and also has potential for application to electric vehicles and stationary grid storage [112], [113]. Silicon is a promising candidate to replace current graphite anodes because it is an earth-abundant material with exceptional specific capacity of Li at room temperature (3579 mAh/g *vs.* 372mAh/g for graphite) [10], [61], [113]. However, silicon undergoes massive volume changes (~300 %) during charge and discharge cycles leading to stress-induced cracking and poor cycle life [114], [115]. To solve these problems and to move toward widespread industrial adoption of silicon-based lithium-ion batteries both require major improvements in three core areas: i) structural integrity of the electrode, ii) electronic and ionic transport pathways, and iii) stability of the electrode/electrolyte interface. Nanostructured forms of silicon, particularly 1D structures, have been shown to mitigate some of the underlying problems observed in bulk counterparts [23], [24], [26], [30]–[32], [116]. For instance, the pioneering work by Chan *et al*. demonstrated nearly theoretical charge capacity in silicon nanowire (SiNW) anodes grown directly on a current collector [30]. The reduction in size and large surface-to-volume ratio of 1D nanowires facilitate lithiation-induced strain relaxation, short lithium diffusion lengths, and efficient electrical conducting pathways for faster charge and discharge cycles.

Unfortunately, the nanostructuring of silicon creates additional challenges due to the large surface-to-volume ratio, which leads to a large surface area that can cause unwanted side-reactions with the liquid electrolyte. For example, the reduction of organic electrolytes during the charge transfer process can lead to the formation of a solid electrolyte interphase (SEI) layer that reduces lithium diffusivity and causes irreversible capacity loss [23]. On the contrary, a thin SEI layer that only grows during the initial few cycles can instead form a permanent protective layer preventing further growth, while allowing $Li^+$ ions to diffuse readily between the electrode and electrolyte. This variety of SEI is regarded as an ideal compromise for battery applications [23], [24]. However, the notorious volume changes experienced by silicon during electrochemical cycling can simultaneously weaken and tear the SEI layer causing the silicon to be directly re-exposed to the electrolyte with each cycle, thus re-forming a new SEI film. This repeated reduction and consumption of electrolyte during cycling can quickly thicken the SEI layer, consuming lithium from cathodes and impeding the further transfer of $Li^+$ ions across the interface. This instability in SEI formation can eventually lead to overall capacity loss and failure of the battery.

Two main strategies have been implemented to stabilize and control the parasitic thickening of the SEI layers on nanostructured silicon electrodes. First, the use of functional coatings such as carbon [31], [52], [117], copper [118], [119], nickel [120], [121], silver [122], and alumina [123] on the surface of silicon electrodes has shown some promising outcomes. These surface coatings can act as a buffer layer between the active electrode and electrolyte and prevent the formation of excess SEI layers.

Electronically active coatings also enhance the conducting pathways of the active Si and remove the need for extra additives [10]. Despite the advantages of such coatings, the precise role they play in constraining the volume changes in silicon during lithiation and delithiation is not fully understood. A second approach has focused instead on the internal structure of silicon nanomaterials, with the goal of providing stress relief through hollow nanostructures, with internal voids. Yao *et al*. compared the stress evolution during lithiation in a hollow nanosphere and a solid nanoparticle with the same volume of Si, and found that the solid form undergoes ~5 times more stress than the hollow counterpart [124]. Recent *in situ* transmission electron microscopy (TEM) studies on solid silicon nanostructures such as crystalline SiNWs [117] and amorphous Si nanorods [125] have demonstrated higher radial straining and simultaneous cracks in the structures when subjected to electrochemical lithiation and delithiation. Studies on corresponding hollow nanostructures, such as silicon nanotubes (SiNTs), have instead shown remarkable initial coulombic efficiencies of >85 % and stable capacity retention of >80 % up through 50 cycles [31], [32].These results all suggest that nanostructures with hollow or tubular shapes can provide substantial benefits over their solid counterparts.

Recently, one study combines the above two approaches, proposing the use of a 10 nm $SiO_x$ coating as a mechanical clamping layer on the outer surface of a SiNT electrode, to prevent the outward expansion that can damage the SEI, and, indeed, a coin cell using such a double-walled SiNT electrode showed excellent lithiation/delithiation cycle performance at a low Si mass-loading (less than 0.1 mg/cm$^2$) [99]. Inspired by this pioneering work, we seek to improve upon this

approach by moving toward higher capacity battery electrodes with significantly increased mass loading, by 30-100 times, as would be required for a broader range of battery applications. By following the fabrication procedure published previously (see Ref. 98 and Methods section below), we can obtain SiNTs with only a very thin $SiO_x$ coating—essentially uncoated nanotubes with only native oxide. When assembled into coin cells at the higher mass loading, these uncoated SiNTs show a rapid degradation of performance. To address this degradation, we additionally coat the outer surface of the SiNTs with nickel, which is both electronically conductive and inert to chemical interactions with lithium, like other metallic coatings [118]–[122], and unlike $SiO_x$. We found that conductive, electrochemically inert Ni coating on Si nanotubes can address the above three challenges simultaneously: structure integrity, fast ion and electron transport, and stable SEI formation for electrodes with a large mass loading. We find that cell capacity-retention and cycle-life are improved with increasing thickness of the Ni-coating layers, suggesting that the high strength of the nickel coatings is indeed able to carry the large hoop stress caused by the expansion of the SiNTs during lithiation. To test such a hypothesis, we conduct further *in-situ* TEM studies, and our observations confirm that, with the thicker Ni layers, the system exhibits a mode where the lithiation-induced expansion is in fact inward-directed entirely on the inner diameter and suppressed on the outer diameter.

## 5.2. Experimental Methods

Preparation of carbon fibers: The SiNTs samples were prepared by a template method using carbon nanofibers [99]. The carbon nanofibers were prepared by an electrospinning method followed by carbonization. During the process, 1.0 g of

polyacrylonitrile (PAN) (Sigma Aldrich) was added to 9.0 g of dimethyl formamide (DMF) (Sigma Aldrich) under mechanical stirring to form a viscous solution. The obtained viscous solution was transferred into a plastic syringe paired with a stainless steel needle (0.3 mm in diameter, *McMASTER-CARR*). The flow rate was kept at 6 µL/min. A grounded copper collector was used to collect the polymer fibers. A voltage of 15 kV was applied between the needle and the copper collector with the distance between them was kept at 15 cm. The as-collected polymer fibers were stabilized in air at a temperature of 280 °C for 5 h with a heating rate of 1 °C/min. The fibers were then pre-carbonized under argon atmosphere by heating to 500 °C with a heating rate of 10 °C/min and holding at this temperature for 0.5 h.

Silicon nanotubes**:** Amorphous silicon was deposited on the carbon nanofibers by a low pressure chemical vapor deposition (LPCVD). The deposition parameters used were: 2 Torr of $SiH_4$ as the silicon source, 1 Torr of argon as the protective gas and at a temperature of 460 ˚C. The thickness of the silicon deposition was controlled by the growth time. Typically, a coat of ~25-30 nm was applied to the carbon fibers in 20-30 minutes. After silicon was coated onto the carbon nanofibers, the sample was heated in air at 500 °C for 2 h with a heating rate of 5 °C/min to remove the carbon core and form a $SiO_x$ layer on the inner and outer surfaces of silicon nanotube. TEM-EDS line-scan analysis across the SiNT indicates that carbon has been completely removed during this oxidation process. During the thermal treatment, a $SiO_x$ layer with modest thickness is expected to grow on the inner and outer surfaces of the SiNT. We determine the thicknesses of $SiO_x$ layers to be ~4 nm by cross-sectional Energy-filtered TEM (EFTEM). We note that this thickness, while reproducible, is

significantly below the 10 nm reported in Ref. 98 for a similar procedure. The ~4 nm thickness is only modestly higher than a room-temperature-formed native oxide layer (~2-3 nm), and this result can be attributed to the low processing temperature (500 ˚C) and short oxidation time (2 h), consistent with other results on the oxidation of bulk silicon [126].

Ni coating: A conformal Ni layer was coated on the silicon nanotubes by conventional DC-magnetron sputtering in an argon atmosphere (1 Pa) using a DC power density of 4.5 W $cm^{-2}$. The target-to-substrate distance was kept at 11 cm, and a single layer of Ni was coated at different deposition times of 10, 30 and 100 min.

Electrochemical characterization: The free-standing uncoated SiNTs/Ni-coated SiNTs were directly used as electrodes for cell assembly without any binder and conductive additives. Coin cells, consisting of a uncoated SiNTs or Ni-coated SiNTs working electrode, a Li foil counter-electrode, Celgard 3501 microporous film separator, and 1.0 M $LiPF_6$ in ethylene carbonate (EC): diethyl carbonate (DEC) (1:1 by volume) liquid electrolyte, were used for electrochemical tests. The active electrode mass loadings for uncoated-SiNTs and Ni-coated SiNTs were 3.6 mg/$cm^2$ and 3.3 mg/$cm^2$, respectively. Galvanostatic charge-discharge tests were performed by using an *Arbin BT 200* test station. Both cells were cycled between 0.01 and 1 V *vs.* $Li/Li^+$ with a current density of 100 mA/g. The current density was calculated on the basis of the total weight of working electrode. After the cell reached the cut-off voltages, it was rested for 2 min before subsequent charge or discharge.

*In-situ* TEM testing and characterization***:*** ***In situ*** characterization was carried out using a JEOL JEM-2100 $LaB_6$ TEM operating at 200 kV. We use a specialized

Nanofactory STM-TEM holder which simultaneously allows imaging and manipulation with three degrees of freedom in real-time. A prototype nano-cell was prepared in a similar fashion as previously reported [45], [94]. The samples comprising $SiO_x$-coated SiNTs and Ni-coated SiNTs were scraped from the substrate using a steel razor blade and glued separately to the Cu rod using conductive epoxy. The piezo-driven scanning tunneling microscope (STM) tip carried a fresh piece of Li metal, loaded in an inert environment, and which acts as a Li source as well as a counter electrode. The thin native $Li_2O$ layer, which is formed on the surface of pristine Li metal inside the TEM due to residual gases ($O_2$ and $H_2O$) in the TEM column, serves as a solid-state electrolyte, allowing the diffusion of $Li^+$ between the electrodes under potential bias. Lithiation and delithiation were performed by applying a constant bias of -4 V and +4 V, respectively.

## 5.3. Electrochemical Performance of Uncoated SiNTs and Ni-Coated SiNTs

The electrochemical performances of uncoated SiNTs and Ni-coated SiNTs are tested under galvanostatic conditions in traditional liquid electrolyte coin cells with Li metal as the counter electrode (see *Experimental Methods* for details).

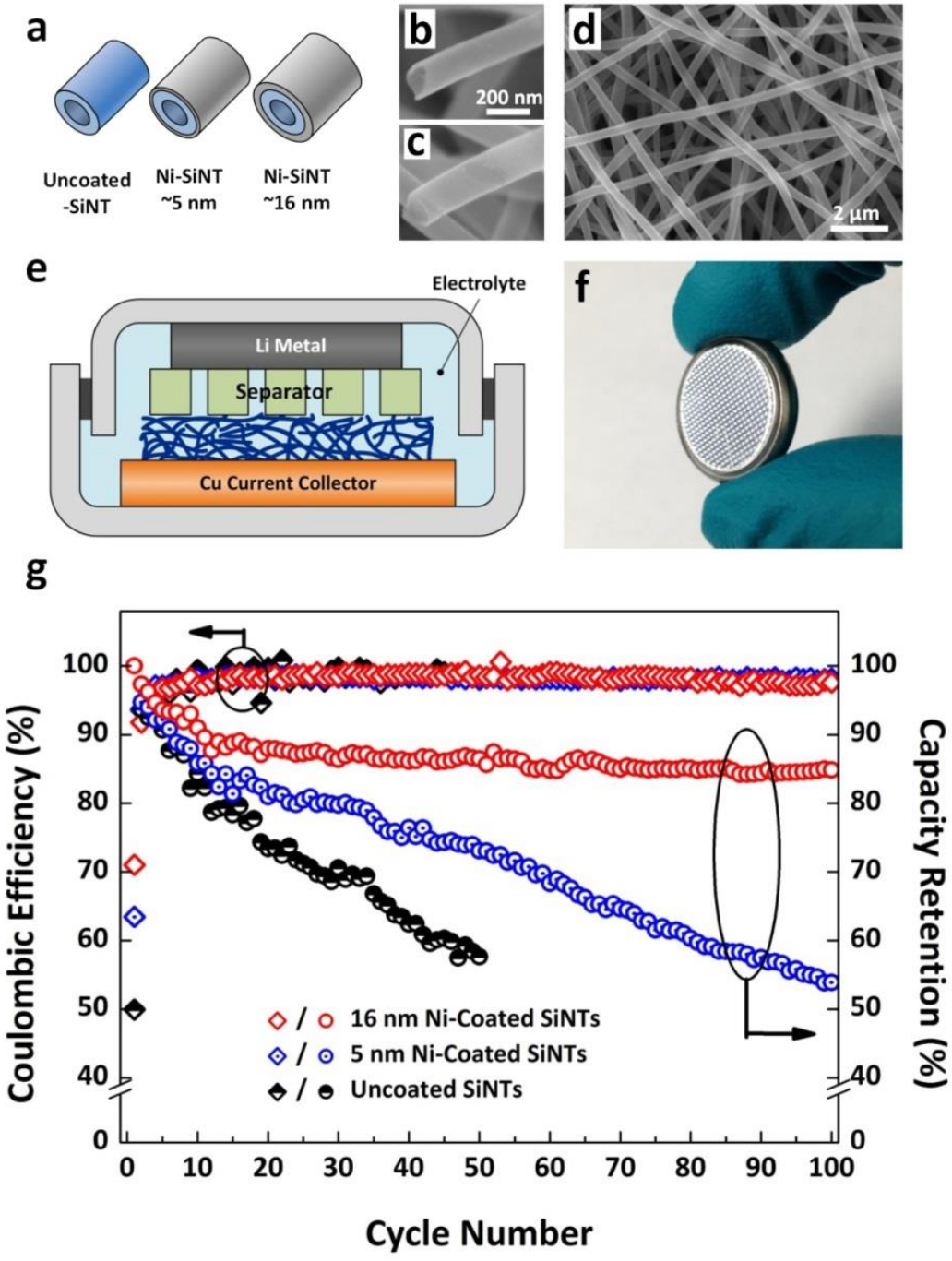


Figure 5.1: Electrochemical performance of uncoated SiNTs and Ni-coated SiNTs. (a) Schematics showing uncoated SiNT and SiNTs with Ni coating thicknesses of ~5 nm and ~16 nm. Scanning electron microscopy (SEM) images of individual SiNTs (b) without Ni coating and (c) with ~16 nm Ni-coating. (d) A lower magnification SEM

image of a SiNT mat prepared for coin-cell cycling. (e) A schematic of the coin-cell configuration with Li metal as counter electrode and SiNTs as working electrodes. (f) A representative coin-cell after assembly. (g) Curves showing coulombic efficiency (CE) and capacity retention for uncoated SiNTs and SiNTs with Ni coating thicknesses of ~5 nm and ~16 nm. Compared to the uncoated SiNTs, adding Ni-coating layers improves the capacity retention of the cell for at least 100 cycles. Same scale bar in (b) and (c)

Figure 5.1a shows schematics of SiNTs prepared by a carbon nanofiber nanotemplating method [99] (see *Experimental Methods* section for details). Three sets of SiNTs, one without any metallic coatings and the other two with sputter-coated Ni layers of different thicknesses prepared using direct current (DC)-magnetron sputtering, are tested for the electrochemical performance. The free-standing uncoated SiNTs or Ni-coated SiNTs mats are directly used in cell assembly and electrochemical tests without using any binder and conductive additives (Figure 5.1b-f), as would be desired for maximum specific capacity in applications.
Figure 5.1g shows the delithiation capacity retention of three electrodes with respect to the delithiation capacity of the 1$^{st}$ cycle. As shown in Figure 5.1g, after 50 lithiation-delithiation cycles, the delithiation capacity of the uncoated SiNTs electrode quickly decreases to only ~55 % of the 1$^{st}$ delithiation capacity. Although the ~5 nm Ni-coated SiNTs electrode shows slightly improved cycling performance compared with the uncoated SiNTs electrode, the capacity still fades during repeated cycling, with only 52 % capacity left after 100 cycles. However, when the thickness of Ni-

coating is increased to ~16 nm, the material shows excellent capacity retention with 85 % capacity retained after 100 cycles. More importantly, almost no capacity decay is observed after the 20$^{th}$ charge-discharge cycle. Figure 5.1g clearly demonstrates that the ~16 nm Ni-coated SiNTs electrode shows superior cycling performance compared with the other two electrodes.

Detailed galvanostatic charge-discharge profiles are shown in Figure 5.2 where all three electrodes exhibit a long voltage plateau at ~200 mV (*vs.* Li/Li$^+$) during the first lithiation, suggesting a two-phase lithiation mechanism in the first cycle, consistent with recent *in situ* TEM studies of amorphous silicon [127], [128].

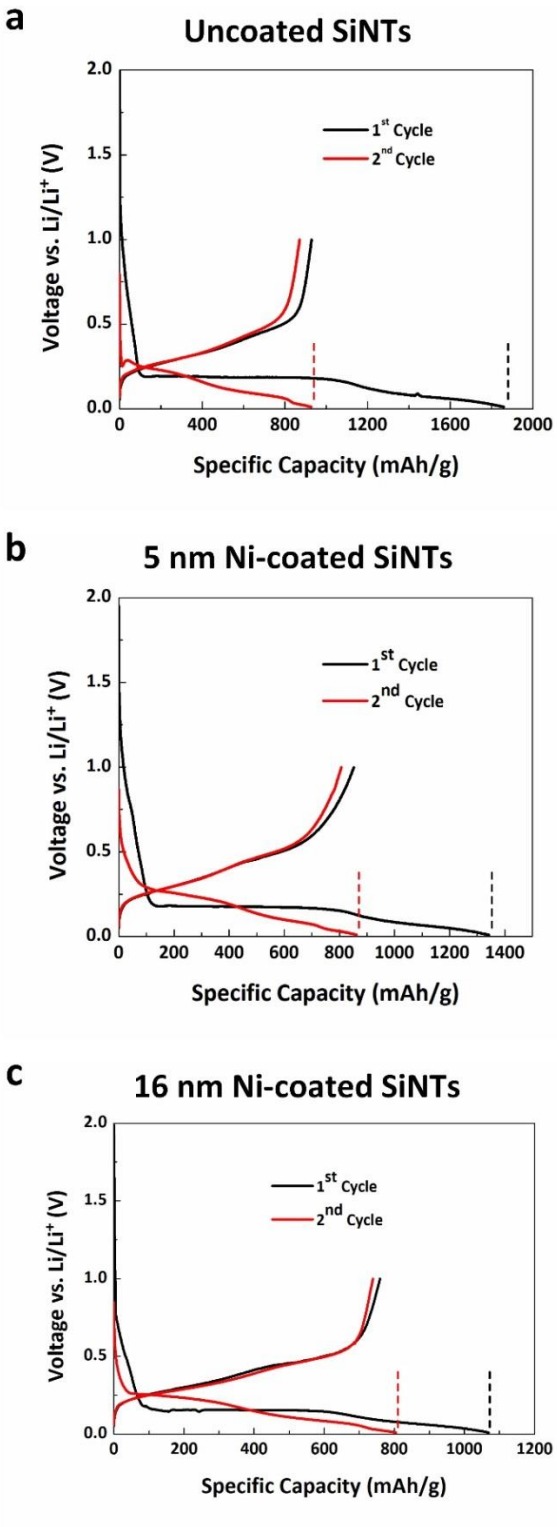


Figure 5.2: Galvanostatic charge/discharge profile of (a) uncoated SiNTs (b) SiNTs with ~5 nm Ni coatings (c) SiNTs with ~16 nm of Ni coatings.

In the second and subsequent cycles, the voltage profiles show sloping curves, which are typical charge-discharge behaviors of amorphous silicon and indicate that the lithiation/delithiation follow a single phase solid solution reaction pathway. Based on the total weight of the electrode (active silicon with Ni coating) material, the first delithiation capacity and coulombic efficiency (CE) of uncoated SiNTs are measured to be 930 mAh/$g_{electrode}$ and ~50 % respectively. Similarly, the first discharge capacity and CE of ~5 nm Ni-coated SiNTs and ~16 nm Ni-coated SiNTs are 850 mAh/$g_{electrode}$ and ~63 %, and 760 mAh/$g_{electrode}$ and ~71 %, respectively. The overall specific capacity of two Ni-coated SiNT electrodes is slightly lower than that of the uncoated SiNT electrode, mainly due to the much higher mass density of Ni compared with amorphous Si. It is notable that the uncoated SiNTs achieve a discharge capacity of 930 mAh/$g_{Si}$, whereas the ~16 nm Ni-coated SiNTs achieve over 3000 mAh/$g_{Si}$, which shows that the Ni helps to maintain the mechanical and electronic integrity of the SiNT structure. We also note that the first-cycle CE is much lower for the uncoated SiNTs than that of ~5 nm Ni-coated SiNTs and ~16 nm Ni-coated SiNTs. This lower initial CE of uncoated SiNTs is probably caused by a large outward expansion of the SiNTs that breaks the SEI film during lithiation and delithiation, thus forming a thicker SEI layer that contributes to increasing cell impedance. On the other hand, the high CE in the Ni-coated SiNTs can be attributed to a stable SEI, resulting from the confinement of outward volume changes during lithiation and delithiation. To elucidate the origins of the different cycling behaviors of the above three electrodes, *in-situ* TEM was used to directly observe all three electrodes during lithiation and delithiation cycling.

5.4. Lithiation and Delithiation of Uncoated SiNTs

Using an *in-situ* TEM platform, as reported in our previous studies [45], [94], a nano-electrochemical cell comprising individual SiNTs, Li metal counter electrode and natively grown $Li_2O$ electrolyte layer is constructed inside the TEM (Figure 5.3a).

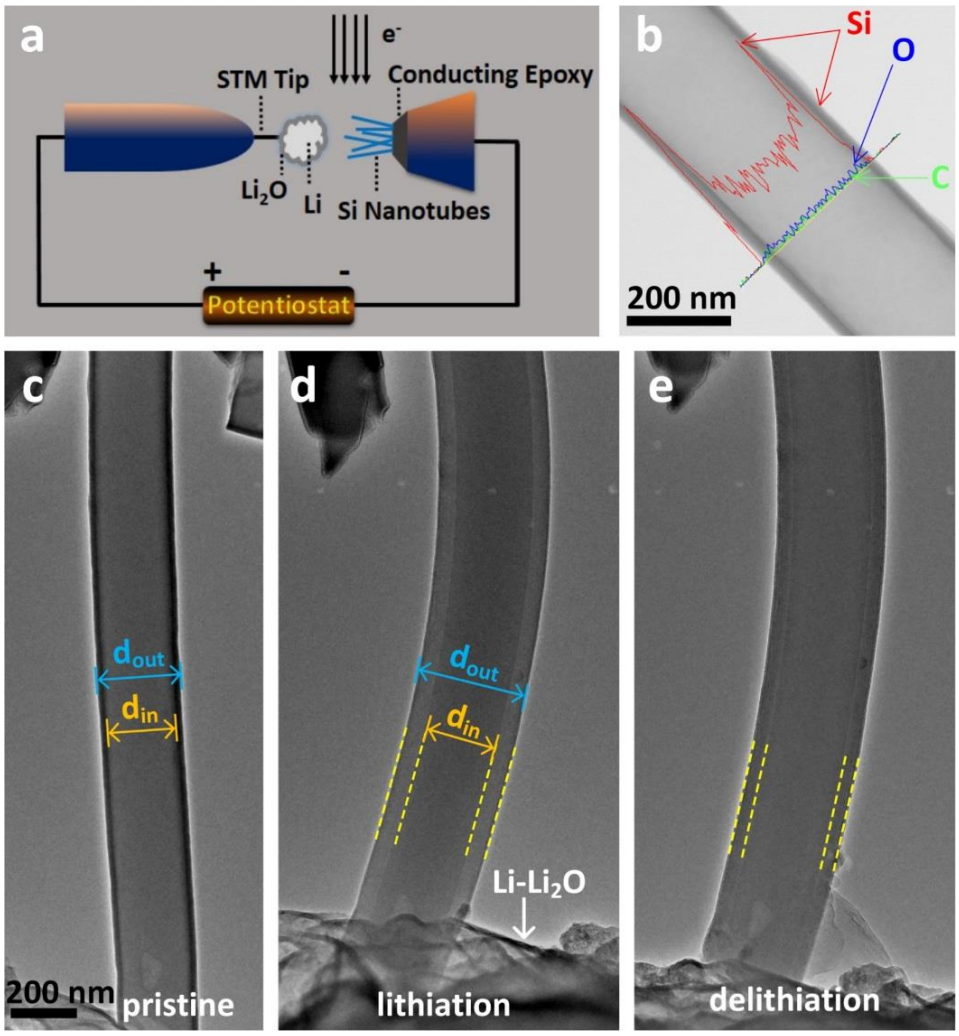


Figure 5.3: Lithiation and delithiation of an uncoated silicon nanotube (SiNT). (a) A schematic of nano-electrochemical setup inside the TEM. (b) A representative energy dispersive x-ray spectroscopy (EDS) line profile scan across the SiNT shows strong Si peaks at the outer shell with little or no trace of C in the inner part. This demonstrates that the oxidation process has successfully removed the inner carbon

core. (c) A pristine uncoated SiNT having inner diameter ($d_{in}$) ~213 nm and outer diameter ($d_{out}$) ~253 nm. (d) By applying a bias of -4 V with respect to Li metal, SiNT undergoes lithiation with the following dimensional changes: $d_{in}$ ~229 nm and $d_{out}$ ~333 nm. (e) During delithiation, biasing +4 V with respect to Li metal, the SiNT shrinks in size but does not reach to the pristine level. The $d_{in}$ and $d_{out}$ of the delithiated SiNT are ~227 nm and ~324 nm respectively. Same scale bar (c-e).

During the electrochemical cycling, a piezo-driven scanning tunneling microscopy (STM) tip carrying a Li metal source is brought in contact with the cantilevered end of the individual SiNT and a constant bias with respect to Li metal is applied to the nanotube. Figure 5.3b shows a representative uncoated SiNT, with its carbon core completely removed by the thermal oxidation process described in the *Experimental Methods* section. Figure 5.3c shows a side-view of such a SiNT with inner ($d_{in}$) and outer ($d_{out}$) diameters of ~213 nm and ~253 nm, respectively. Upon application of a constant bias with respect to Li metal (-4 V unless otherwise specified), Li propagates axially along SiNT, lithiating first on the outer surface of the wall followed by the inner core until it reaches the fully lithiated state (Figure 5.3d). After the SiNT is fully lithiated, the $d_{in}$ and $d_{out}$ are measured to be ~229 nm and ~333 nm, respectively, demonstrating an outward-radial volume expansion of ~210 % and no inward expansion towards the core of the tube. It is notable that even the inner surface expands in the outward direction. As the reverse bias with respect to the Li metal is applied (+4 V unless otherwise specified), Li is extracted back, causing the SiNT to shrink (Figure 5.3e). The $d_{in}$ and $d_{out}$ of delithiated SiNT are measured to be ~227 nm

and ~324 nm, respectively. This lithiation and delithiation process has been repeated on a number of similarly-prepared SiNTs, all with quantitatively comparable results. Interestingly, a previous study with *post mortem* TEM [99] of similarly-prepared SiNT structures showed indications of a strong constraining effect of a 10 nm thick thermally-grown $SiO_x$ surface layer, in which the silicon expanded only inwardly, towards the core, with no appreciable outward expansion during lithiation. However, no such constraining effect is observed with our electrochemical setup for our uncoated nanotubes, with only ~4 nm $SiO_x$ coating. We note that the thickness of the $SiO_x$ layer for the SiNTs we describe here is thinner than that reported in Ref. 98, although we used a similar fabrication procedure. This thin $SiO_x$ apparently cannot force the SiNT to expand inward. We also point out that a number of studies conclude that $SiO_x$ and other silicon oxides are not strictly inert to lithium [78], [129]–[131], and these chemical reactions of $SiO_x$ with Li may alter its mechanical toughness. Further study is warranted to investigate the precise relationship between surface oxide composition & thickness to the lithiation- and delithiation-induced volume changes in SiNTs. However, this is beyond the scope of the present study. Instead, we choose to focus on a coating which is known to have high electron and Li ion mobility, yet is also inert against alloy formation and other insertion reactions. For this role, nickel presents an ideal model material with which to study the mechanical effects of a clamping layer independent of other electronic, ionic, or electrochemical considerations [120], [121].

5.5. Lithiation and Delithiation on Nickel-Coated SiNTs

To evaluate the role of surface coatings in constraining the volume expansion of SiNTs during lithiation, we sputter-coat SiNTs with Ni using DC-magnetron sputtering. Figure 5.4 shows *in-situ* electrochemical cycling and simultaneous structural evolution observed during lithiation of Ni-coated SiNTs with various coating thicknesses of ~2 nm, ~5 nm and ~16 nm, together with schematics showing the expansion exhibited upon first lithiation of these structures (Figures 5.4b and 5.4c) and also the uncoated case (Figure 5.4a).

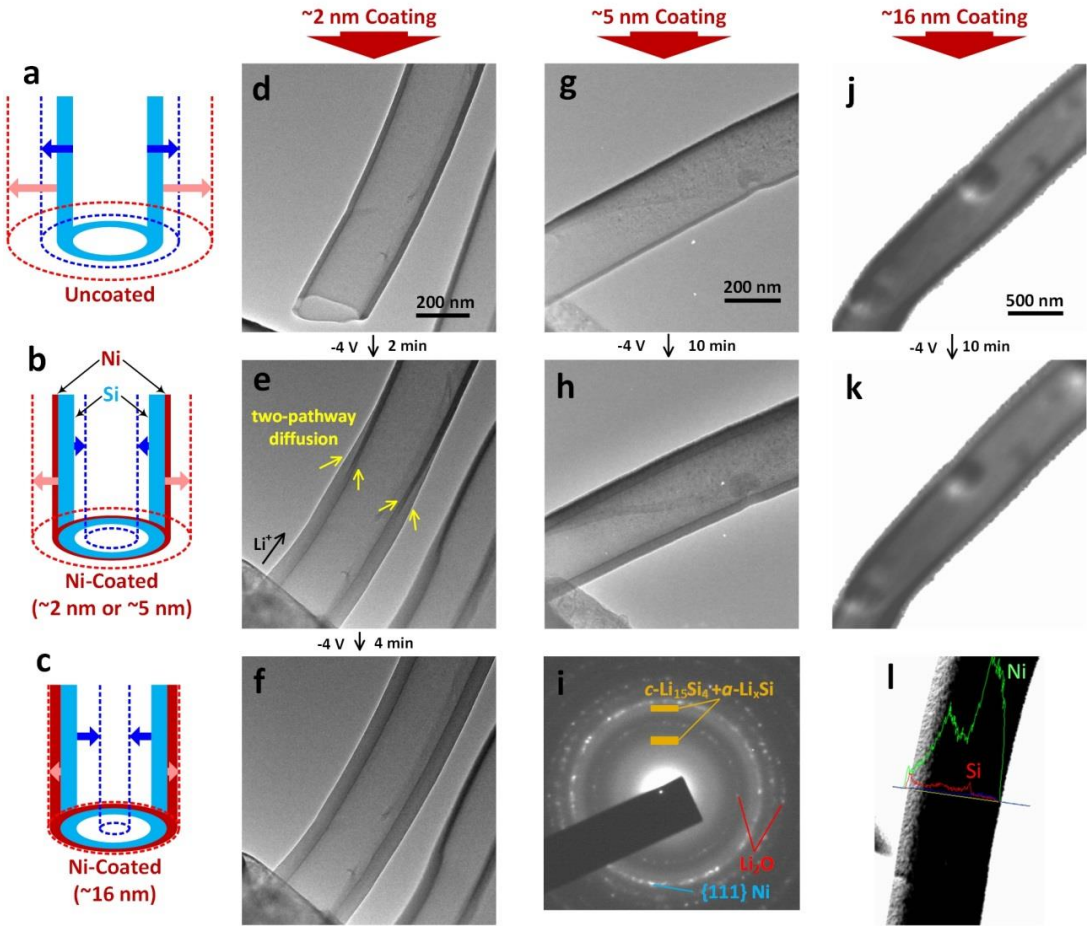


Figure 5.4: Comparison of lithiation behavior and simultaneous volume changes in SiNTs with different nickel coating thicknesses. (a, b, c) Schematics of uncoated

SiNT and SiNT with nickel deposition thicknesses of ~2 nm, ~5 nm and ~16 nm, as labeled (not to scale). The red and blue arrows show the direction and relative amount of expansion during the first lithiation of the outer diameter and inner diameter, respectively. (d) A ~2 nm Ni-coated SiNT with as-fabricated $d_{in}$ ~263 nm and $d_{out}$ ~324 nm. (e) As a bias of -4 V with respect to Li metal is applied to the SiNT, lithiation progresses axially following a two- pathway diffusion. The faster diffusion of lithium across the surface results in a tapered interface between the lithiated and unlithiated silicon. (f) A fully lithiated silicon with $d_{in}$ ~245 nm and $d_{out}$ ~380 nm. Although there is a considerable increase in $d_{out}$, the decrease in the $d_{in}$ suggests that the Ni layer is constraining the outer expansion of silicon to some extent. Same scale bar (d-f). (g) SiNT with Ni coating of ~5 nm and as-fabricated $d_{in}$ of ~218 nm and $d_{out}$ of ~263 nm. (h) After lithiation, $d_{in}$ and $d_{out}$ are measured to be ~203 nm and ~290 nm respectively. It is clear that there is lesser outer expansion and more towards the inner core as the thickness of the Ni coating is increased. Same scale bar (g & h). (i) An EDP image on the lithiated SiNT (h) shows the presence of polycrystalline $Li_{15}Si_4$ (*c*-$Li_{15}Si_4$), amorphous $Li_xSi$ (*a*-$Li_xSi$), $Li_2O$ and Ni. (j) SiNT with Ni coating of ~16 nm, $d_{in}$ ~570 nm and $d_{out}$ ~672 nm. (k) After lithiation, there was little change in the outer diameter ($d_{out}$ ~678 nm) of the SiNT. The inner diameter shrank significantly ($d_{in}$ ~521 nm). Same scale bar (j & k). (l) An EDS line scan profile across the SiNT shows strong Ni peaks compared to Si, indicating a thicker Ni coating.

First, we discuss the case of ~2 nm Ni thickness, as shown schematically in Figure 5.4b and in electron micrographs in Figures 5.4d, 5.4e, and 5.4f. The $d_{in}$ and $d_{out}$ of as-prepared SiNTs, including the Ni-coating layers, are ~263 nm and ~324 nm

respectively (Figure 5.4d). Upon applying a constant bias with respect to Li metal, $Li^+$ ions diffuse into the silicon and propagate rapidly along the axis of the SiNT (Figure 5.4e). Notably, the lithiation follows two diffusion pathways on both the inner and outer surfaces of the SiNT [94], [99], which is evident as a tapered interface between the lithiated and unlithiated interface of the SiNT. The Li propagation is predominantly faster on the outer surface while proceeds at a slower rate in the inner core of the SiNT. The $d_{in}$ and $d_{out}$ of the fully lithiated SiNT are measured to be ~245 nm and ~380 nm respectively, of which the outward radial expansion of $d_{out}$ is only ~17 %, relative to its initial value, whereas $d_{in}$ now exhibits an *inward* expansion, of ~7 % (Figure 5.4f). The still outwardly-directed overall expansion of the SiNT suggests that this relatively thin coating layer of nickel (~2 nm) is unable to constrain the volume changes experienced by SiNT during lithiation. However, it can be noted that it does result in some improvement in constraining the outer radial expansion, over the uncoated SiNTs (Figure 5.3).

Now, we turn to a discussion of ~5 nm Ni thickness samples, as shown schematically in Figure 5.4b and in electron micrographs in Figures 5.4g and 5.4h. The rougher surface texture of the as-prepared Ni-coated SiNTs is consistent with the grain growth of the thicker nickel film (Figure 5.4g). The measured $d_{in}$ and $d_{out}$ in the unlithiated state are measured to be ~218 nm and ~263 nm and changed to ~203 nm and ~290 nm after lithiation, respectively. Figure 5.3i shows an electron diffraction pattern of the lithiated SiNT shown in Figure 5.4h. The pattern indicates the presence of polycrystalline $Li_{15}Si_4$, Ni, $Li_2O$, and an amorphous $Li_xSi$ phase (*a*-$Li_xSi$), consistent with previous studies [53], [94], [104]. When the Ni coating is increased

from ~2 nm to ~5 nm, the outer radial expansion of the SiNT reduced from ~17 % to ~10 %, while the inward expansion (contraction) is maintained at ~7 % during a similar reaction time. Moreover, no sign of surface cracks or Ni-Si interfacial debonding is observed during lithiation and delithiation, which suggest that any Ni deformation still occurs within the ductile limit. In core-shell nanostructures, material interfaces can sometimes serve as a nucleation site for cracking and delamination, due to compressive stress [132]. However, Si coatings on Ni have previously been shown to exhibit strong Ni-Si interfacial bonding even after hundreds of electrochemical cycles [133], consistent with the results we report here.

Figures 5.4j and 5.4k show the case of a relatively thick Ni coating layer of ~16 nm applied to the SiNT, yielding $d_{in}$ and $d_{out}$ that are measured to be ~570 nm and ~672 nm, respectively. An energy dispersive X-ray spectroscopy (EDS) line scan profile across a similar nanotube shows higher peaks of Ni on the surface (Figure 5.4l), with only modest nonuniformity of Ni coating thickness. Figure 5.4k shows the same SiNT as 4j after lithiation, and its measured $d_{in}$ and $d_{out}$ are found to be ~521 nm and ~678 nm, respectively. Here, the Si expands almost exclusively towards the inner core (~9 % contraction of $d_{in}$), while relatively little expansion is seen on the outer surface of the nanotube (only ~1 % increase in $d_{out}$). We also note that the two-pathway lithiation process, clearly observed in the case of ~2 nm coating, appears to be reduced to just the inner pathway for the ~16 nm case. This occurs in spite of the fact that Ni has been shown to have high Li mobility in other studies [120], [121]. We observe that increasing the Ni coating thickness in fact blocks the outward volume expansion of the SiNT, simply because the hoop stress caused by this expansion is

not able to overcome the tensile strength of the nickel coating layer. In the ~5 nm case, the two pathways proceed with similar ease due to the hoop stress, the outer pathway being constrained by the ductile expansion of Ni and the inner pathway by the SiNT itself.

Table 5.1 shows the summary of relative dimensional changes in the $d_{in}$ and $d_{out}$ of pristine and lithiated SiNTs with and without Ni coatings.

Table 5.1: Summary of relative dimensional changes of silicon nanotubes upon lithiation.

| **Uncoated (% change)** | | **Ni (~2 nm) (% change)** | | **Ni (~5 nm) (% change)** | | **Ni (~16 nm) (% change)** | |
|---|---|---|---|---|---|---|---|
| **Outer diameter** | **Inner diameter** | **Outer diameter** | **Inner diameter** | **Outer diameter** | **Inner diameter** | **Outer diameter** | **Inner diameter** |
| 35.7 | 9.0 | 17.3 | -6.8 | 10.2 | -6.9 | 0.9 | -8.6 |
| 31.6 | 7.5 | 23.5 | -6.6 | 9.5 | -6.9 | 0.2 | -18.8 |
| 26.3 | 4.7 | 20.6 | -8.3 | 8.0 | -4.3 | 0.2 | -17.5 |

In the uncoated SiNTs, the expansion of the silicon wall during lithiation is primarily in the radially outward direction. There is no inward expansion towards the tubular core of SiNT. However, with additional surface coatings of SiNTs with Ni, the outer expansion of the silicon wall can be controlled. At ~2 nm of Ni coating, SiNTs undergo expansion both outwardly as well as inwardly, toward the core. The outer expansion is significantly constrained at ~5 nm of Ni coating, and going to ~16 nm produces a structure exhibiting almost no expansion on the outer surface, while much of the silicon expansion is forced inward towards the core. Based on the observations collected in Table 5.1, it is clear that Ni coatings can be beneficial in suppressing the

lithiation-induced volume expansion in SiNTs. As Ni is a good electronic conductor, no conductive additives are needed, thereby lowering the size and weight of a cell, even though Ni is an inactive material for Li storage. From the comparative studies using different Ni coating thickness (Table 5.1), we estimated the optimum thickness of Ni coatings to be in the range of ~5-16 nm. We note that the coatings used here were applied using DC-magnetron sputtering, which, despite the high-porosity and transparency of the SINT mats, is still a somewhat directional process producing slight thickness non-uniformities. More efficient use of coating materials may be achieved through a more conformal technique such as atomic layer deposition (ALD) in future work. Furthermore, using stronger materials than Ni may be able to realize the same hoop-strong clamping mechanism with even thinner coatings.

## 5.6. Summary

Using *in-situ* TEM studies, we directly observe the electrochemical lithiation/delithiation behavior and the nature of volume changes in individual SiNTs, both uncoated and with Ni coatings of different thickness. In uncoated SiNTs, the lithiation-induced volume expansion was predominantly in the outer radial direction, while no inward-directed expansion was observed. We find that the thickness of $SiO_x$ grown by low temperature thermal oxidation (~4 nm at 500 ˚C) cannot sustain the huge stress produced by SiNT during lithiation. In Ni-coated SiNTs, the suppression of the outer volume expansion was readily achieved and improved as the thickness of the Ni coating layer was increased. We compare the electrochemical performance between uncoated SiNTs and SiNTs with ~5 nm and ~16 nm of Ni coatings, and we find that Ni-coated SiNTs demonstrate excellent initial CE and stable capacity

retention for at least 100 cycles. The presented results and associated analyses provide insightful guidelines for a viable design of hollow silicon nanostructures for lithium-ion battery applications.

## 5.7. Acknowledgement

I conceived and designed the experiments, along with Prof. John Cumings and Prof. Chunsheng Wang. ChuanFu Sun and Prof. Yuhuang Wang performed Si deposition using LPCVD. Yihang Liu performed Ni coatings. Yujie Zhu performed coin-cell cycling and testing. Xin Zhang and Prof. Briber helped with microtome. I analyzed all other TEM results. Prof. Liangbing Hu provided valuable insights in the overall discussions.

# Chapter 6: Summary, Conclusions, and Future Work

*In-situ* TEM is a powerful tool to study the fundamental properties of nanostructured materials. Conventionally, the properties of battery materials are studied by evaluating the overall performance of a cell. There has historically been little attention focused on understanding the physical and chemical behaviors of individual electrodes or structures. Unfortunately, the current strategy of studying LIB materials can be ineffective and time-consuming if the goal of developing batteries with high-energy and high-power densities needs to be achieved. Therefore, understanding the behavior of the materials bottom-up from the atomic level can be critical for tailoring and designing of robust electrodes for future LIBs. On that basis, my dissertation focuses on using *in-situ* TEM technique to investigate individual silicon nanostructures, during charge and discharge in real-time. The one-dimensional silicon nanostructures such as SiNWs were previously thought to withstand the massive volume changes (~ 300 – 400 %) during cycling. However, our studies show an anisotropic volume expansion and simultaneous cracking in *c*-SiNWs. The SiNWs having the growth direction of [112] showed preferential diffusion of $Li^+$ ions, more towards [110] direction compared to [111]. The dumb-bell shape observed in TEM clearly demonstrated the anisotropic swelling and deformation mechanism of lithiated *c*-SiNWs. Further *in-situ* experiments on *c*-SiNWs grown along [100], [110] and [111] directions may be necessary to understand the correlation between lithium diffusivity and crystal orientation in details. To improve the effectiveness of the

study, a TEM 3D tomography capable of high-angle tilt series could be implemented. I designed and built a TEM holder pin capable of a tilt series with ±60˚ (Figure 6.1), which could be used to capture series of 2D images. By using commercial software such as TEMography, a 3D reconstruction of 2D captured images could be produced and analyzed for detail understanding of the material's properties.

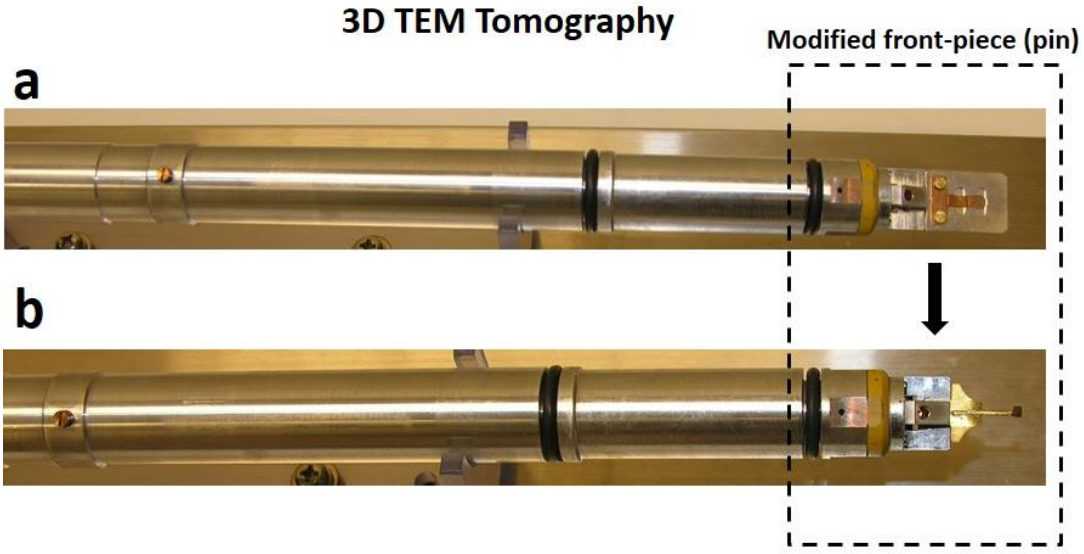


Figure 6.1: A custom-built TEM tomography holder pin. (a) A conventional TEM single-tilt holder with ±30˚ tilt series. (b) A modified pin designed to fit in holder shown above in (a) and is capable of ±60˚ tilt series.

Using this tomography setup, further investigations on the morphology of void formation and distribution as a function lithiation/delithiation rate in SiNWs (discussed in Section 3.2 of Chapter 3) can be performed.

We also studied heterogeneous nanostructures, focusing on CNT@α-Si chemistry in collaboration with Prof. YuHuang group at the Department of Chemistry and Biochemistry (UMD). The CNT@α-Si core-shell heterostructures provide significant benefits with CNT core working as a robust supporting framework and continuous

pathway for electrical conductivity, while α-Si acting as $Li^+$ ions storage-medium. To find the mechanical reliability of CNT@α-Si at the interface, we performed TEM bending test. We concluded that these heterostructures show strong dependence on the CNT surface chemistry. By carefully controlling the CNT chemistry with carboxylic $-(CH_2)_5COOH$ functional groups, we synthesized uniform and bead-string CNT@α-Si core-shell nanostructures, and performed *in-situ* TEM lithiation and delithiation experiments. We conclude that novel heterostructures such as bead-string CNT@α-Si can accommodate huge volume changes during TEM cycling without appreciable mechanical failure. Although, individual core-shell CNT@α-Si heterostructures show promising outcomes, future studies are warranted to evaluate their collective performance when used in a coin-cell.

Finally, we also conducted studies on hollow silicon nanostructures focusing on SiNTs. The SiNTs can accommodate the lithiation/delithiation induced volume changes by providing stress relief through hollow internal voids. A previous study by Hu and co-workers [99] proposed to use a 10 nm $SiO_x$ coating as a mechanical clamping layer on the outer surface of a SiNT electrode, to prevent the outward expansion that can damage the SEI. However, our *in-situ* TEM studies showed no such constraining behavior with a ~4 nm $SiO_x$ layer. By coating SiNTs with Ni (2, 5, and 16 nm), lithiation-induced volume expansion was significantly improved. Additionally, the coin-cell cycling with 30-100 times more mass-loading with Ni-coated SiNTs showed good capacity retention compared to uncoated SiNTs (~ 4 nm of $SiO_x$ coatings). For the future work, the more efficient and conformal $SiO_x$ coatings layer of ~10 nm thickness could be achieved either through the conventional

thermal treatment route or from atomic layer deposition (ALD) technique. Below, I show the preliminary results with low temperature oxidation (LTO) coated $SiO_x$ layer on individual SiNTs (Figure 6.2). The thickness of the $SiO_x$ produced were found to be in the range between 28 to 30 nm. *In-situ* TEM lithiation was performed on one of the SiNTs with $d_{out}$ and $d_{in}$ of 347 and 252 nm, respectively (Figure 6.3a). Figure 6.3b shows Si wall expanding both outwardly as well towards inner direction, demonstrating the inability of ~29 nm $SiO_x$ coating to fully constrain the outer volume expansion of SiNT. Further study is warranted to investigate the precise relationship between surface oxide composition and thickness to the lithiation- and delithiation-induced volume changes in SiNTs.

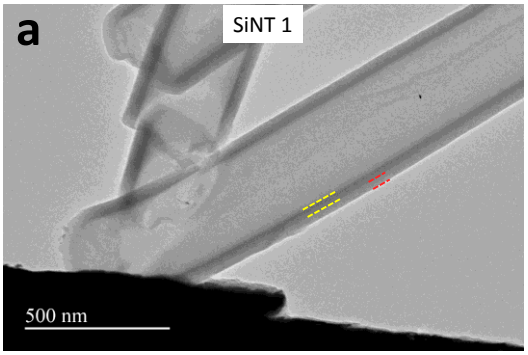


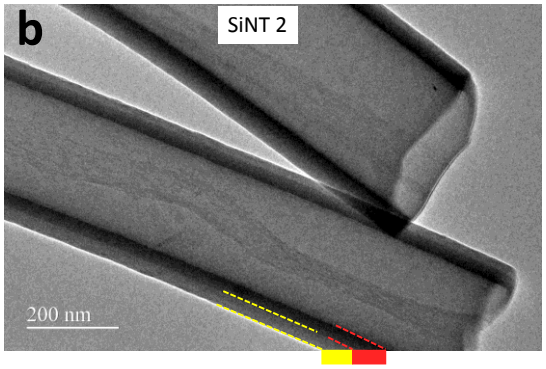


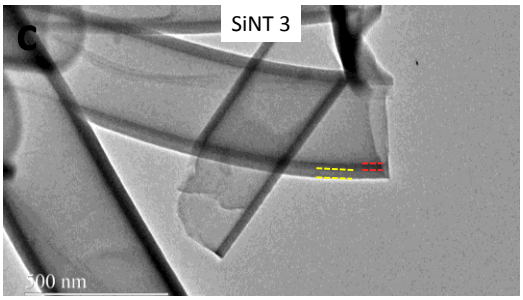


d

| SiNT | $d_{out}$ (nm) | $d_{in}$ (nm) | SiNT thickness (nm) | $SiO_x$ thickness (nm) |
|---|---|---|---|---|
| 1 | 384 | 287 | 26 | 29 |
| 2 | 324 | 220 | 28 | 29 |
| 3 | 375 | 280 | 25 | 28 |

Figure 6.2: (a-c) SiNTs with $SiO_x$ coatings prepared from low temperature oxidation (LTO) technique. (d) A table showing measured SINT wall and $SiO_x$ thicknesses.

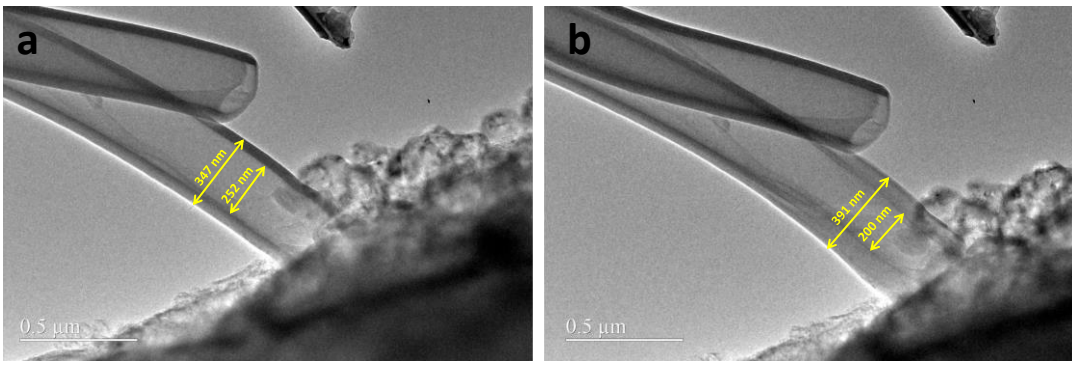


Figure 6.3: Lithiation of SiNT with LTO-coated $SiO_x$ layer. (a) Pristine SiNT with $d_{out}$= ~ 347 nm and $d_{in}$= ~ 252 nm. (b) After lithiation, $d_{out}$ and $d_{in}$ are 391 and 200 nm, respectively. The Si wall expanded more towards inner core (~21 %) and less towards outer direction (~13 %).

Finally, the scope of current *in-situ* TEM technique can be extended to study various cathode materials, to investigate SEI formation mechanism, and to understand other electrochemical processes in LIBs. These studies could also be extended beyond lithium-ion, focusing on lithium-air or sodium ion batteries, etc. The design of the current experimental setup could be modified as demanded by future needs or studies.

# Appendices

## Appendix A: A Simplified Model for Calculation of Shear Strength at the Welded Interface of the Crossed SiNWs

*The following analysis is performed with help from Eric Epstein, a former undergraduate student in our Group and has been published: Ref.*[45].

The total deflection of the SiNW described in Section 3.3.3, and as shown in Figure 3.7g in the transverse direction is a superposition of the two deflections caused by $F_1$ and $F_{shear}$. For $F_{shear}$, only its component along the transverse direction, labeled as $F_{bend}$, contributes to the deflection of the SiNW. To determine the shear strength at the welded interface, we first estimate $F_{bend}$. The equations that follow are derived using the double integration method on the governing equation for the deformation of an elastic beam: $\frac{d^2y(x)}{dx^2} = \frac{M}{EI}$, where y(x) is the deflection of the beam as a function of location x, M is the bending moment of the beam with respect to its neutral axis, I is the area moment of inertia of the beam (= $2.9 \times 10^{-29}$ $m^4$ , using SiNW radius of 78 nm and assuming a circular cross-section), and E is the elastic modulus of the beam (taken to be 68.6 GPa, representative for amorphous Si, taken from various literatures). In all calculations, the origin is taken to be the tip of the SiNW. The unknown value of $F_A$ is a superposition of two forces: a reaction force from the pin in the bottom right of Figure 3.7g and $F_1$, the force that would be required to produce deflection $\delta_1$ in the absence of $F_{bend}$. We compute $F_1$ according to the following equation,

$$F_1 = \frac{3EI\delta_1}{L^3} \cong 7.7 * 10^{-6}\text{N}. \quad (1)$$

Here, L is the length of the SiNW (5780 nm) and $\delta_1$ = 2480 nm is the transverse displacement from the neutral axis of the undeflected SiNW (Figure 3.7a) to the neutral axis of the fully deflected SiNW (Figure 3.7f). From this estimate of $F_1$, we calculate the deflection near the intersection of two welded SiNW (labeled by $x_c$ from the origin) as it should be, if $F_1$ were the only force acting on the SiNW,

$$\delta_{calc} = \frac{F_1}{6EI}(2L^3 - 3L^2x_c + {x_c}^3) \cong 580\ \text{nm}. \quad (2)$$

However, $F_{bend}$ from the secondary SiNW causes the observed deflection at $x_c$ to deviate from the above-calculated value by an amount, $\delta_2$ = 430 nm, which is directly measured from microscope images near the welded intersection (see Figure 3.7). Thus, $\delta_2$ is the additional deflection induced by $F_{bend}$ at $x_c$, as illustrated in the bottom right configuration in Figure 3.7g. The force $F_{bend}$ can be calculated from $\delta_2$ according to the following equation,

$$F_{bend} = \frac{12EIL^3\delta_2}{a(L-x_c)^2[3L(a^2-L^2)+(L-x_c)(3L^2-a^2)]} \cong 6.6 * 10^{-7}\text{N}, \quad (3)$$

where a is the distance from the pinned end of the SiNW to the point where $F_{bend}$ is applied. Using the included angle between $F_{bend}$ and $F_{shear}$ (24°), the value of $F_{shear}$ can then be estimated. The shear strength at the welded junction (the stress prior to failure) can be then calculated by dividing $F_{shear}$ by the cross-sectional area of the welded junction. To estimate an upper bound of the welded area, we can use the total cross-section of the nanowires as it appears in projection in a TEM image, yielding a lower bound on the shear strength of 140 MPa. However, two cylindrical nanowires would be unlikely to form a weld with such a large cross-sectional area. To improve

the estimate, we can use a geometrical model, incorporating space-filling during the lithiation expansion followed by uniform contraction, to obtain a more accurate estimate of the cross-sectional area. From this more realistic geometrical model, we obtain a shear strength of approximately 200 MPa. We note that the analytical model used here assumes no deflections parallel to the direction of the imaging electron beam, since all 2D images are obtained in projection. However, the manipulation piezo causing the deflections is actuated purely in the plane of the image, and thus any out-of-plane deflections are expected to introduce only minimal correction factors. We note that the above analysis assumes no bending moment is introduced due to the torsional loading of the weld itself. If such a load were included, then the inhomogeneous stress within the weld would result in an increased estimate of the strength of the weld material. We further note that the geometry of the lithiated nanowires can be anisotropic, as described in Section 3.1.2. However, we neglect this effect because the degree of anisotropy is dependent upon the degree of lithiation. The welded SiNWs used in our study are not highly anisotropic because the SiNWs are not fully lithiated, and thus the above model is expected to be a good approximation.

# Appendix B: Estimation of Shear Strength at the Welded Interface via Nonlinear Finite Element (FEA) Analysis of the Large Deformation of SiNW

*The following analysis is performed by Professor Teng Li and his graduate student Zheng Jia at UMD Department of Mechanical Engineering and has been published: Ref.* [45].

The simplified analytical model delineated in Section 3.3.3 guarantees a good estimate of the shear strength at the welded interface of the crossed SiNWs only when the deflection of the SiNW is not significantly large. To further quantify the effect of the large deflection of the SiNW in our *in situ* experiment as shown in Figure 3.7, we next carry out a three-dimensional finite element analysis (FEA) accounting for the nonlinear geometric effect of the large deformation of the SiNW, using the software package, ABAQUS v6.10. The FEA model considers a similar suspended cantilever SiNW as illustrated in Figure 3.7g. The free end of the SiNW is subject to a displacement $\delta$ with two components of $\delta_x$=2150nm and $\delta_y$ = 3020nm, which are measured by direct comparison of the *in situ* TEM images of the un-deformed and deformed SiNW. The effect of the secondary SiNW on the deformation of the suspended cantilever SiNW is introduced by a shear force $F_{shear}$ acting at the welded intersection along the axial direction of the secondary SiNW. In our FEA simulation model, the SiNW is 5780 nm long and its cross-section is assumed to be circular with a radius of r =78nm. The SiNW is modeled as linear elastic material with Young's Modulus and Poisson's ratio to be 68.6 GPa and 0.3, respectively. The SiNW is

meshed with three-dimensional-stress eight-node linear brick elements (C3D8R) with sizes about 0.2r. Nonlinear geometry option is turned on in the simulations to account for the large deformation of the SiNW. The value of $F_{shear}$ is varied in simulations until the deformed shape of the SiNW reaches the best fit to the deformed SiNW as observed in the TEM image. Figure B1 plots the undeformed and deformed SiNW from the best-fit FEA simulation overlapping the TEM image of the deformed SiNW (same as Figure 3.7f). The best-fit FEA simulation gives $F_{shear} = 2.5 \times 10^{-6}$ N. Using the same method to estimate the cross-sectional area of the welded junction as described in Section 3.3.3, the shear strength is estimated to be 308 MPa, somewhat larger than that estimated by the simplified analytical model. The difference between these two estimates may be attributed to nonlinear geometric effects of the large deformation of the SiNW. However, to be conservative, the value of 200 MPa estimated by the analytical model may be taken to be the conclusion of our studies.

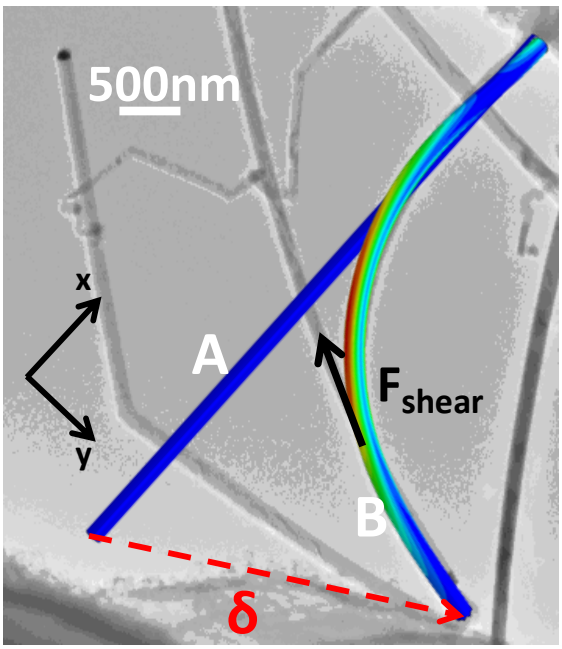


Figure B1: The undeformed and deformed shapes of SiNW from the best-fit FEA simulation are plotted over the *in situ* TEM image of the deformed SiNW (same as Figure 3.7f). The color shades represent von Mises stress levels in the SiNW.

# Appendix C: A Surface Coating Thickness Measurements for Different SiNTs

*The following analysis is performed with microtome help from Xin Zhang, a Research Associate in Professor Robert Briber Group and has been published: Ref.* [111].

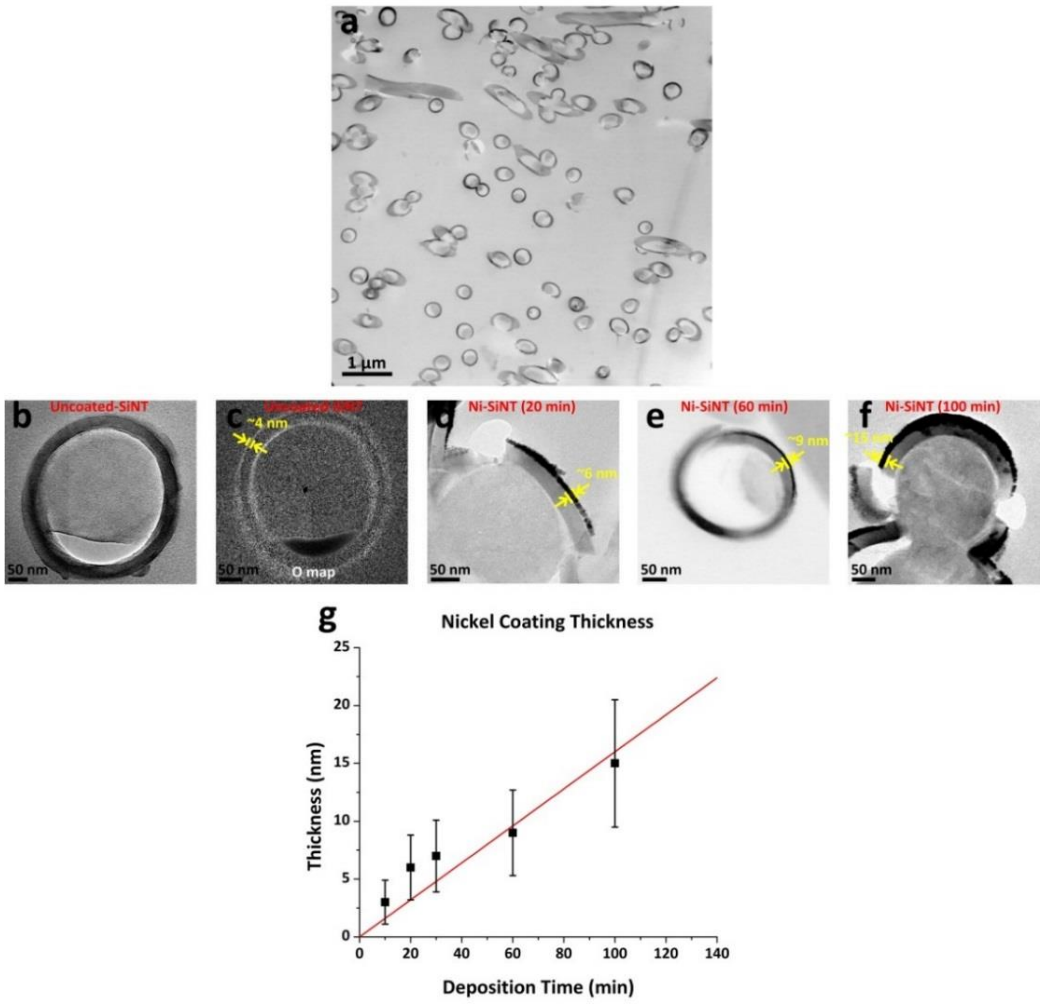


Figure C1: Surface coating thickness measurements for different SiNTs.

Figure C1a shows microtomed cross-sectional Ni-coated SiNTs on a TEM Cu grid. The coating was employed using DC-magnetron sputtering at argon gas pressure of 1Pa and target power density of 4.5W/cm$^2$. Figure C1b shows cross-sectioned SiNT

without Ni coating. An EFTEM elemental mapping showing oxygen distribution in Figure C1b is given in Figure C1c. Figures C1 (d-f) show magnified images of individual SiNTs with different Ni deposition time of 20, 60, and 100 min respectively. Measured nickel coating thickness with different deposition time is given in Figure C1g. To determine the thickness of Ni coatings on the surface of the SiNTs, a radial cross-section is produced by embedding the nanotubes in a cross-linked polymer and using a microtome cutting tool as shown in Figure C1a. An oxygen distribution mapping using energy-filtered transmission electron microscopy (EFTEM) is performed in a cross-sectioned SiNT without Ni coatings (Figure C1b). We judiciously determine the thickness of $SiO_x$ surface layer to be ~4 nm (Figure C1c). The same thickness of $SiO_x$ is also formed at the inner wall of the nanotube. For Ni coating thickness measurements, several SiNT samples with Ni deposition time of 20 min, 60 min and 100 min are selected and high-magnification TEM images are taken (Figure C1d-C1f). A thickness dependence of SiNTs is plotted with respect to different deposition time (Figure C1g). Using linear fit regression of measured Ni thickness within ±30 % error margins, we assign the thickness of Ni coatings with deposition time of 10 min, 30 min and 100 min to be ~2 nm, ~5 nm, and ~16 nm respectively. Our observations show a clean Ni-Si interface, with no indications of nickel silicide formation, which may be expected when heated above 250° C.

# References


[1] R. E. Smalley, “Top Ten Problems Facing Humanity Over the Next 50 Years,” in *Energy & Nanotechnology Conference*, 2003.

[2] J.-M. Tarascon and M. Armand, “Issues and challenges facing rechargeable lithium batteries,” *Nature*, vol. 414, no. 6861, pp. 359–367, Nov. 2001.

[3] D. Linden, *Handbook of batteries*. New York: McGraw-Hill, 1995.

[4] R. A. Huggins, *Energy Storage*. Springer, 2010.

[5] M. Winter and R. J. Brodd, “What Are Batteries, Fuel Cells, and Supercapacitors?,” *Chem. Rev.*, vol. 104, no. 10, pp. 4245–4270, Sep. 2004.

[6] H. D. Abruna, Y. Kiya, and J. C. Henderson, “Batteries and electrochemical capacitors,” *Phys. Today*, vol. 61, no. 12, pp. 43–47, 2008.

[7] X. Chen, “Tobacco mosaic virus based three dimensional anodes for lithium ion batteries,” University of Maryland, 2011.

[8] Y. Wang, H. Li, P. He, E. Hosono, and H. Zhou, “Nano active materials for lithium-ion batteries,” *Nanoscale*, vol. 2, no. 8, pp. 1294–1305, 2010.

[9] W.-J. Zhang, “A review of the electrochemical performance of alloy anodes for lithium-ion batteries,” *J. Power Sources*, vol. 196, no. 1, pp. 13–24, Jan. 2011.

[10] U. Kasavajjula, C. Wang, and A. J. Appleby, “Nano- and bulk-silicon-based insertion anodes for lithium-ion secondary cells,” *J. Power Sources*, vol. 163, no. 2, pp. 1003–1039, Jan. 2007.

[11] F. Schlachter, “No Moore’s Law for batteries,” *Proc. Natl. Acad. Sci.*, vol. 110, no. 14, p. 5273, Apr. 2013.

[12] M. S. Whittingham, “Electrical Energy Storage and Intercalation Chemistry,” *Science (80-. ).*, vol. 192, no. 4244, pp. 1126–1127, Jun. 1976.

[13] R. Teki, M. K. Datta, R. Krishnan, T. C. Parker, T.-M. Lu, P. N. Kumta, and N. Koratkar, “Nanostructured Silicon Anodes for Lithium Ion Rechargeable Batteries,” *Small*, vol. 5, no. 20, pp. 2236–2242, 2009.

[14] R. Marom, S. F. Amalraj, N. Leifer, D. Jacob, and D. Aurbach, “A review of advanced and practical lithium battery materials,” *J. Mater. Chem.*, vol. 21, no. 27, pp. 9938–9954, 2011.

[15] J. Goodenough, “Basic Research Needs for Electrical Energy Storage: Report of the Basic Energy Sciences Workshop on Electrical Energy Storage, April 2-4, 2007.”

[16] W.-J. Zhang, “Lithium insertion/extraction mechanism in alloy anodes for lithium-ion batteries,” *J. Power Sources*, vol. 196, no. 3, pp. 877–885, Feb. 2011.

[17] T. Yamaue, “Modeling Thermal Runaway for Safer Lithium Ion Batteries.” [Online]. Available: http://www.comsol.com/stories/kobelco_lithium_ion_batteries/full/. [Accessed: 12-Sep-2013].

[18] N.-S. Choi, Z. Chen, S. A. Freunberger, X. Ji, Y.-K. Sun, K. Amine, G. Yushin, L. F. Nazar, J. Cho, and P. G. Bruce, “Challenges Facing Lithium Batteries and Electrical Double-Layer Capacitors,” *Angew. Chemie Int. Ed.*, vol. 51, no. 40, pp. 9994–10024, 2012.

[19] M. Hu, X. Pang, and Z. Zhou, “Recent progress in high-voltage lithium ion batteries,” *J. Power Sources*, vol. 237, no. 0, pp. 229–242, Sep. 2013.

[20] C. M. Julien and A. Mauger, “Review of 5-V electrodes for Li-ion batteries: status and trends,” *Ionics (Kiel).*, vol. 19, no. 7, pp. 951–988, 2013.

[21] Y.-G. Guo, J.-S. Hu, and L.-J. Wan, “Nanostructured Materials for Electrochemical Energy Conversion and Storage Devices,” *Adv. Mater.*, vol. 20, no. 15, pp. 2878–2887, 2008.

[22] K. T. Lee and J. Cho, “Roles of nanosize in lithium reactive nanomaterials for lithium ion batteries,” *Nano Today*, vol. 6, no. 1, pp. 28–41, Feb. 2011.

[23] N.-S. Choi, Y. Yao, Y. Cui, and J. Cho, “One dimensional Si/Sn - based nanowires and nanotubes for lithium-ion energy storage materials,” *J. Mater. Chem.*, vol. 21, no. 27, pp. 9825–9840, 2011.

[24] J. R. Szczech and S. Jin, “Nanostructured silicon for high capacity lithium battery anodes,” *Energy Environ. Sci.*, vol. 4, no. 1, pp. 56–72, 2011.

[25] S. Ohara, J. Suzuki, K. Sekine, and T. Takamura, “A thin film silicon anode for Li-ion batteries having a very large specific capacity and long cycle life,” *J. Power Sources*, vol. 136, no. 2, pp. 303–306, Oct. 2004.

[26] T. Takamura, S. Ohara, M. Uehara, J. Suzuki, and K. Sekine, “A vacuum deposited Si film having a Li extraction capacity over 2000 mAh/g with a long cycle life,” *J. Power Sources*, vol. 129, no. 1, pp. 96–100, Apr. 2004.

[27] M. Uehara, J. Suzuki, K. Tamura, K. Sekine, and T. Takamura, “Thick vacuum deposited silicon films suitable for the anode of Li-ion battery,” *J. Power Sources*, vol. 146, no. 1–2, pp. 441–444, Aug. 2005.

[28] W. Wang, M. K. Datta, and P. N. Kumta, “Silicon-based composite anodes for Li-ion rechargeable batteries,” *J. Mater. Chem.*, vol. 17, no. 30, pp. 3229–3237, 2007.

[29] H. Kim, M. Seo, M.-H. Park, and J. Cho, “A Critical Size of Silicon Nano-Anodes for Lithium Rechargeable Batteries,” *Angew. Chemie Int. Ed.*, vol. 49, no. 12, pp. 2146–2149, 2010.

[30] C. K. Chan, H. Peng, G. Liu, K. McIlwrath, X. F. Zhang, R. A. Huggins, and Y. Cui, “High-performance lithium battery anodes using silicon nanowires,” *Nat Nano*, vol. 3, no. 1, pp. 31–35, Jan. 2008.

[31] M.-H. Park, M. G. Kim, J. Joo, K. Kim, J. Kim, S. Ahn, Y. Cui, and J. Cho, “Silicon Nanotube Battery Anodes,” *Nano Lett.*, vol. 9, no. 11, pp. 3844–3847, Sep. 2009.

[32] T. Song, J. Xia, J.-H. Lee, D. H. Lee, M.-S. Kwon, J.-M. Choi, J. Wu, S. K. Doo, H. Chang, W. Il Park, D. S. Zang, H. Kim, Y. Huang, K.-C. Hwang, J. A. Rogers, and U. Paik, “Arrays of Sealed Silicon Nanotubes As Anodes for Lithium Ion Batteries,” *Nano Lett.*, vol. 10, no. 5, pp. 1710–1716, Apr. 2010.

[33] J. Cho, “Porous Si anode materials for lithium rechargeable batteries,” *J. Mater. Chem.*, vol. 20, no. 20, pp. 4009–4014, 2010.

[34] L. Su, Y. Jing, and Z. Zhou, “Li ion battery materials with core-shell nanostructures,” *Nanoscale*, vol. 3, no. 10, pp. 3967–3983, 2011.

[35] T. Shimizu, T. Xie, J. Nishikawa, S. Shingubara, S. Senz, and U. Gösele, “Synthesis of Vertical High-Density Epitaxial Si(100) Nanowire Arrays on a Si(100) Substrate Using an Anodic Aluminum Oxide Template,” *Adv. Mater.*, vol. 19, no. 7, pp. 917–920, 2007.

[36] F.-F. Cao, Y.-G. Guo, and L.-J. Wan, “Better lithium-ion batteries with nanocable-like electrode materials,” *Energy Environ. Sci.*, vol. 4, no. 5, pp. 1634–1642, 2011.

[37] H. Wu and Y. Cui, “Designing nanostructured Si anodes for high energy lithium ion batteries,” *Nano Today*, vol. 7, no. 5, pp. 414–429, Oct. 2012.

[38] F. Orsini, A. du Pasquier, B. Beaudouin, J. M. Tarascon, M. Trentin, N. Langenhuizen, E. de Beer, and P. Notten, “In situ SEM study of the interfaces

in plastic lithium cells," *J. Power Sources*, vol. 81–82, no. 0, pp. 918–921, Sep. 1999.

[39] M. Morcrette, Y. Chabre, G. Vaughan, G. Amatucci, J.-B. Leriche, S. Patoux, C. Masquelier, and J.-M. Tarascon, "In situ X-ray diffraction techniques as a powerful tool to study battery electrode materials," *Electrochim. Acta*, vol. 47, no. 19, pp. 3137–3149, Jul. 2002.

[40] R. Baddour-Hadjean and J.-P. Pereira-Ramos, "Raman Microspectrometry Applied to the Study of Electrode Materials for Lithium Batteries," *Chem. Rev.*, vol. 110, no. 3, pp. 1278–1319, Nov. 2009.

[41] F. Poli, J. S. Kshetrimayum, L. Monconduit, and M. Letellier, "New cell design for in-situ NMR studies of lithium-ion batteries," *Electrochem. commun.*, vol. 13, no. 12, pp. 1293–1295, Dec. 2011.

[42] D. B. Williams and C. B. Carter, *Transmission Electron Microscopy: A Textbook for Materials Science*, no. v. 1. Springer, 2009.

[43] R. F. Egerton, *Physical Principles of Electron Microscopy: An Introduction to TEM, SEM, and AEM*. Springer Science+Business Media, 2006.

[44] K. Svensson, Y. Jompol, H. Olin, and E. Olsson, "Compact design of a transmission electron microscope-scanning tunneling microscope holder with three-dimensional coarse motion," *Rev. Sci. Instrum.*, vol. 74, no. 11, pp. 4945–4947, 2003.

[45] K. Karki, E. Epstein, J.-H. Cho, Z. Jia, T. Li, S. T. Picraux, C. Wang, and J. Cumings, "Lithium-Assisted Electrochemical Welding in Silicon Nanowire Battery Electrodes," *Nano Lett.*, vol. 12, no. 3, pp. 1392–1397, Feb. 2012.

[46] S. T. Picraux, S. A. Dayeh, P. Manandhar, D. E. Perea, and S. G. Choi, "Silicon and germanium nanowires: Growth, properties, and integration," *Jom*, vol. 62, no. 4, pp. 35–43, 2010.

[47] D. Tham, C.-Y. Nam, K. Byon, J. Kim, and J. E. Fischer, "Applications of electron microscopy to the characterization of semiconductor nanowires," *Appl. Phys. A*, vol. 85, no. 3, pp. 227–231, 2006.

[48] L.-F. Cui, Y. Yang, C.-M. Hsu, and Y. Cui, "Carbon−Silicon Core−Shell Nanowires as High Capacity Electrode for Lithium Ion Batteries," *Nano Lett.*, vol. 9, no. 9, pp. 3370–3374, Aug. 2009.

[49] L.-F. Cui, R. Ruffo, C. K. Chan, H. Peng, and Y. Cui, "Crystalline-Amorphous Core−Shell Silicon Nanowires for High Capacity and High Current Battery Electrodes," *Nano Lett.*, vol. 9, no. 1, pp. 491–495, Dec. 2008.

[50] W. Wang and P. N. Kumta, “Nanostructured Hybrid Silicon/Carbon Nanotube Heterostructures: Reversible High-Capacity Lithium-Ion Anodes,” *ACS Nano*, vol. 4, no. 4, pp. 2233–2241, Apr. 2010.

[51] A. Magasinski, P. Dixon, B. Hertzberg, A. Kvit, J. Ayala, and G. Yushin, “High-performance lithium-ion anodes using a hierarchical bottom-up approach,” *Nat Mater*, vol. 9, no. 4, pp. 353–358, Apr. 2010.

[52] R. Huang, X. Fan, W. Shen, and J. Zhu, “Carbon-coated silicon nanowire array films for high-performance lithium-ion battery anodes,” *Appl. Phys. Lett.*, vol. 95, no. 13, p. 133119, 2009.

[53] X. H. Liu, H. Zheng, L. Zhong, S. Huang, K. Karki, L. Q. Zhang, Y. Liu, A. Kushima, W. T. Liang, J. W. Wang, J.-H. Cho, E. Epstein, S. A. Dayeh, S. T. Picraux, T. Zhu, J. Li, J. P. Sullivan, J. Cumings, C. Wang, S. X. Mao, Z. Z. Ye, S. Zhang, and J. Y. Huang, “Anisotropic Swelling and Fracture of Silicon Nanowires during Lithiation,” *Nano Lett.*, vol. 11, no. 8, pp. 3312–3318, Jun. 2011.

[54] H. Seidel, L. Csepregi, A. Heuberger, and H. Baumgärtel, “Anisotropic Etching of Crystalline Silicon in Alkaline Solutions: I . Orientation Dependence and Behavior of Passivation Layers,” *J. Electrochem. Soc.*, vol. 137, no. 11, pp. 3612–3626, Nov. 1990.

[55] B. Wu, A. Kumar, and S. Pamarthy, “High aspect ratio silicon etch: A review,” *J. Appl. Phys.*, vol. 108, no. 5, p. 51101, 2010.

[56] J. L. Goldman, B. R. Long, A. A. Gewirth, and R. G. Nuzzo, “Strain Anisotropies and Self-Limiting Capacities in Single-Crystalline 3D Silicon Microstructures: Models for High Energy Density Lithium-Ion Battery Anodes,” *Adv. Funct. Mater.*, vol. 21, no. 13, pp. 2412–2422, 2011.

[57] S. W. Lee, M. T. McDowell, J. W. Choi, and Y. Cui, “Anomalous Shape Changes of Silicon Nanopillars by Electrochemical Lithiation,” *Nano Lett.*, vol. 11, no. 7, pp. 3034–3039, Jun. 2011.

[58] H. Okamoto, “Li-Si (Lithium-Silicon),” *J. Phase Equilibria Diffus.*, vol. 30, no. 1, pp. 118–119, 2009.

[59] P. Limthongkul, Y.-I. Jang, N. J. Dudney, and Y.-M. Chiang, “Electrochemically-driven solid-state amorphization in lithium–metal anodes,” *J. Power Sources*, vol. 119–121, no. 0, pp. 604–609, Jun. 2003.

[60] T. D. Hatchard and J. R. Dahn, “In Situ XRD and Electrochemical Study of the Reaction of Lithium with Amorphous Silicon,” *J. Electrochem. Soc.*, vol. 151, no. 6, pp. A838–A842, Jun. 2004.

[61] M. N. Obrovac and L. Christensen, “Structural Changes in Silicon Anodes during Lithium Insertion/Extraction,” *Electrochem. Solid-State Lett.*, vol. 7, no. 5, pp. A93–A96, May 2004.

[62] S. Misra, N. Liu, J. Nelson, S. S. Hong, Y. Cui, and M. F. Toney, “In Situ X-ray Diffraction Studies of (De)lithiation Mechanism in Silicon Nanowire Anodes,” *ACS Nano*, vol. 6, no. 6, pp. 5465–5473, May 2012.

[63] X. H. Liu, S. Huang, S. T. Picraux, J. Li, T. Zhu, and J. Y. Huang, “Reversible Nanopore Formation in Ge Nanowires during Lithiation–Delithiation Cycling: An In Situ Transmission Electron Microscopy Study,” *Nano Lett.*, vol. 11, no. 9, pp. 3991–3997, Aug. 2011.

[64] I. Ryu, J. W. Choi, Y. Cui, and W. D. Nix, “Size-dependent fracture of Si nanowire battery anodes,” *J. Mech. Phys. Solids*, vol. 59, no. 9, pp. 1717–1730, Sep. 2011.

[65] J. Li, A. K. Dozier, Y. Li, F. Yang, and Y.-T. Cheng, “Crack Pattern Formation in Thin Film Lithium-Ion Battery Electrodes,” *J. Electrochem. Soc.*, vol. 158, no. 6, pp. A689–A694, Jun. 2011.

[66] H. Li, X. Huang, L. Chen, G. Zhou, Z. Zhang, D. Yu, Y. Jun Mo, and N. Pei, “The crystal structural evolution of nano-Si anode caused by lithium insertion and extraction at room temperature,” *Solid State Ionics*, vol. 135, no. 1–4, pp. 181–191, Nov. 2000.

[67] H. Li, L. Shi, W. Lu, X. Huang, and L. Chen, “Studies on Capacity Loss and Capacity Fading of Nanosized SnSb Alloy Anode for Li-Ion Batteries,” *J. Electrochem. Soc.* , vol. 148 , no. 8 , pp. A915–A922, Aug. 2001.

[68] J. H. Ryu, J. W. Kim, Y.-E. Sung, and S. M. Oh, “Failure Modes of Silicon Powder Negative Electrode in Lithium Secondary Batteries,” *Electrochem. Solid-State Lett.* , vol. 7 , no. 10 , pp. A306–A309, Oct. 2004.

[69] I. A. Courtney, W. R. McKinnon, and J. R. Dahn, “On the Aggregation of Tin in SnO Composite Glasses Caused by the Reversible Reaction with Lithium,” *J. Electrochem. Soc.* , vol. 146 , no. 1 , pp. 59–68, Jan. 1999.

[70] L. Shi, H. Li, Z. Wang, X. Huang, and L. Chen, “Nano-SnSb alloy deposited on MCMB as an anode material for lithium ion batteries,” *J. Mater. Chem.*, vol. 11, no. 5, pp. 1502–1505, 2001.

[71] Y. I. Kharkats, “Transition to a state of superionic conduction induced by an electric field,” *Sov. Phys. Solid State*, no. 23, pp. 1283–1284, 1981.

[72] Y. Y. Gurevich, “Theory of abrupt disordering in solid electrolytes induced by an electric field,” *Sov. Electrochem.*, vol. 20, no. 1, pp. 65–71, 1984.

[73] C. Cayron, M. Den Hertog, L. Latu-Romain, C. Mouchet, C. Secouard, J.-L. Rouviere, E. Rouviere, and J.-P. Simonato, “Odd electron diffraction patterns in silicon nanowires and silicon thin films explained by microtwins and nanotwins,” *J. Appl. Crystallogr.*, vol. 42, no. 2, pp. 242–252, Apr. 2009.

[74] S. A. Dayeh, J. Wang, N. Li, J. Y. Huang, A. V Gin, and S. T. Picraux, “Growth, Defect Formation, and Morphology Control of Germanium–Silicon Semiconductor Nanowire Heterostructures,” *Nano Lett.*, vol. 11, no. 10, pp. 4200–4206, Aug. 2011.

[75] J. F. Shackelford and W. Alexander, *CRC Materials Science and Engineering Handbook*, Third. CRC Press, FL, 2001, p. 628.

[76] J. F. Shackelford and W. Alexander, *CRC Materials Science and Engineering Handbook*, Third. CRC Press, FL, 2001, p. 1587.

[77] K. Zhao, W. L. Wang, J. Gregoire, M. Pharr, Z. Suo, J. J. Vlassak, and E. Kaxiras, “Lithium-Assisted Plastic Deformation of Silicon Electrodes in Lithium-Ion Batteries: A First-Principles Theoretical Study,” *Nano Lett.*, vol. 11, no. 7, pp. 2962–2967, Jun. 2011.

[78] Q. Sun, B. Zhang, and Z.-W. Fu, “Lithium electrochemistry of SiO2 thin film electrode for lithium-ion batteries,” *Appl. Surf. Sci.*, vol. 254, no. 13, pp. 3774–3779, Apr. 2008.

[79] B. Guo, J. Shu, Z. Wang, H. Yang, L. Shi, Y. Liu, and L. Chen, “Electrochemical reduction of nano-SiO2 in hard carbon as anode material for lithium ion batteries,” *Electrochem. commun.*, vol. 10, no. 12, pp. 1876–1878, Dec. 2008.

[80] Y. Yamada, Y. Iriyama, T. Abe, and Z. Ogumi, “Kinetics of Electrochemical Insertion and Extraction of Lithium Ion at SiO,” *J. Electrochem. Soc.* , vol. 157 , no. 1 , pp. A26–A30, Jan. 2010.

[81] H. Li, L. Shi, Q. Wang, L. Chen, and X. Huang, “Nano-alloy anode for lithium ion batteries,” *Solid State Ionics*, vol. 148, no. 3–4, pp. 247–258, Jun. 2002.

[82] H. T. Nguyen, F. Yao, M. R. Zamfir, C. Biswas, K. P. So, Y. H. Lee, S. M. Kim, S. N. Cha, J. M. Kim, and D. Pribat, “Highly Interconnected Si Nanowires for Improved Stability Li-Ion Battery Anodes,” *Adv. Energy Mater.*, vol. 1, no. 6, pp. 1154–1161, 2011.

[83] H. Liao, K. Karki, Y. Zhang, J. Cumings, and Y. Wang, “Interfacial Mechanics of Carbon Nanotube@Amorphous-Si Coaxial Nanostructures,” *Adv. Mater.*, vol. 23, no. 37, pp. 4318–4322, 2011.

[84] S. Liao, K.-A. Holmes, H. Tsaprailis, and V. I. Birss, “High Performance PtRuIr Catalysts Supported on Carbon Nanotubes for the Anodic Oxidation of Methanol,” *J. Am. Chem. Soc.*, vol. 128, no. 11, pp. 3504–3505, Feb. 2006.

[85] M. M. Shaijumon, S. Ramaprabhu, and N. Rajalakshmi, “Platinum/multiwalled carbon nanotubes-platinum/carbon composites as electrocatalysts for oxygen reduction reaction in proton exchange membrane fuel cell,” *Appl. Phys. Lett.*, vol. 88, no. 25, p. 253105, 2006.

[86] J. Chen, Y. Liu, A. I. Minett, C. Lynam, J. Wang, and G. G. Wallace, “Flexible, Aligned Carbon Nanotube/Conducting Polymer Electrodes for a Lithium-Ion Battery,” *Chem. Mater.*, vol. 19, no. 15, pp. 3595–3597, Jun. 2007.

[87] E. W. Wong, P. E. Sheehan, and C. M. Lieber, “Nanobeam Mechanics: Elasticity, Strength, and Toughness of Nanorods and Nanotubes,” *Sci.* , vol. 277 , no. 5334 , pp. 1971–1975, Sep. 1997.

[88] P. Poncharal, Z. L. Wang, D. Ugarte, and W. A. de Heer, “Electrostatic Deflections and Electromechanical Resonances of Carbon Nanotubes,” *Sci.* , vol. 283 , no. 5407 , pp. 1513–1516, Mar. 1999.

[89] R. Gao, Z. L. Wang, Z. Bai, W. A. de Heer, L. Dai, and M. Gao, “Nanomechanics of Individual Carbon Nanotubes from Pyrolytically Grown Arrays,” *Phys. Rev. Lett.*, vol. 85, no. 3, pp. 622–625, Jul. 2000.

[90] S. Deng, A. H. Brozena, Y. Zhang, Y. Piao, and Y. Wang, “Diameter-dependent{,} progressive alkylcarboxylation of single-walled carbon nanotubes,” *Chem. Commun.*, vol. 47, no. 2, pp. 758–760, 2011.

[91] J. Y. Huang, H. Zheng, S. X. Mao, Q. Li, and G. T. Wang, “In Situ Nanomechanics of GaN Nanowires,” *Nano Lett.*, vol. 11, no. 4, pp. 1618–1622, Mar. 2011.

[92] R. T. Howe and R. S. Muller, “Polycrystalline and amorphous silicon micromechanical beams: annealing and mechanical properties,” *Sensors and Actuators*, vol. 4, no. 0, pp. 447–454, 1983.

[93] M.-F. Yu, O. Lourie, M. J. Dyer, K. Moloni, T. F. Kelly, and R. S. Ruoff, “Strength and Breaking Mechanism of Multiwalled Carbon Nanotubes Under Tensile Load,” *Sci.* , vol. 287 , no. 5453 , pp. 637–640, Jan. 2000.

[94] C.-F. Sun, K. Karki, Z. Jia, H. Liao, Y. Zhang, T. Li, Y. Qi, J. Cumings, G. W. Rubloff, and Y. Wang, "A Beaded-String Silicon Anode," *ACS Nano*, vol. 7, no. 3, pp. 2717–2724, Feb. 2013.

[95] P. S. Ho, P. O. Hahn, J. W. Bartha, G. W. Rubloff, F. K. LeGoues, and B. D. Silverman, "Chemical bonding and reaction at metal/polymer interfaces," *J. Vac. Sci. Technol. A Vacuum, Surfaces, Film.*, vol. 3, no. 3, pp. 739–745, 1985.

[96] P. Lucksanasombool, W. A. J. Higgs, R. J. E. . Higgs, and M. V Swain, "Interfacial fracture toughness between bovine cortical bone and cements," *Biomaterials*, vol. 24, no. 7, pp. 1159–1166, Mar. 2003.

[97] R. A. Sharma and R. N. Seefurth, "Thermodynamic Properties of the Lithium-Silicon System," *J. Electrochem. Soc.* , vol. 123 , no. 12 , pp. 1763–1768, Dec. 1976.

[98] B. A. Boukamp, G. C. Lesh, and R. A. Huggins, "All-Solid Lithium Electrodes with Mixed-Conductor Matrix," *J. Electrochem. Soc.* , vol. 128 , no. 4 , pp. 725–729, Apr. 1981.

[99] H. Wu, G. Chan, J. W. Choi, I. Ryu, Y. Yao, M. T. McDowell, S. W. Lee, A. Jackson, Y. Yang, L. Hu, and Y. Cui, "Stable cycling of double-walled silicon nanotube battery anodes through solid-electrolyte interphase control," *Nat Nano*, vol. 7, no. 5, pp. 310–315, May 2012.

[100] X. H. Liu, L. Zhong, S. Huang, S. X. Mao, T. Zhu, and J. Y. Huang, "Size-Dependent Fracture of Silicon Nanoparticles During Lithiation," *ACS Nano*, vol. 6, no. 2, pp. 1522–1531, Jan. 2012.

[101] J.-S. Bridel, T. Azaïs, M. Morcrette, J.-M. Tarascon, and D. Larcher, "Key Parameters Governing the Reversibility of Si/Carbon/CMC Electrodes for Li-Ion Batteries†," *Chem. Mater.*, vol. 22, no. 3, pp. 1229–1241, Dec. 2009.

[102] Z. Chen, L. Christensen, and J. R. Dahn, "A study of the mechanical and electrical properties of a polymer/carbon black binder system used in battery electrodes," *J. Appl. Polym. Sci.*, vol. 90, no. 7, pp. 1891–1899, 2003.

[103] J. Christensen, "Modeling Diffusion-Induced Stress in Li-Ion Cells with Porous Electrodes," *J. Electrochem. Soc.* , vol. 157 , no. 3 , pp. A366–A380, Mar. 2010.

[104] C.-M. Wang, X. Li, Z. Wang, W. Xu, J. Liu, F. Gao, L. Kovarik, J.-G. Zhang, J. Howe, D. J. Burton, Z. Liu, X. Xiao, S. Thevuthasan, and D. R. Baer, "In Situ TEM Investigation of Congruent Phase Transition and Structural Evolution of Nanostructured Silicon/Carbon Anode for Lithium Ion Batteries," *Nano Lett.*, vol. 12, no. 3, pp. 1624–1632, Mar. 2012.

[105] J. Y. Howe, D. J. Burton, Y. Qi, H. M. Meyer III, M. Nazri, G. A. Nazri, A. C. Palmer, and P. D. Lake, "Improving microstructure of silicon/carbon nanofiber composites as a Li battery anode," *J. Power Sources*, vol. 221, no. 0, pp. 455–461, Jan. 2013.

[106] L. Fransson, T. Eriksson, K. Edström, T. Gustafsson, and J. O. Thomas, "Influence of carbon black and binder on Li-ion batteries," *J. Power Sources*, vol. 101, no. 1, pp. 1–9, Oct. 2001.

[107] S. S. Zhang and T. R. Jow, "Study of poly(acrylonitrile-methyl methacrylate) as binder for graphite anode and LiMn2O4 cathode of Li-ion batteries," *J. Power Sources*, vol. 109, no. 2, pp. 422–426, Jul. 2002.

[108] D. Guy, B. Lestriez, and D. Guyomard, "New Composite Electrode Architecture and Improved Battery Performance from the Smart Use of Polymers and Their Properties," *Adv. Mater.*, vol. 16, no. 6, pp. 553–557, 2004.

[109] I. Kovalenko, B. Zdyrko, A. Magasinski, B. Hertzberg, Z. Milicev, R. Burtovyy, I. Luzinov, and G. Yushin, "A Major Constituent of Brown Algae for Use in High-Capacity Li-Ion Batteries," *Sci.* , vol. 334 , no. 6052 , pp. 75–79, Oct. 2011.

[110] S. Deng, Y. Zhang, A. H. Brozena, M. L. Mayes, P. Banerjee, W.-A. Chiou, G. W. Rubloff, G. C. Schatz, and Y. Wang, "Confined propagation of covalent chemical reactions on single-walled carbon nanotubes," *Nat Commun*, vol. 2, p. 382, Jul. 2011.

[111] K. Karki, Y. Zhu, Y. Liu, C.-F. Sun, L. Hu, Y. Wang, C. Wang, and J. Cumings, "Hoop-Strong Nanotubes for Battery Electrodes," *ACS Nano*, vol. 7, no. 9, pp. 8295–8302, Aug. 2013.

[112] M. Armand and J.-M. Tarascon, "Building better batteries," *Nature*, vol. 451, no. 7179, pp. 652–657, Feb. 2008.

[113] A. S. Arico, P. Bruce, B. Scrosati, J.-M. Tarascon, and W. van Schalkwijk, "Nanostructured materials for advanced energy conversion and storage devices," *Nat Mater*, vol. 4, no. 5, pp. 366–377, May 2005.

[114] J. Christensen and J. Newman, "Stress generation and fracture in lithium insertion materials," *J. Solid State Electrochem.*, vol. 10, no. 5, pp. 293–319, 2006.

[115] V. A. Sethuraman, M. J. Chon, M. Shimshak, V. Srinivasan, and P. R. Guduru, "In situ measurements of stress evolution in silicon thin films during

electrochemical lithiation and delithiation," *J. Power Sources*, vol. 195, no. 15, pp. 5062–5066, Aug. 2010.

[116] P. V Braun, J. Cho, J. H. Pikul, W. P. King, and H. Zhang, "High power rechargeable batteries," *Curr. Opin. Solid State Mater. Sci.*, vol. 16, no. 4, pp. 186–198, Aug. 2012.

[117] B. Hertzberg, A. Alexeev, and G. Yushin, "Deformations in Si−Li Anodes Upon Electrochemical Alloying in Nano-Confined Space," *J. Am. Chem. Soc.*, vol. 132, no. 25, pp. 8548–8549, Jun. 2010.

[118] V. A. Sethuraman, K. Kowolik, and V. Srinivasan, "Increased cycling efficiency and rate capability of copper-coated silicon anodes in lithium-ion batteries," *J. Power Sources*, vol. 196, no. 1, pp. 393–398, Jan. 2011.

[119] M. T. McDowell, S. Woo Lee, C. Wang, and Y. Cui, "The effect of metallic coatings and crystallinity on the volume expansion of silicon during electrochemical lithiation/delithiation," *Nano Energy*, vol. 1, no. 3, pp. 401–410, May 2012.

[120] I. Sandu, T. Brousse, and D. M. Schleich, "Effect of nickel coating on electrochemical performance of graphite anodes for lithium ion batteries," *Ionics (Kiel).*, vol. 9, no. 5–6, pp. 329–335, 2003.

[121] V. R. Subramanian, P. Yu, B. N. Popov, and R. E. White, "Modeling lithium diffusion in nickel composite graphite," *J. Power Sources*, vol. 96, no. 2, pp. 396–405, Jun. 2001.

[122] Y. Yu, L. Gu, C. Zhu, S. Tsukimoto, P. A. van Aken, and J. Maier, "Reversible Storage of Lithium in Silver-Coated Three-Dimensional Macroporous Silicon," *Adv. Mater.*, vol. 22, no. 20, pp. 2247–2250, 2010.

[123] X. Xiao, P. Lu, and D. Ahn, "Ultrathin Multifunctional Oxide Coatings for Lithium Ion Batteries," *Adv. Mater.*, vol. 23, no. 34, pp. 3911–3915, 2011.

[124] Y. Yao, M. T. McDowell, I. Ryu, H. Wu, N. Liu, L. Hu, W. D. Nix, and Y. Cui, "Interconnected Silicon Hollow Nanospheres for Lithium-Ion Battery Anodes with Long Cycle Life," *Nano Lett.*, vol. 11, no. 7, pp. 2949–2954, Jun. 2011.

[125] H. Ghassemi, M. Au, N. Chen, P. A. Heiden, and R. S. Yassar, "In Situ Electrochemical Lithiation/Delithiation Observation of Individual Amorphous Si Nanorods," *ACS Nano*, vol. 5, no. 10, pp. 7805–7811, Sep. 2011.

[126] B. E. Deal and A. S. Grove, "General Relationship for the Thermal Oxidation of Silicon," *J. Appl. Phys.*, vol. 36, no. 12, pp. 3770–3778, 1965.

[127] M. T. McDowell, S. W. Lee, J. T. Harris, B. A. Korgel, C. Wang, W. D. Nix, and Y. Cui, "In Situ TEM of Two-Phase Lithiation of Amorphous Silicon Nanospheres," *Nano Lett.*, vol. 13, no. 2, pp. 758–764, Jan. 2013.

[128] J. W. Wang, Y. He, F. Fan, X. H. Liu, S. Xia, Y. Liu, C. T. Harris, H. Li, J. Y. Huang, S. X. Mao, and T. Zhu, "Two-Phase Electrochemical Lithiation in Amorphous Silicon," *Nano Lett.*, vol. 13, no. 2, pp. 709–715, Jan. 2013.

[129] P. R. Abel, Y.-M. Lin, H. Celio, A. Heller, and C. B. Mullins, "Improving the Stability of Nanostructured Silicon Thin Film Lithium-Ion Battery Anodes through Their Controlled Oxidation," *ACS Nano*, vol. 6, no. 3, pp. 2506–2516, Feb. 2012.

[130] J. Yang, Y. Takeda, N. Imanishi, C. Capiglia, J. Y. Xie, and O. Yamamoto, "SiOx-based anodes for secondary lithium batteries," *Solid State Ionics*, vol. 152–153, no. 0, pp. 125–129, Dec. 2002.

[131] K. Kim, J.-H. Park, S.-G. Doo, and T. Kim, "Effect of oxidation on Li-ion secondary battery with non-stoichiometric silicon oxide (SiOx) nanoparticles generated in cold plasma," *Thin Solid Films*, vol. 518, no. 22, pp. 6547–6549, Sep. 2010.

[132] K. Zhao, M. Pharr, L. Hartle, J. J. Vlassak, and Z. Suo, "Fracture and debonding in lithium-ion batteries with electrodes of hollow core–shell nanostructures," *J. Power Sources*, vol. 218, no. 0, pp. 6–14, Nov. 2012.

[133] S. Zhang, Z. Du, R. Lin, T. Jiang, G. Liu, X. Wu, and D. Weng, "Nickel Nanocone-Array Supported Silicon Anode for High-Performance Lithium-Ion Batteries," *Adv. Mater.*, vol. 22, no. 47, pp. 5378–5382, 2010.